March 2001 • NREL/SR-520-29283

Subcontractor Report

Photovoltaic Manufacturing Cost and Throughput Improvements for Thin-Film CIGS-Based Modules

Phase II Annual Subcontract Technical Report

July 1999–August 2000

R.G. Wendt and S. Wiedeman
Global Solar Energy, L.L.C.
Tucson, Arizona

1617 Cole Boulevard
Golden, Colorado 80401-3393

NREL is a U.S. Department of Energy Laboratory
Operated by Midwest Research Institute • Battelle • Bechtel

Contract No. DE-AC36-99-GO10337

March 2001 • NREL/SR-520-29283

Photovoltaic Manufacturing Cost and Throughput Improvements for Thin-Film CIGS-Based Modules

Phase II Annual Subcontract Technical Report

July 1999–August 2000

R.G. Wendt and S. Wiedeman
Global Solar Energy, L.L.C.
Tucson, Arizona

NREL Technical Monitor: R.L. Mitchell

Prepared under Subcontract No. ZAX-8-17647-11

1617 Cole Boulevard
Golden, Colorado 80401-3393

NREL is a U.S. Department of Energy Laboratory
Operated by Midwest Research Institute • Battelle • Bechtel

Contract No. DE-AC36-99-GO10337

NOTICE

This report was prepared as an account of work sponsored by an agency of the United States government. Neither the United States government nor any agency thereof, nor any of their employees, makes any warranty, express or implied, or assumes any legal liability or responsibility for the accuracy, completeness, or usefulness of any information, apparatus, product, or process disclosed, or represents that its use would not infringe privately owned rights. Reference herein to any specific commercial product, process, or service by trade name, trademark, manufacturer, or otherwise does not necessarily constitute or imply its endorsement, recommendation, or favoring by the United States government or any agency thereof. The views and opinions of authors expressed herein do not necessarily state or reflect those of the United States government or any agency thereof.

Available electronically at http://www.doe.gov/bridge

Available for a processing fee to U.S. Department of Energy
and its contractors, in paper, from:
U.S. Department of Energy
Office of Scientific and Technical Information
P.O. Box 62
Oak Ridge, TN 37831-0062
phone: 865.576.8401
fax: 865.576.5728
email: reports@adonis.osti.gov

Available for sale to the public, in paper, from:
U.S. Department of Commerce
National Technical Information Service
5285 Port Royal Road
Springfield, VA 22161
phone: 800.553.6847
fax: 703.605.6900
email: orders@ntis.fedworld.gov
online ordering: http://www.ntis.gov/ordering.htm

Printed on paper containing at least 50% wastepaper, including 20% postconsumer waste

Executive Summary

Interest in thin film photovoltaics (PV) has expanded dramatically in the last five years, but commercial use remains limited by performance, cost and reliability. Of all the thin film systems, copper indium gallium diselenide (CIGS) has demonstrated the greatest potential for achieving high performance at a low cost. The highest quality CIGS has been formed by multi-source co-evaporation, a technique pioneered in this country by researchers at NREL. Multi-source co-evaporation is also potentially the fastest and most cost-effective method of CIGS absorber deposition.

Global Solar Energy (GSE) has adapted multi-source co-evaporation of CIGS to large area, roll-to-roll processing on flexible substrates, enabling several manufacturing and product capability advantages. Roll-to-roll processing enables a low cost, automated continuous manufacturing process. Flexible substrates enable product application in unique as well as traditional areas.

The primary objectives of the GSE Photovoltaic Manufacturing Technology (PV-MAT) subcontract are directed toward reducing cost and expanding the production rate of thin film CIGS based PV modules on flexible substrates. Improvements will be implemented in monolithic integration, CIGS deposition, contact deposition and *in-situ* CIGS control and monitoring. Specific goals of the three-year contract are:

- **Monolithic Integration**

  —Increase integration speed by developing high speed, all-laser scribing processes that are more than 100% faster than the baseline process and offer clean, selective scribing.

  —Increase capacity and substantially reduce module area losses by replacing conventional screen-printing with industrial, high-speed ink-jet printing to dispense insulating materials with high accuracy into laser scribes.

- **Absorber Deposition**

  —Increase absorber layer deposition rate by 75% in the large area, continuous GSE process, increasing throughput and reducing labor and capital costs.

  —Integrate a parallel detector spectroscopic ellipsometer (PDSE) with mathematical algorithms for *in-situ* control of CIGS absorber enabling runs of over 300 meters of moving substrate while ensuring uniform properties.

  —Enhance health and safety by reducing selenium waste generation through modifications to the reactor and Se delivery method.

- **Back Contact Deposition**

  —Reduce back contact cost and increase operation yield by using improved back contact materials.

In Phase 1 of the PV-MAT program, GSE has attacked many of the highest risk aspects of each task with success. All-laser, selective scribing processes for CIGS have been developed, and many end-of-contract goals for scribing speed have been exceeded in the first year. High-speed ink-jet deposition of insulating material in the scribes now appears to be a viable technique, again exceeding some end-of-contract goals in the first year.

CIGS absorber deposition throughput speeds were increased by rates of up to 400% to 24-in/min, far exceeding an end of contract goal. Alternate back contact materials have been identified that show potential as candidates for replacement of higher cost molybdenum, and a novel, real time monitoring technique (PDSE) has shown remarkable sensitivity to relevant properties of the CIGS absorber layer for use as a diagnostic tool.

In Phase 2, GSE transitioned the monolithic integration and high-rate CIGS absorber tasks to the production equipment. All, laser selective scribes were demonstrated on production equipment at rates that exceed third year goals. In addition, the scribing equipment was upgraded to support higher speed web motion, active web steering, multiple direction scribing, and multiple beam scribing. Ink-jet equipment was substantially upgraded to support two direction ink dispense and cure as well as reduce mean time between failure.

CIGS deposition in production-based equipment during Phase 2 focused on upgrading the effusion sources to support high-rate deposition for extended run lengths. Runs of up to 600-ft were conducted with most in the range of 200 to 300-ft. At high CIGS deposition rates, Se utilization was optimized to fully react the film without overloading the system with waste.

PDSE was installed in a research-based system capable of depositing on 13-in wide substrates in either a roll-to-roll or rigid-transport fashion. Based on the preliminary experiments, the instrument is under design for integration into the production-based CIGS system. In parallel, several samples with widely varied composition were analyzed to establish preliminary data regression algorithms.

Based on results of last year, the high-rate Mo back contact was used during the entire year to provide material for the CIGS system. Deposition parameters have been fully integrated into production.

Table of Contents

Page

Executive Summary i
Table of Contents iii
List of Figures v
List of Tables v
6. Task 6 – High Speed, All Laser Scribing Processes 1
6.1 Introduction 1
6.2 Task Objectives 1
6.3 Summary of Phase 1 Accomplishments 2
6.4 Technical Approach 2
6.5 Results 4
6.5.1 Automation 4
6.5.2 Scribe Process Validation and Performance 5
6.6 Conclusions and Future Work 9
7. Task 7 – Ink-Jet Technology for Insulator Deposition 10
7.1 Introduction 10
7.2 Task Objectives 10
7.3 Summary of Phase 1 Accomplishments 11
7.4 Technical Approach 11
7.5 Results 11
7.6 Conclusions and Future Work 14
8. Task 8 - High Rate CIGS Deposition 15
8.1 Introduction 15
8.2 Task 3 Objectives 16
8.3 Technical Approach 16
8.4 Results 17
8.4.1 Source Design and Operation 17
8.4.2 High-Rate CIGS Films 25
8.4.3 Materials Utilization 26
8.5 Conclusions and Future Work 30
9. Task 9 Absorber Layer Diagnostic Development 31

9.1 Introduction 31
9.2 Goals 31
9.3 Summary of Phase 1 Accomplishments 32
9.4 Summary of Phase II Accomplishments 32
9.5 Task Objectives 33
9.6 Technical Approach 33
9.7 Results 34
9.7.1 PDSE Hardware Development 34
9.7.2 Spectroscopic Ellipsometry Analysis of CIGS Thin Films 41
9.8 Conclusion and Future Work 57
10. Alternative Contacts 59
10.1 Task 10 Back Contact 59
10.1.1 Introduction 59
10.1.2 Back Contact Task Objectives 59
10.1.3 Back Contact Technical Approach 60
10.1.4 Back Contact Results 60
10.2 Front Contact Introduction 64
10.2.1 Front Contact Task Objectives 65
10.2.2 Front Contact Technical Approach 65
10.2.3 Front Contact Results 65

List of Figures

Page

Figure 6.1 Resultant module interconnect structure on flexible substrate.................................. 2

Figure 6.2 Optical micrograph of a back contact scribe (left) and via scribe (right) done in 1st laser operation. Spacing between scribes is approximately 300 microns. 3

Figure 6.3. SEM image of a front contact scribe done in the 2nd laser operation......................... 3

Figure 6.4. Resistance between adjacent back contact pads as a function of laser power. 5

Figure 6.5. The minimum resistance measured across back contact scribes versus CIGS layer thickness shown for three different levels of laser power (approximately 10% apart) as represented by the 3 separate curves. The minimum acceptable resistance is 200 ohms. 6

Figure 6.6. The minimum resistance measured across back contact scribes versus CIGS stoichiometry is shown. Different levels of laser power.are shown as separate curves, with the upper 3 curves being in the normal operating range and approximately 10% apart. The minimum acceptable resistance is 200 ohms. 6

Figure 6.7. The specific interconnect resistivity as a function of relative laser power used for the scribe. The maximum acceptable resistivity is indicated as a horizontal line at 1.7 ohm-cm. The interconnect resistivity is measured for 4 sets of test patterns at each laser power, each represented as a single point.............. 7

Figure 6.8. Laser isolated diodes exhibited very small variation in Voc indicative of complete isolation with no shunting. 8

Figure 6.9. The difference in average V_{oc} with surrounding cells masked and unmasked for front contact scribes done at various laser powers settings. 8

Figure 6.10. Change in V_{oc} of individual cells (unmasked-masked) for the highest, lowest and middle power studied for front contact scribe process tolerance. 9

Figure 7.1. Optical micrograph of an ink jet deposited line (approx 300 microns wide) directly on top of a back contact scribe... 12

Figure 7.2. Variation of ink line width, showing maximum and minimum measured width along a random sampling of 9 module segments. Dashed horizontal lines indicate process specification limits. 13

Figure 7.3. Optical micrograph of a finished module showing all three scribes of the monolithic interconnect (front, via and back contact scribes from left to right). The total interconnect is approximately 700 microns wide in this example. The irregular appearance is introduced largely by refractive effects viewing through the laminating materials. 14

Figure 8.1. Fraction of runs impacted by nozzle blockage over the course of 83 runs. 18

Figure 8.2. Cu spits visible on the surface of a CIGS film. 19

Figure 8.3. Cu spit density down the length of a web. 19

Figure 8.4. CIGS composition uniformity down the length of a 450 ft. web. 20

Figure 8.5. Number of top insulation layers as a function of applied power. 22

Figure 8.6. Number of side insulation layers as a function of applied power 22

Figure 8.7. Cu deposit thickness as a function of effusion source temperature 24

Figure 8.8. Log Cu thickness as a function of reciprocal effusion source temperature 24

Figure 8.9. Cu layer thickness as a function of applied power 25

Figure 8.10. Cu layer thickness as a function of applied voltage 25

Figure 8.11. Cu layer thickness as a function of applied current 25

Figure 8.12. Calculated source resistance as a function of source temperature 25

Figure 8.13. Cross sectional SEM micrographs showing the effect of Se delivery rate on CIGS morphology 28

Figure 8.14. Se consumption over the course of multiple runs with nominally identical conditions. 29

Figure 8.15. CIGS thickness as a function of effused Se mass. 30

Figure 9.1. Picture of the PDSE in a prototype CIGS vacuum deposition chamber. The optical fibers and wires for the electronics pass out of the vacuum chamber in feedthroughs in the bottom right of the picture. Flexible tubes carry nitrogen to the optical components to keep Se from depositing on the cooler surfaces. 35

Figure 9.2. Normalized stokes vectors from the PDSE with incident light at different polarizations. 36

Figure 9.3. Comparison of Si optical properties measured with a standard commercially available spectroscopic ellipsometer and the PDSE. The

PDSE data was acquired with a 15 ms integration time for the spectrometers compared to the 10 to 15 minutes required to obtain the spectra from the standard spectroscopic ellipsometer. 37

Figure 9.4. Relative intensity alignment index multiplied. The index is derived by subtracting the number of counts of the two smallest spectra from the number of counts from the two largest spectra, dividing that by the sum of the counts from all four spectra, and multiplying by 100. 39

Figure 9.5. Raw intensities from Si measured with the PDSE in the IR region between 900 and 1700 nm. 40

Figure 9.6. Measured spectroscopic ellipsometry parameters Psi and Delta from baseline CIGS sample 32876.22 for incident angles 65, 70, and 75 Degrees. 41

Figure 9.7. Measured spectroscopic ellipsometry parameters Psi and Delta from baseline CIGS sample 33157.22 for incident angles 65, 70, and 75 degrees. 42

Figure 9.8. Measured spectroscopic ellipsometry parameters Psi and Delta from baseline CIGS sample 32983.22 for incident angles 65, 70, and 75 degrees. 42

Figure 9.9. Measured spectroscopic ellipsometry parameters Psi and Delta from CIGS sample 32823.21 for incident angles 65, 70, and 75 degrees (higher Cu). 42

Figure 9.10. Measured spectroscopic ellipsometry parameters Psi and Delta from CIGS sample 33018.21 for incident angles 65, 70, and 75 degrees (Lower Cu). 43

Figure 9.11. Baseline sample 32876.22 modeled with thickness and cauchy coefficients for n & k 45

Figure 9.12. Baseline samples 33157.22 and 32983.22 modeled with thickness and cauchy coefficients for *n* and *k* coupled together for each model 46

Figure 9.13. Half thickness sample 32893.33 modeled with thickness and optical parameters from sample 32876.22. 47

Figure 9.14. High Ga sample 32988.33 modeled with thickness and cauchy parameters for n and k (more dependant on *n*) and modeled with (lower two plots) thickness and optical properties coupled to baseline samples 33157.22 and 32983.22 (See Figure 2). 48

Figure 9.15. High Ga sample 32991.33 modeled with thickness and cauchy coefficients for n and k. 49

Figure 9.16. Hi Cu sample 33021.21 modeled with thickness and cauchy coefficients for n and k. 50

Figure 9.17. Hi Cu, half thickness sample 32889.21 modeled with thickness and optical parameters from sample 33021.21. 50

Figure 9.18. Low Cu sample 32897.21 modeled with thickness and cauchy coefficients for n and k. 51

Figure 9.19. Low temperature sample 32909.22 modeled with thickness and cauchy coefficients for *n* and *k*, or with thickness and coupled optical properties from sample 32876.22 (lower two plots). 52

Figure 9.20. Low temperature sample 33125.21 modeled with thickness and cauchy coefficients for *n* and *k*, or with thickness and coupled optical properties from sample 33021.21 (lower two plots). 53

Figure 9.21. Comparison of n and k values for different CIGS samples 53

Figure 9.22. Plots of the modeled SE data from sample 32876.22 for the absorption region. The models used the exact material structure established with the transparent region data to fit the absorption region data. 54

Figure 9.23. Plots of the modeled SE data from sample 32876.22 for the band gap region. The models used the exact material structure established with the transparent region data to fit the band gap region data. 55

Figure 9.24. Second derivative plots of the imaginary part of the pseudo-dielectric and dielectric functions in the band gap region. The inflection points correspond to the points in the second derivatives that are zero. 56

Figure 9.25. Comparison of bandgaps as a function of Ga(In+Ga) ratio for CIGS samples 57

Figure 10.1. Evaluation of the Ni:V back contact on a stainless steel web. 63

Figure 10.2. V_{oc}-fill factor product as a function of Mo sputtering pressure for lot S276. 64

Figure 10.3. The optical transmission of TCO on glass having 12.3 ohms/square sheet resistivity and about 4.9 mA/cm2 integrated absorptive loss on a CIGS device. 66

Figure 10.5. Typical run chart data for the TCO process showing lot-lot variation in sheet resistivity, taken on glass witness coupons co-deposited with the CIGS web. 67

List of Tables

Page

Table 8.1. Equilibrium power requirements of standard effusion sources 22

Table 8.2. Summary of Cu effusion source repeatability tests 23

Table 8.3. Summary of source volume/levelness tests 23

Table 8.4. Results from 268C 26

Table 8.5. Results from Run 280A. 26

Table 8.6. Utilization of Cu evaporated from the standard effusion source. 26

Table 8.7. Effect of Se usage on device characteristics 28

Table 9.1. Measured Composition and Thickness of CIGS Films. The Composition was measured with EDS and the thicknesses determined by substrate mass gain. 41

Table 9.2. Measured Composition and Thickness of CIGS Films. The SE information was determined from analysis of the data. 44

Table 10.1 Ohmic behavior of CIS/metal contacts from NREL Work [Ref 5-1]. 61

Table 10.2. Key material properties and cost estimates for alternative back contact materials proposed for an in-depth investigation under the GSE PVMaT program. 62

6. Task 6 – High Speed, All Laser Scribing Processes

6.1 Introduction

Monolithic integration divides active thin film PV into serially connected segments allowing the PV product to deliver an output voltage suited to an application. Serial interconnects are formed with three adjacent scribes in the back contact, absorber and front contact layers. Continuous scribes, yielding complete electrical interruption of the front and back contacts are required for the first and third scribes, without formation of bridging or shunts through the absorber layer. The second scribe forms a low resistance path between adjacent cell front and back contacts. From a manufacturing viewpoint, several areas are affected by scribing processes as described in the following paragraphs.

- **Manufacturing Rate Limitation -** Excluding module lamination and finishing, major steps that limit manufacturing throughput are often either the absorber deposition or the scribing operations for most thin film systems. Typical scribing equipment is limited to translation rates of 3 to 4-in/sec. Higher scribing rates coupled with multiple beam delivery are required to improve production throughput.

- **Active Area Loss -** Module efficiency is directly impacted by active area loss, which is related to scribe width and spacing. Scribe spacing is determined by the positional accuracy and minimum linewidths that can be obtained for the individual scribes. Accurate positioning registration, reproducibility and fine linewidth are required for both the laser scribing and printing steps to minimize active area loss.

- **Manufacturing Yield -** Product yield is a strong function of the control, reproducibility and robustness of the scribing process. The requirement for continuous front and back contact scribes is absolute. Defects caused by debris, or a single missed laser pulse can shunt an entire module segment, causing a measurable drop in performance and yield. Pinholes in the absorber, causing shunts, are often traced to debris or defect generation in the laser scribing processes. More obvious failures due to crossed or incomplete scribes also affect product yield loss. Debris must be minimized, and yield must be attacked by development of a broad, robust process window i.e., a tolerant process for each laser scribe, along with development of well-controlled, well-characterized equipment.

6.2 Task Objectives

Key issues regarding laser scribing are:

- Selective removal of thin film layers without damaging the underlying layers that remain,

- Avoiding shunt formation due to scribe debris or edge effects in the heat affected zone adjacent to the scribe,

- Speed and multiple beam delivery to achieve high throughput, and

- Process parameter tolerance and robustness.

GSE is developing high throughput, all-laser processes for selective scribing of device layers. Key goals of this GSE PV-MAT task are:

- Developing robust, selective front contact, back contact and interconnect scribing operations to improve yield.
- Developing the equipment and methods to increase scribing speed 100% to 23 cm/sec resulting in improved throughput and reduced cost.
- Minimizing scribe debris, scribe width, and the inactive heat affected zone adjacent to scribe all of which lead to lower module performance.

6.3 Summary of Phase 1 Accomplishments

During Phase 1, GSE successfully developed equipment and preliminary conditions that appeared to produce viable, all-laser, high speed (12-in/sec, 30.5-cm/sec) processes for the back contact, front contact and interconnect scribes for CIGS based modules on flexible polyimide substrates. High rate, selective, thin film cutting had been evidenced for these process, and all scribe processes have been validated microstructurally by optical and scanning electron microscopic (SEM) examination. The high rate back contact scribing process has also been validated through electrical tests. High rate front contact and interconnect scribe were demonstrated by required electrical validation and further optimization will certainly be necessary based on electrical test results. Robustness, sources of variability, and process sensitivity also remain to be fully evaluated.

6.4 Technical Approach

GSE has selected a post-absorber scribing method that enables all monolithic scribing operations to start after complete formation of the absorber and buffer. A schematic view of the finished interconnect is shown in Figure 6.1. The post-absorber technique avoids pinholes formation (and possible shunting) in the absorber that may result from microscopic debris generated by scribing before absorber deposition. Post-absorber processing requires that the scribe cut in the absorber and buffer layer be back-filled with an insulating material, to be described in Task 7.

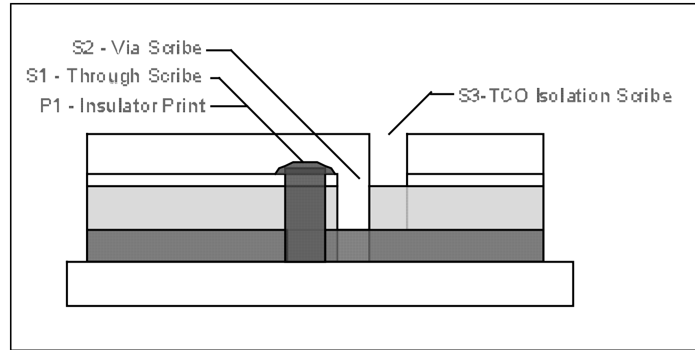

Figure 6.1 Resultant module interconnect structure on flexible substrate.

Compared to mechanical scribing, all-laser processing provides manufacturing advantages of increased speed, increased throughput, and reduced maintenance. Additionally all-laser processing is virtually required for monolithic interconnects on flexible polymer substrates because mechanical scribing on extensible or compliant substrates leads to shorting between front and back contacts.

GSE has selected laser processing equipment and parameters that allow selective cutting of specific layers in the device stack. Specifically, for the back contact (“P1”) scribe the CdS, CIGS and Mo layers are cut and the underlying substrate must be left undamaged (an example is shown in Figure 6.2). For the interconnect or via (“P2”) scribe the CdS and CIGS is cut far enough to make a conductive path to the underlying back contact material without cutting the underlying Mo back contact. This scribe need not be continuous to be a low resistance path between the front and back contacts. An example of the “P3” or front contact scribe (“P3”), is shown in Figure 6.3.

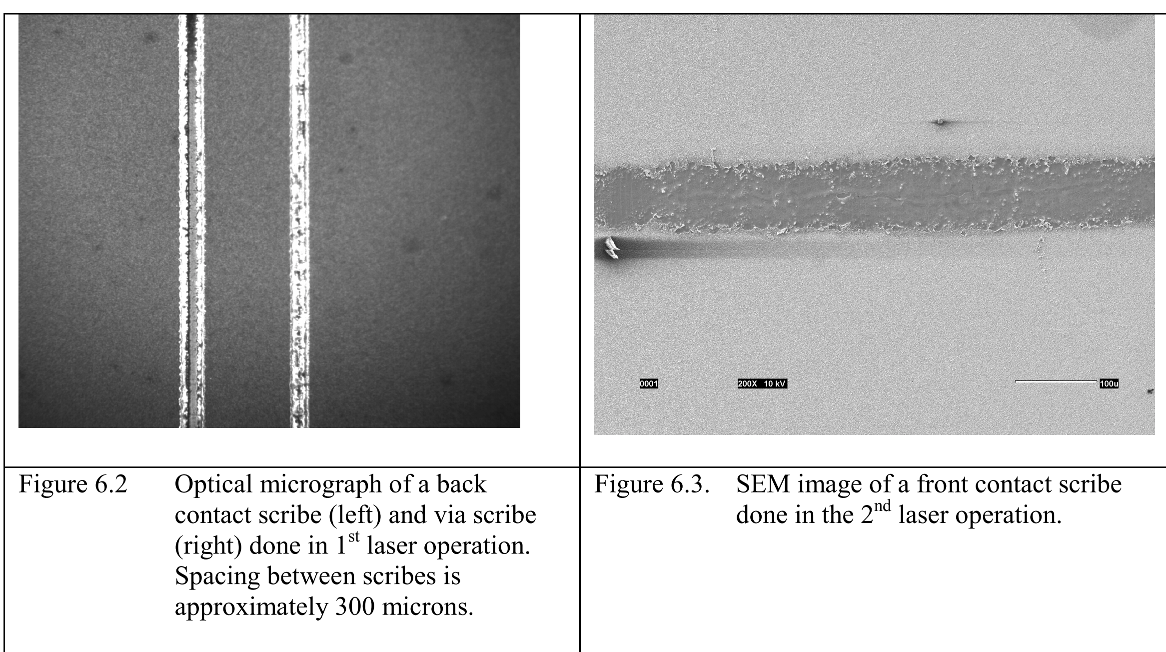

Figure 6.2 Optical micrograph of a back contact scribe (left) and via scribe (right) done in 1st laser operation. Spacing between scribes is approximately 300 microns.

Figure 6.3. SEM image of a front contact scribe done in the 2nd laser operation.

Throughput demands are met by using high speeds and multiple beams. The scribing equipment at GSE utilizes up to 4 beams simultaneously. The standard scribing rate for all processes is presently 30 cm/sec.

Flexible web substrate also demands that all laser processing be conducted from the deposited film side. A length of web (still integral as part of a long roll) is held stationary on a vacuum chuck for the laser patterning of one or more modules. During the first laser operation, P1 and P2 scribes and fiducial marks are cut for one or more modules. After a region is scribed, the web is advanced and tensioned using the web drive system for scribing the next region of web. During the second laser operation, the P3 scribe is accomplished after TCO deposition on the same equipment. Using machine vision to locate and register each module pattern using the previously cut fiducial marks. Components of the machine vision system are used for scribe alignment, inspection and measurement during processing.

In Phase 1 scribe processes feasibility was demonstrated for this approach as evidenced by the microstructural properties of individual scribes and successful serial addition of voltage from module segments. Going into Phase 2 major issues remaining for the monolithic. post-absorber, all-laser approach were process robustness or tolerance, reproducibility and control. Verification of scribe performance for all three scribes by electrical means was required, as was increased automation and evaluation of process tolerance.

6.5 Results

6.5.1 Automation

The web drive and tensioning system required improved capability in several aspects for high rate unattended manufacturing operation. During Phase 2 the entire web drive system was replaced with one designed with several improvements, most notably are:

- Accurate web advance and placement based on true web movement.
- Improved tension control on both a dynamic and static basis.
- Automatic web tracking correction for web skew and misalignment.

GSE demonstrated an automated step-and-repeat mode in which many sequential module patterns are formed by successive scribe and web-advance steps for the first laser operation (P1, P2 and the ink-jet deposition). For the second laser operation, after TCO deposition, registration of the existing module pattern is required using the machine vision to find fiducial marks. A separate encoder attached to a fixed radius roller accurately measures web position during web advance within precision of better than 0.010-in. With this accuracy we expect to be able to place fiducial marks directly in the field of view of the machine vision system and avoid uncertainty in the panel location and the time that would be required to search for the fiducial marks. With robust fiducial recognition, an automated step-and-repeat operation should be possible for the second laser operation.

Lateral positioning of the web is also important to achieve moderate accuracy for pattern placement during the first laser operation, and for finding fiducials for the second laser operation. Active web tracking correction, implemented as a separate servo feedback system, has enabled accurate control of lateral web position during web advance and patterning.

Automatic fiducial recognition by the machine vision system is also required for unattended operation. Contrast or lighting changes, slight variation in the appearance or orientation of the fiducial, or extraneous artifacts or scratches in the field of view can prevent successful recognition of a valid fiducial, or can falsely indicate the presence of a fiducial. By testing several fiducial patterns over a range of conditions and parameters for the pattern matching algorithm, we were highly successful in finding fiducial centroids accurately. Further tests, however, indicated that having fairly uniform material in the field of view is required.

6.5.2 Scribe Process Validation and Performance

6.5.2.1 Back Contact Scribe

The P1 or back contact scribe is not necessarily continuous and must exhibit a high enough resistance that leakage current between adjacent module segments is negligible in comparison to the module I_{sc} at full cell voltage. In Phase 1 we demonstrated that our back contact scribing process was reproducible and did not exhibit sporadic failures such as "bridging" defects. In Phase 2 we have demonstrated that the scribing process is robust to changes in the most important operational variables.

Shown below in Figure 6.4 is the maximum and minimum resistance obtained across a set of back contact scribes as a function of laser power. Laser power was selected as a variable because it is a key parameter or the process and does exhibit some natural variation during operation, typically less than 4%. The data in Figure 6.4 shows that a wide process window exists over a substantial range of laser power in which the resistance across the scribe far exceeds the minimum acceptable value.

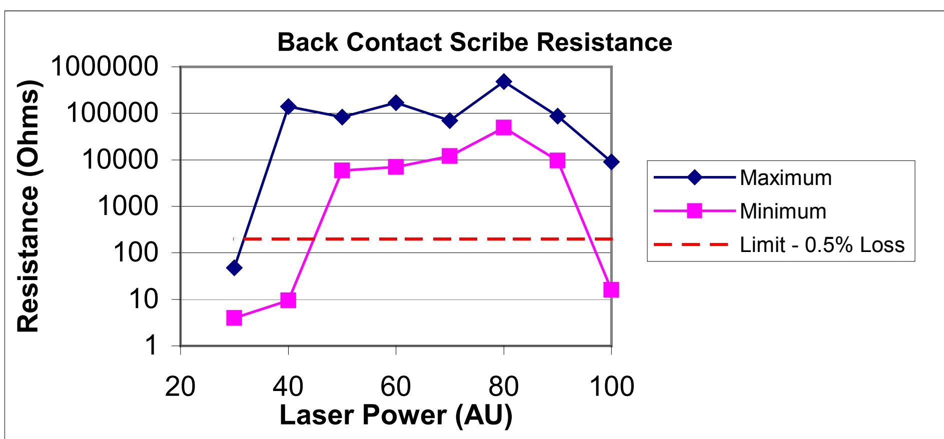

Figure 6.4. Resistance between adjacent back contact pads as a function of laser power.

Absorber thickness also shows some natural variation, and might be expected to impact scribe resistance for the back contact operation. Resistance across back contact scribes for a large number of distinct runs is shown in Figure 6.5. The absorber layer thickness of the samples used for Figure 6.5 vary by more than would normally be expected because they were drawn from experimental lots. Nevertheless, the measured resistance significantly exceeds the minimum acceptable resistance in all cases, even when the laser power is intentionally varied by 10% above and below the standard setpoint, as shown. Our data indicates that the back contact scribing process is tolerant to variations of more than a factor of two in absorber layer thickness.

Another factor that exhibits some natural variation and may be expected to affect scribing characteristics is the composition of the absorber layer. As above, experimental samples were used which exhibited more variation in stoichiometry than would normally be expected, and minimum resistance across a set of back contact scribes was recorded (shown in Figure 6.6).

Over a wide range of Cu/(In+Ga) ratio the scribe resistance exceeds the minimum acceptable value (200 Ω for that module geometry), indicating that the back scribing process is tolerant to composition variation.

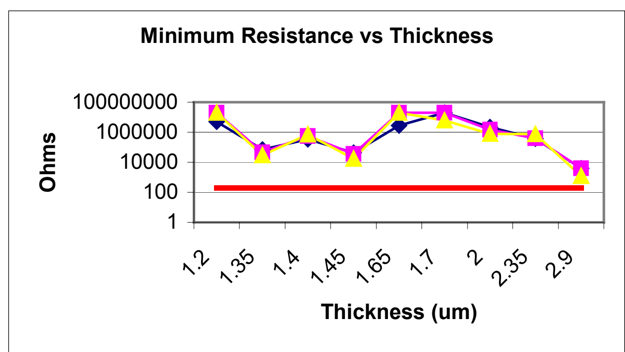

Figure 6.5. The minimum resistance measured across back contact scribes versus CIGS layer thickness shown for three different levels of laser power (approximately 10% apart) as represented by the 3 separate curves. The minimum acceptable resistance is 200 Ω.

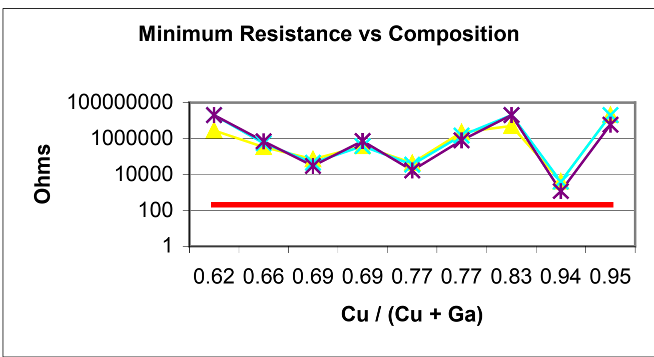

Figure 6.6. The minimum resistance measured across back contact scribes versus CIGS stoichiometry shown for different levels of laser power. The upper 3 curves indicate the normal operating range and approximately 10% apart. The minimum acceptable resistance is 200 Ω.

6.5.2.2 Interconnect (Via) Scribe

The via scribe must present a low resistance between front and back contacts of adjacent module segments. Morphological aspects of the via scribe were verified in Phase 1, consisting of micrographs and energy dispersive x-ray spectroscopy (EDS) analysis showing laser cutting down to, and exposing regions of the back contact. Electrical tests, using interconnect test patterns were used in Phase 2 to determine the specific resistivity of the established interconnect. The interconnect test patterns consist of a series of back-to-back interconnect scribes on each side of a back contact scribe. A standard interconnect test pattern consists of three sub patterns of 40 serial interconnects each, and each sub pattern has a modified geometry to allow separation of the resistance component due to the back contact, front contact, and the interconnect scribe itself.

The specific interconnect resistivity calculated from one set of interconnect tests is shown in Figure 6.7.

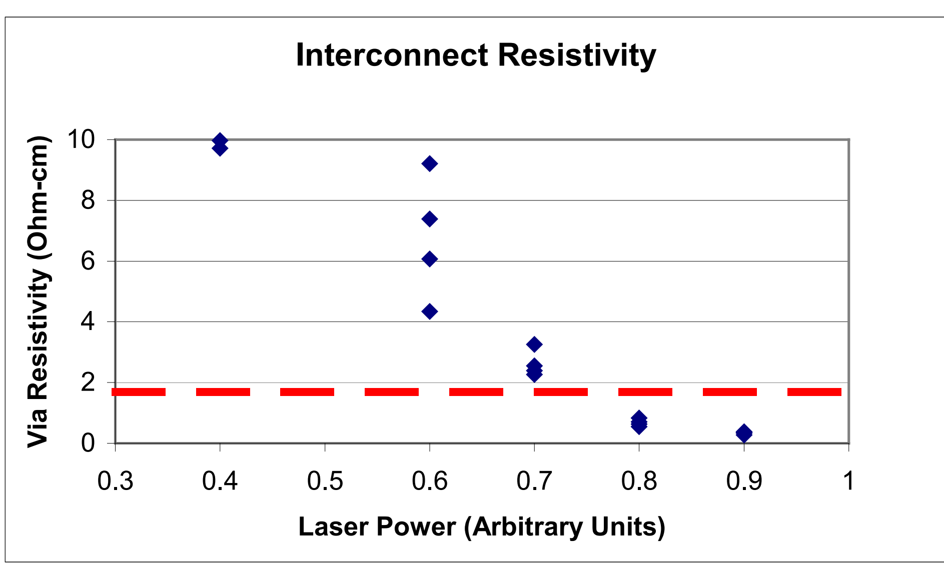

Figure 6.7. Specific interconnect resistivity as a function of relative laser power used for the scribe. The maximum acceptable resistivity is indicated as a horizontal line at 1.7 Ω-cm. The interconnect resistivity is measured for 4 sets of test patterns at each laser power, each represented as a single point.

The requirement for low interconnect resistivity can be satisfied using our process, as indicated by the data in Figure 6.7. A lower boundary for the required laser power is apparent, the boundary for upper power limit for this process is not yet known.

6.5.2.3 Front Contact Scribe

The requirements for the front contact scribe are exacting: complete and continuous isolation of the front contact while avoiding the formation of shunts either from front to back contact or between adjacent front contact segments. Microstructural evidence for successful front contact scribing was presented in Phase 1. In Phase 2 to validate electrical behavior of the laser process for the front contact we compared the J-V behavior of small area devices defined by laser scribing to that obtained by mechanical scribing. We have used mechanical scribing on stainless steel substrates routinely, and in general have found it to be free of scribe-induced shunts between the front and back contacts. Both sets of devices were made from a common sample of CIGS device stack on stainless steel substrate. The JV behavior of the devices on the laser scribed substrates was essentially identical to that of the mechanically scribed devices. Thus, the latter indicates that the laser scribing process for the front contact does not induce shunts from front-to-back contact.

We conducted multiple additional studies to assure that the front contact was completely isolated by the laser scribe, and to define the process window over which adequate front contact isolation could be obtained. Using cell arrays the J-V characteristics of small area devices were measured both with and without a mask that shaded all devices except the one under test. If the front contact scribe is incomplete, the V_{oc} of the device under test was depressed when masked (compared to unmasked) due to the large shunt conductance of the surrounding cells in the dark.

Figure 6.8 shows the relative difference in V_{oc} of individual cells between the masked and unmasked state. The average change in V_{oc} is low, although some loss in V_{oc} can be expected in the masked state due to misalignment between the mask and the cell under test.

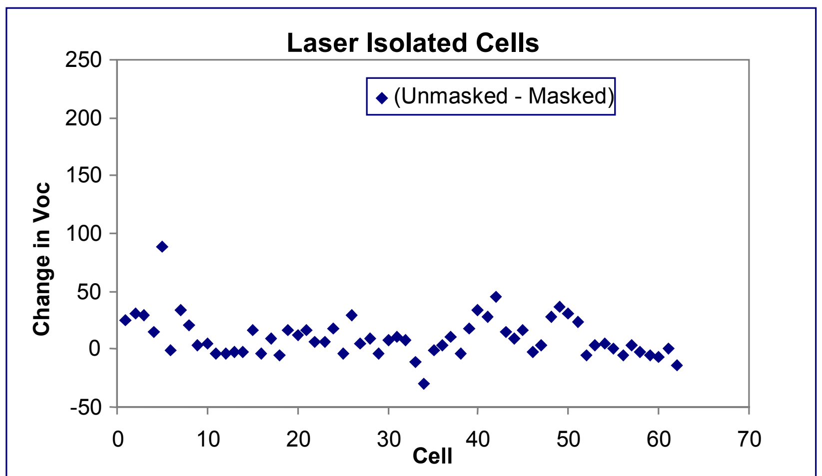

Figure 6.8. Laser isolated diodes exhibited very small variation in Voc indicative of complete isolation with no shunting.

The tolerance to variation in laser power for the front contact scribing process was evaluated by making arrays of small area devices using various laser power settings and evaluating for complete isolation using the unmasked-masked V_{oc} test, results shown in Figure 6.9 and Figure 6.10. Remarkably, the process is very tolerant to variation in laser power. The cells were isolated despite changes in the laser power by almost a factor of 5.

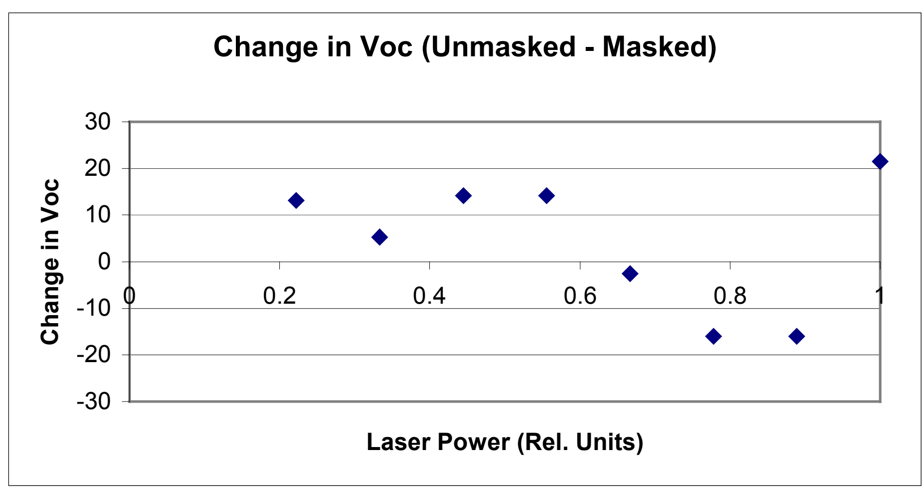

Figure 6.9. Change in average V_{oc} values of a device between surrounding cells masked and unmasked for front contact scribes done at various laser powers settings.

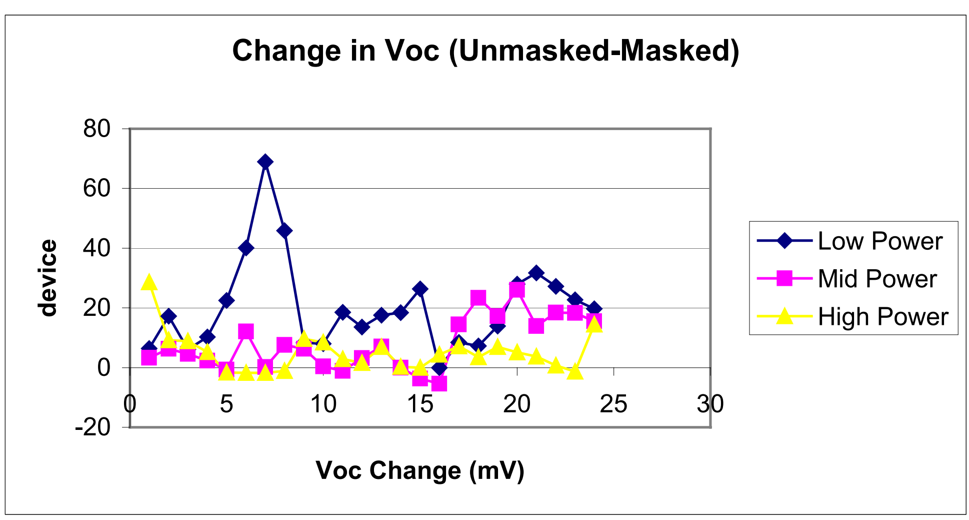

Figure 6.10. Change in V_{oc} of individual cells (unmasked-masked) for the highest, lowest and middle power studied for front contact scribe process tolerance.

Scribe morphology over that range appeared adequate and, in general, only the scribe width changed slightly. In each case the front contact material could be completely removed and the underlying CIGS left largely intact. Only in looking at the individual data points for each cell did it become apparent that variability was beginning to increase at the lowest laser power settings (Figure 6.10). Given the wide process window for laser power, we fully expect the process to be tolerant of variation in front contact thickness as well.

6.6 Conclusions and Future Work

Remarkable process robustness has been demonstrated during Phase 2 for both the back contact and front contact scribing processes. All laser scribes (P1, P2 and P3) have been validated on a production laser scribing system through electrical tests for proper function. Improved capability has been added to the scribing equipment, the level of automation has been increased. Remaining work includes characterization of the scribing processes in even greater lot sizes and software augmentation to improve throughput. The process window for the via (P2) process must be studied over a greater range of laser powers and must also be evaluated for tolerance to variation in absorber layer thickness.

7. Task 7 – Ink-Jet Technology for Insulator Deposition

7.1 Introduction

The post-absorber laser scribing approach described in the last section requires that an insulating material be deposited over the back contact scribe (see Figure 6.1), preventing direct shunt formation upon subsequent deposition of the TCO front contact. Screen printing is the technique conventionally used to deposit insulating material in the scribe, but suffers from several drawbacks. Silk screen printing typically produces 250 to 1000 µm line widths, which cause significant module area loss. Additionally, the screens stretch with use, causing registration errors and further loss in module area and manufacturing yield. Silk screen printing is also inflexible in that even small pattern changes require fabrication of completely new screens.

Ink-jet technology was proposed as a method for controllably printing scribe areas with insulating lines while circumventing the limitations of screen printing. Conceptually, a single head or multiple heads capable of controllably dispensing a fine line of insulating material could be positioned and moved rapidly over a substrate scribe area to generate a printed fill pattern.

Several types of ink-jet technologies exist, including "bubble-jet", electrostatic/ultrasonic ink drop, and valved fluid dispense through an orifice. Each method is constrained by different limitations, such as speed, ultimate linewidth, or required fluid characteristics. For instance, the electronic/ultrasonic ink drop delivery is capable of very high printing speeds, but can dispense very limited types of fluid, having strict requirements on viscosity, surface tension, electrical conductivity and vapor pressure.

Drying or curing time is also an important parameter for the printed insulator materials, as rapid processes for module production are needed for high throughput. Success in this task depends on developing the equipment and process for rapidly depositing and drying insulating ink that is compatible with subsequent processes.

7.2 Task Objectives

For the GSE scribing approach, it is necessary to deposit an insulator into previously cut back contact scribe to prevent two issues: 1) a direct shunt between the front and back contact and 2) reconnection of separated back contacts. Depositing insulating lines by ink-jet offers significant potential advantages of reduced area loss as well as increased pattern accuracy and flexibility compared to baseline screen-printing processes.

Key issues for insulator deposition are:

- line width and accuracy of the ink-jet deposited material,
- line continuity and uniformity of the ink-jet deposited material,
- overall process speed, including deposition rate and post-deposition curing time,

- insulating material compatibility with subsequent processes, and
- insulating material properties of outgassing, adhesion, shrinkage, and resistivity.

GSE is developing ink-jet technology for low loss, flexible pattern deposition of insulating material over scribes. Key goals of this task include:

- Assure reproducible, continuous, well adherent lines of insulating material with uniform line widths.
- Obtain progressively decreasing line widths, down to 125 µm, maintaining line continuity and uniformity.
- Develop the equipment and methods to minimize curing time and enable deposition rates of 22 cm/sec.
- Assure compatibility; integrate with all other module fabrication processes.

7.3 Summary of Phase 1 Accomplishments

In Phase 1 feasibility was demonstrated for the technique, as evidenced by moderate numbers of deposited, continuous ink lines. The lines were deposited, (including drying time) at 30 cm/sec which exceeds the PVMaT goal, with a line width that ranged typically from 150 to 400 µm.

7.4 Technical Approach

Commercial ink-jet technology has been adapted by GSE to deposit an insulating material in a fine, continuous line from a moving ink-jet dispense head. The ink-jet deposited insulating material is applied during the first laser patterning operation (back contact and via scribe) directly in the previously cut back contact scribes, thus preventing formation of a direct short by the subsequent front contact deposition.

The largest challenge for Phase 2 was to improve equipment reliability and process robustness as the existing equipment was prone to damage, clogging and drift in alignment after only brief periods of operation. The dispense tip or associated parts would typically clog before deposition of 100 to 200 lines. Additionally the line continuity was impacted strongly by small changes in operating parameters.

7.5 Results

Equipment reliability was addressed in Phase 2 directly through a complete re-design of the ink-jet dispense head. Lessons learned from the first iteration were applied, vendors for specialized components were located and an ink-jet head that is much more robust to failure was produced. During the longest run of commercial modules of one type to date, the new ink-jet dispense equipment deposited over 16,000 lines sequentially without a failure or clog.

Although the re-designed ink-jet dispense head was critical to the dramatic improvement in reliability, upgrades and alteration of many other components was required as well. For instance, new valving and fluid handling components were evaluated and selected. Further tests

on additional insulating materials (the ink itself) having different rheological properties were also carried out in Phase 2.

Figure 7.1 below shows a typical ink-jet deposited line of insulator over a back contact scribe. In this example the sample is backlit so that the back contact scribe can be clearly seen.

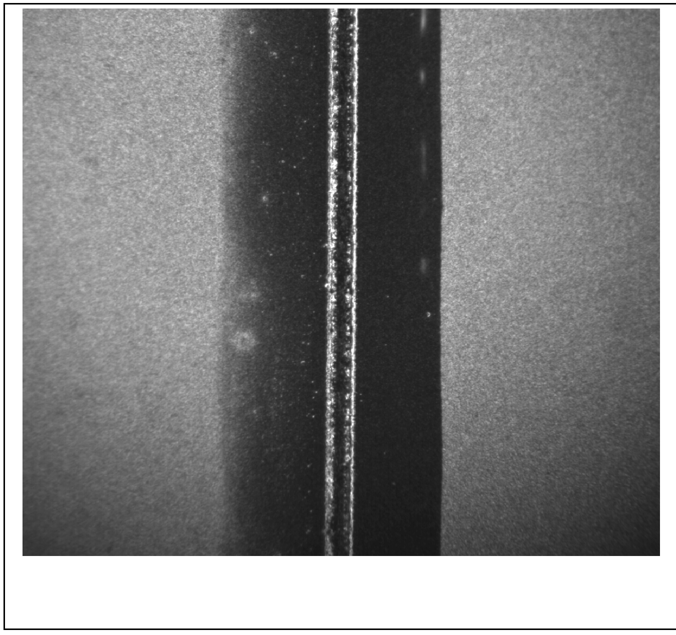

Figure 7.1. Optical micrograph of an ink jet deposited line (approx 300 μm wide) directly on top of a back contact scribe.

Registration reproducibility has also been greatly improved with the new ink-jet dispense head. Excellent reproducibility in ink line registration is a necessary factor for utilizing the smaller line widths of 150 μm spelled out in the PVMaT goals. Extremely narrow lines of insulating material can not be used if we are unable to locate them exactly over the back contact scribe.

In addition to greatly improved equipment reliability, process robustness has also improved dramatically. Previously the ink line width was very sensitive to several ink-jet operating parameters. Natural variation in some of the parameters inevitably led to large variations in the width of the deposited line, and even in complete skips or voids. With the new ink-jet dispense head, line width variation is typically ± 15% or less. Figure 7.2 below shows the variation in a random sampling of 9 ink lines deposited over the back contact scribes of module segments.

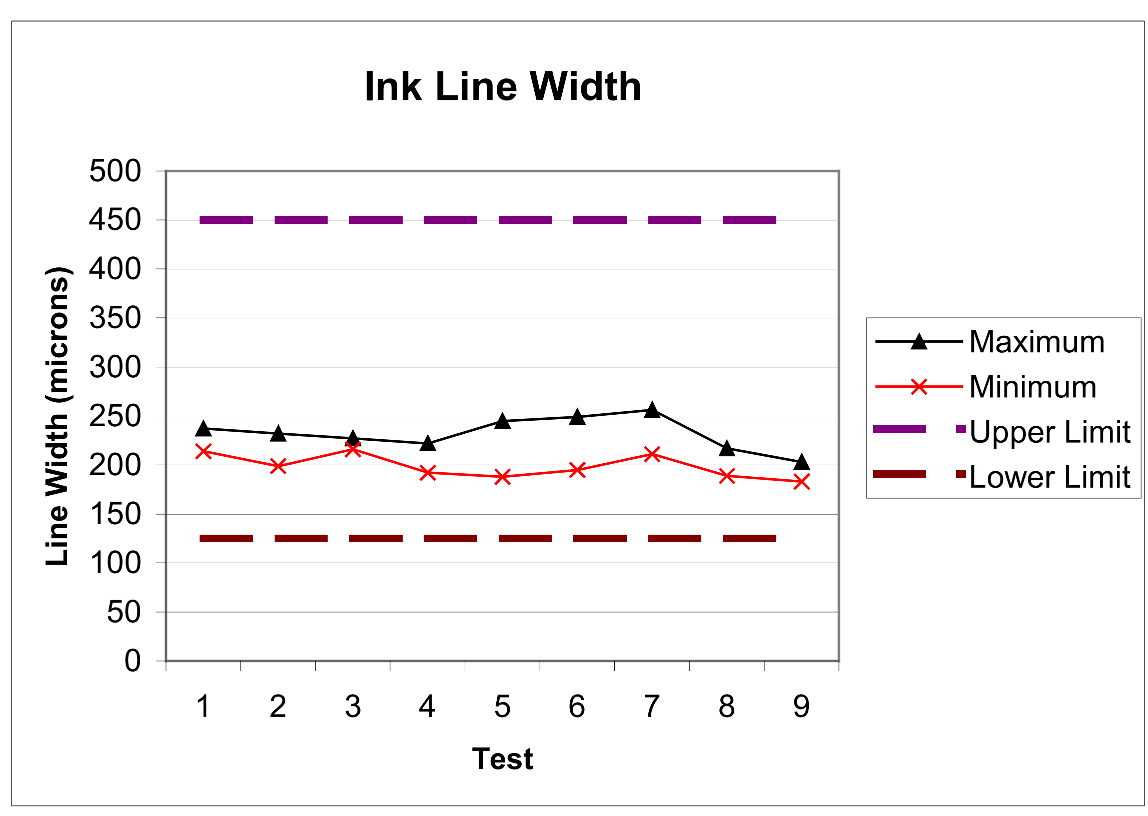

Figure 7.2. Variation of ink line width, showing maximum and minimum measured width along a random sampling of 9 module segments. Dashed horizontal lines indicate the upper and lower critical process specification limits.

Using the new ink-jet equipment, complete line skips are rare and are usually associated with problems of web hold-down or web damage.

Figure 7.3 shows a completed interconnect viewed through a finished, laminated module on flexible substrate. The module and scribes shown were selected at random from several that had been processed in a lot. Registration accuracy and automatic skew correction are sufficient to keep the three scribes parallel and well placed, however for diagnostic purposes we presently maintain a relatively large spacing between the scribes. The current equipment would allow us to substantially minimize the total interconnect width simply by changing the settings.

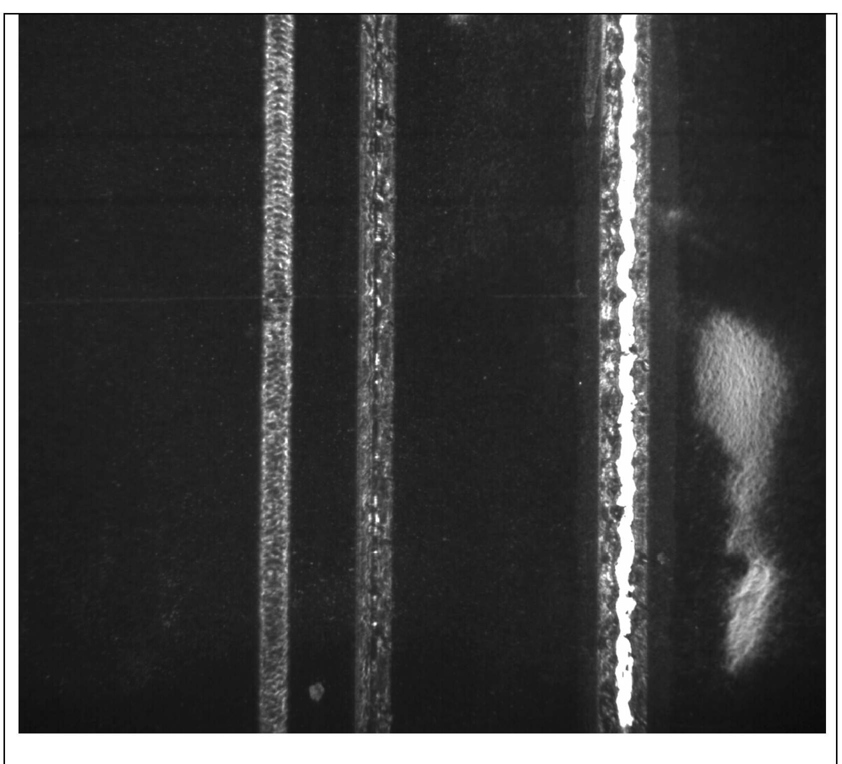

Figure 7.3. Optical micrograph of a finished module showing all three scribes of the monolithic interconnect (front, via and back contact scribes from left to right). The total interconnect is approximately 700 µm wide in this example. The irregular appearance is introduced largely by refractive effects viewing through the laminating materials.

7.6 Conclusions and Future Work

Process robustness and equipment reliability have been sucessfully addressed in Phase 2. Although ink-jet deposition of the insulating line has been developed to handle rates of 30 cm/sec with high accuracy and robustness, some further improvement is still needed. Primarily, the throughput of the ink-jet operation must be increased to better match the rate associated with the laser operations. The current plan, partially implemented, calls for multiple ink-jet heads, similar to what was accomplished with multiple laser beams for scribing. Software enhancements, including alterations for bi-directional ink-jet capability will also be added. Some improvements aimed at equalizing the operating settings for multiple ink-jet heads will probably be required. Further reduction in deposited ink-line width and decreased scribe spacing, leading to a reduction in total interconnect width will also be required to meet PVMaT goals.

8. Task 8 - High Rate CIGS Deposition

8.1 Introduction

One limiting factor for PV module throughput, and subsequent cost, is absorber deposition time. Neither the equipment nor the proof of concept exist for very high-rate CIGS deposition for use in large area thin film PV manufacturing. The challenges in this task are the high-rate, controlled, simultaneous delivery of Cu, In, Ga and Se to the substrate surface under conditions that form a dense, stoichiometric, uniform, and well adherent film of high quality CIGS. Issues including control of the Ga concentration, as well as Ga concentration profile to control absorber bandgap, impurity and defect densities, morphology, grain boundaries and surface termination are all critical to absorber layer quality, and thus also to device and module performance.

For co-evaporation processes the kinetic rate limitation on CIGS compound formation is not known. Generally high quality CIGS has been formed at relatively slow rates (>30 min. deposition time for 2 to 2.5 µm absorber thickness). However, work in some laboratories using elemental co-evaporation at high substrate temperatures (>500°C) indicates that a high quality CIGS absorber layer can be formed using 5-10 min for the metal delivery. [3-1] High-rate deposition bodes well for a rapid manufacturing process, however, the manufacturing process used at GSE introduces several additional constraints. Large area, uniform deposition of CIGS must be accomplished at GSE with process temperatures less than about 400°C because higher temperatures degrade the flexible polymer substrate. Consequently, mixing and mass transport that are dependent on diffusion are greatly reduced compared to the diffusive rates that exist at much higher temperatures when CIGS is grown on glass or metal substrates. Moreover, the intrinsic source of sodium associated with glass substrates is unavailable when using polymer substrates. Sodium incorporation has been shown to improve absorber quality and spatial uniformity of the photoresponse. [3-2, 3-3]. The formation of CIGS at high rates, with low temperatures and on polymer substrates is so far unexplored.

Photogeneration of electron-hole pairs and charge separation within the space charge region – which is located primarily inside the CIGS absorber – take place inside the CIGS, and thus it is central to photovoltaic performance. Electronic properties such as carrier concentration and mobility, defect densities, minority carrier lifetime and internal electric junction field width and strength are critical. Along with the above mentioned electronic characteristics, physical aspects such as adhesion and continuity of absorber coverage have dramatic effects on final module performance. The absorber deposition process must yield high performance material, be economical, fast, controllable and scaleable to large area.

One additional consideration for manufacturable absorber processes is selenium utilization. Although excess of Se is provided in laboratory systems to enhance CIGS growth, a 3 to 4 times stoichiometric excess of Se for continuous operation of in-line CIGS systems may increase downtime for clean-up and costs associated with waste disposal.

8.2 Task 3 Objectives

High rate deposition of the absorber layer is essential to raise throughput and reduce cost for manufacturing thin film PV. GSE is using large area co-evaporation of elemental constituents in a continuous, roll-to-roll fashion to form the thin film CIGS absorber. Key issues with CIGS deposition are:

- design of evaporative sources capable of uniform, controllable, high-rate delivery of reactants over a large area,
- electronic quality and adhesion of CIGS deposited at high rates, within constraint of low substrate temperature process,
- source heat dissipation to web and chamber, and
- materials utilization, Se delivery, and system maintenance/downtime.

GSE is developing the equipment and methods for CIGS absorber deposition at high rate. Key goals of this task are:

- Revising existing evaporative source designs capable of uniform, controllable, high-rate delivery of reactants over a large area.
- Evaluating CIGS absorber quality at progressively higher deposition rates, up to 27 cm/minutes web speed (a 100 % increase over base rate).
- Developing methods for deposition of well adherent, high quality CIGS at high rates and low substrate temperature.
- Demonstrating module production using the high-rate process.
- Incorporating high-rate absorber deposition methods and equipment into the GSE manufacturing line.

8.3 Technical Approach

The baseline GSE CIGS manufacturing process consists of direct co-evaporation from elemental sources and was selected over sequential based sputtering processes because:

- Co-evaporation allows direct gallium incorporation into the active region of the absorber even at low substrate temperatures resulting in higher band gap, and thus higher voltage per module segment.
- Substantially reduced cost because of high material utilization (70 to 80% compared to 20 to 30% for sputtering) and low cost starting materials.
- Ability to produce quality stoichiometric and off-stoichiometric compounds (i.e., transition from Cu-lean to Cu-rich and back Cu-lean within a single deposition zone).
- Process throughput for direct co-evaporation is much higher because finishing heat treatments are not necessary, and capital cost for the required deposition equipment is significantly lower.

- Direct co-evaporation from elemental sources avoids source material fabrication costs associated with making and bonding sputtering targets. These avoided costs and speed advantages take on extreme importance in a manufacturing environment.
- Compared to the elemental sputtering/selenization, direct co-evaporation has yielded CIGS material of better quality, as is evidenced by higher device efficiencies.

For large-area, high-rate vapor phase manufacturing of thin-film compound semiconductor devices, multi-source evaporation on a moving substrate (flexible or rigid) provides the best combination of performance and low-cost.

Source modeling was conducted to optimize materials utilization while achieving a uniform thickness across the web. Down web composition uniformity is achieved by the web movement through a well-defined deposition zone at a constant speed. Modeling indicated that high source utilization (>60%) required a relatively close source-to-substrate spacing.

GSE has designed and built continuous roll-to-roll CIGS deposition systems' using multi-source co-evaporation in which the substrate is transported above sources operated at a constant material flux. With specific spacing between the individual sources, the web motion creates a controllable flux profile at the substrate. Using a GSE roll coating system, adherent, uniform, stoichiometric CIGS has been deposited. GSE CIGS is single phase and exhibits a large grain morphology.

8.4 Results

8.4.1 Source Design and Operation

Several extreme requirements exist that critically affect effusion source design, the most obvious being high temperature operation for extended periods of time, material flux delivery that is uniform and well controlled, and limited heat dissipation to surrounding parts – especially polymeric substrates. At GSE we have taken innovative approaches toward meeting all the requirements for operational sources. Multiple iterations of source design or modification followed by evaluation were required to meet all of the technical challenges. Some of the technical requirements of source design are mutually conflicting, thus compromises to satisfy design issues to a satisfactory level were applied.

Much progress has been made, and sources are operational at GSE for high-rate, uniform delivery of Cu, In, Ga and Se. Even so, further improvements to the source design are expected on an evolutionary basis.

Very high source temperatures are required for mass transport of material from the effusion sources to achieve high rates, particularly in the case of Cu. The high temperatures place excessive demands on the materials comprising the source and thermocouples and can lead to undesirable heat transfer to the web. During Phase 2, one of the drivers for new source designs was the reduction of applied source power necessary to achieve a given effusion rate. A second stimulant was the elimination or reduction of deposit buildup on the exterior of the source that impacts web quality and maximum web length capability.

With these principles in mind, a new design was fabricated and tested over the course of several depositions. As predicted, the required effusion source temperature of the new source was significantly lower than that of the standard source, as validated over the course of 25 production runs. In addition, the new design substantially reduced the impact of deposit buildup on the exterior of the source (Figure 8.1).

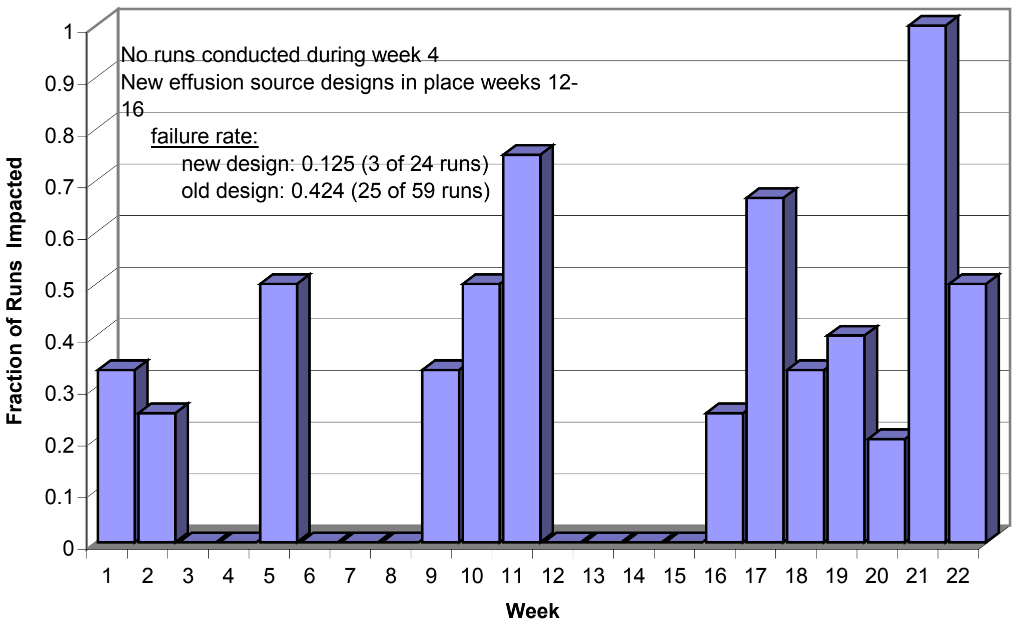

Figure 8.1. Fraction of runs impacted by nozzle blockage over the course of 83 runs.

Unfortunately, the new design promoted spitting from the Cu, In, and Ga sources. The size of Cu spits varied from 10 to over 100 μm (Figure 8.2). The density of spits was found to decrease during the course of a run (Figure 8.3). Presumably, achieving a steady state operationally and/or parametrically is beneficial to source performance. Module yield was poor when the new sources were utilized due to the source spitting. As a result, the new sources were removed from the CIGS system and the original sources were reinstalled.

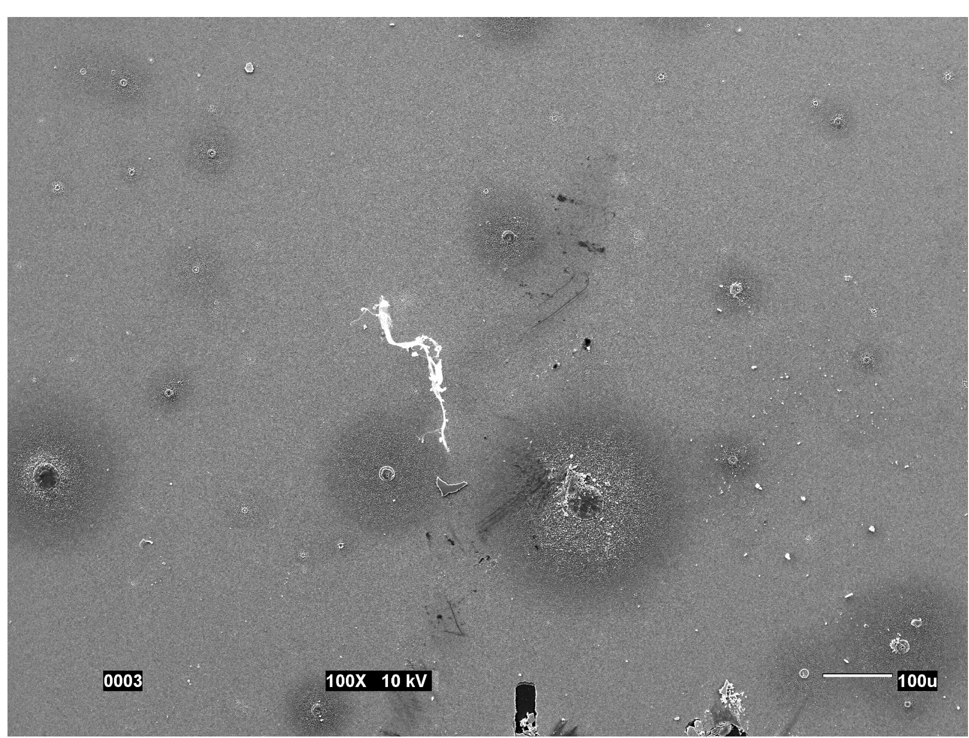

Figure 8.2. Cu spits visible on the surface of a CIGS film.

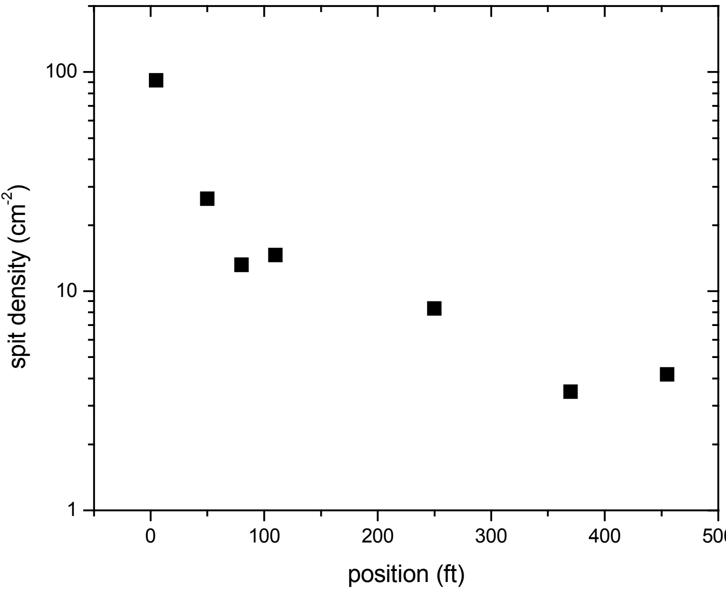

Figure 8.3. Cu spit density down the length of a web.

It was suspected that the material buildup on the exterior of the source could be associated with the Se vapor density within the deposition zone leading to gas scattering (i.e., reduction of the metal atom mean free path). A study was conducted using records of Se usage and the incidence of nozzle blockage in the GSE production system. No significant correlation between Se usage and nozzle blockage was determined.

With no apparent process levers to adjust, the operational procedures were examined for potential modification. Through trial and error, a set of procedures were developed that substantially reduced the degree of material buildup and thereby the number of lots impacted. In the process, the mechanism responsible for the buildup was better understood. The improved understanding is reflected in effusion source design modifications intended to further reduce the buildup.

Several meetings were convened during Phase 2 with participants from universities and industry (Colorado School of Mines, IEC, ITNES and GSE) to focus attention on source issues relevant to high-rate CIGS deposition. The primary goal of these meetings was to generate improved source designs. A number of designs have been fabricated for validation testing in the dedicated PVMaT 12-in web coater. The most successful designs will undergo final testing in one of GSE's production systems. The interaction of the group has been so successful that a subcontract has been extended to CSM for rigorous modeling of GSE effusion sources.

Through improvements in source design and operation, CIGS run lengths were increased considerably during Phase 2. Runs as long as 450-ft were conducted. Composition uniformity was found to be reasonably constant during these long runs as shown in Figure 8.4.

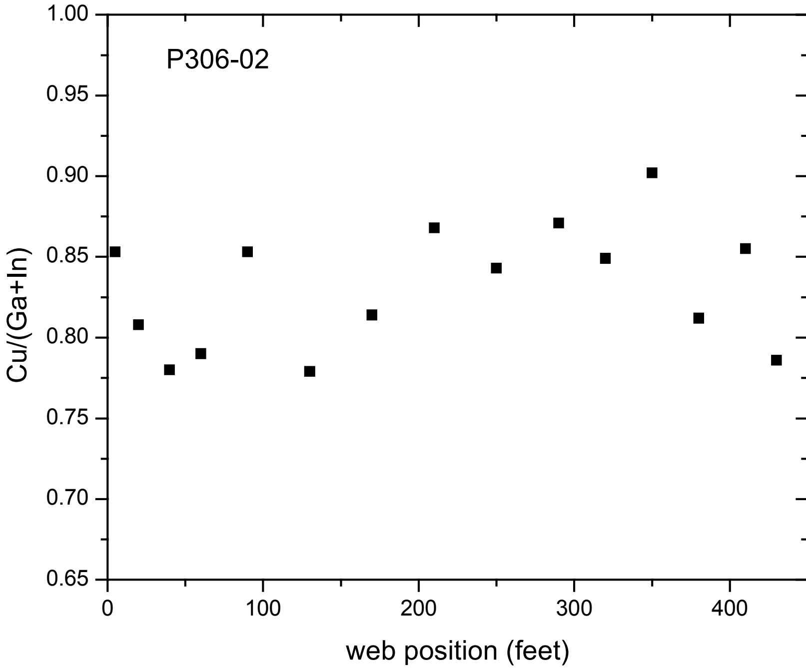

Figure 8.4. CIGS composition uniformity down the length of a 450 ft. web.

To prevent excessive radiative heating of the web from the effusion sources, it is desirable to optimize the type and amount of insulation surrounding the sources. More efficient insulation

enhances system stability by preventing thermal drift allowing extended runs without process drift. The type of insulation must be chosen with consideration of the severe temperature/corrosive environment the material will be subjected to for extended periods of time. A satisfactory material has been utilized for some time, but other materials are available with potentially lower emissivities at high operating temperatures.

Several ceramic felts and papers with desirable qualities were obtained evaluated for their insulating capabilities in the Cu source. This location is critical since the Cu source operates at the highest temperature and its facing surface provides the largest heat load to the substrate. In a typical test with a ceramic paper installed, the maximum operating temperature of Cu effusion source increased by 15-25°C. Unfortunately, the paper became brittle after use and degraded so severely that it was non-serviceable. It was a general conclusion that the ceramic felts and papers available were not up to the task because of limitations on their maximum working temperature.

A modular enclosure is used to contain the insulation. An important function of the packaging is to allow efficient removal and maintenance of the sources. The package material utilized at the beginning of Phase 2 was discovered to induce process non-repeatability due to corrosion and warping discovered as production levels were increased. A variety of materials and designs were tested for improvements. Several designs were rejected based on mechanical instability and poor insulating efficiency. The latest design eliminates most of the issues.

Tests have been conducted to optimize the amount of insulation to support high-rate deposition during long runs. The evaluations consisted of modifying the insulation on the sides and top of the effusion source and measuring the power required to maintain the source at a constant temperature. The goal of the tests was to establish the point at which additional insulation does not reduce power required to maintain the source temperature. Additionally, the tests would establish the lower power limit associated with the current effusion source configuration.

The tests were conducted in a chamber dedicated to the PVMaT program for effusion source and CIGS development on 12-in wide webs. A significant difference between the conditions used in the experimental and those found in actual operation is the absence of adjacent hot effusion sources and substrate heaters surrounding the source. Accordingly, powers required in the insulation experiments are higher than those that will be observed during production. Nonetheless a difference between the various degrees of source insulation should be and was fount to be detectable.

Standard effusion sources were employed and were filled with the quantity of Cu typically loaded during production runs. Between experiments, the source was refilled with Cu and sheets of insulation were added or removed. The source temperature was raised to 1500°C, stabilized for 15 minutes, and the applied voltage and current were recorded.

Results of tests for the insulation on the top of the effusion source (facing the web) are shown in Figure 8.5. Standard insulation layers were used on the sides and bottom. A curve fitted to the data is asymptotic with leveling out at about 2000W. As expected the first few insulation sheets are most critical, the difference between 8 and 10 sheets is only about 75W.

During experiments with the side insulation, identical numbers of insulation sheet were removed from each side of the effusion source. The top and bottom insulation layers were left at standard values. Results of tests for the side insulation are shown in Figure 8.6. A curve fitted to the data is apparently not asymptotic indicating that additional insulation layers to the side (more than 11) would have a substantial impact on applied power required.

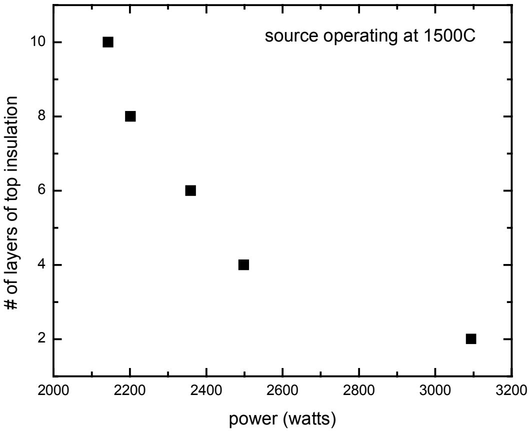

Figure 8.5. Number of top insulation layers as a function of applied power.

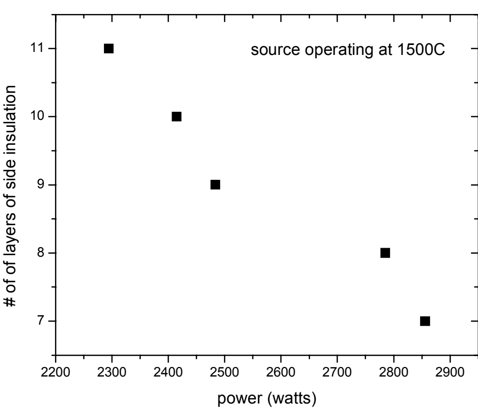

Figure 8.6. Number of side insulation layers as a function of applied power

Additional experiments were conducted to determine the power consumption of new high-rate large area effusion sources. Typical power consumption values after the sources had stabilized at the deposition temperature are listed in Table 8.1.

Table 8.1. Equilibrium power requirements of standard effusion sources

	Ga	In	Cu
Power (kW)	1.05	0.69	2.66

Tests were conducted on the effusion source in the dedicated PVMaT development system to determine run-to-run sources of variance in the characteristics of the effusion sources. In one set of experiments the impact of routine operator maintenance on effusion rates and powers was investigated. The experiment consisted of depositing a Cu film on test slides mounted on a web moving at 6 in/min. The Cu source was stabilized for 15 min at 1500°C before moving the web. The source was removed from the deposition system between tests, completely disassembled and reassembled, and then reinstalled. A small amount of Cu was added to the source to compensate for material effused during each test.

Deposit thickness was measured by stylus profilometry at nine evenly spaced locations across the web, and effusion source power by the percentage of maximum power available. Results, shown in Table 8.2, indicate that source disturbance can induce a substantial amount of variation

in effusion rate. Additional checks prior to productions runs are being instituted as a result of these tests.

Table 8.2. Summary of Cu effusion source repeatability tests

Test #	Thickness (Å)		Power
	Avg.	St. Dev.	(%)
1	1395	74	52.8
2	1686	45	53.7
3	1832	35	53.2

A separate set of tests was conducted to determine the sensitivity of source volume and levelness on the effusion rate. Once again, the Cu effusion source was utilized in these tests. The tests were conducted in the dedicated PVMaT development system 12-in R&D chamber using the standard production effusion source. The experiment consisted of depositing a Cu film on test slides mounted on a web moving at 6 in/min. with the effusion source stabilized at 1500°C.

A 2x2 matrix of tests was conducted by varying the source volume between “full” and “low” and the levelness of the source between “level” and “tilted”. In the case of source volume, “full” indicates the volume of the source at the start of a production run and “low” the volume at the finish. The difference between “level” and “tilted” represents the range that the source might actually encounter after it is set up for a production run.

Deposit thickness was characterized by stylus profilometry at nine evenly spaced locations (5 measurements each) across the test slides mounted across the web. The results are shown in Table 8.3. The tests indicate that the Cu coating thickness would drop 21% over the course of a production deposition (level source), and drop 31% for a “tilted” source, if no adjustment was made to the source temperature. The tilted sources effused less material than the level sources (15% and 26% less for the “full” and “low” conditions, respectively). One conclusion of these tests is that advanced controls must be in place to control effusion rates; maintaining a constant source temperature is inadequate. A second conclusion is that the source/source mounting structure must allow repeatable attainment of source position to help ensure process repeatability.

Table 8.3. Summary of source volume/levelness tests

Source		Thickness (Å)	
Volume	Levelness	Avg.	St. Dev.(Å)
Hi	Level	1993	126
Hi	Tilted	1689	115
Low	Level	1582	105
Low	Tilted	1170	34

Cu effusion source rate tests were conducted in the dedicated 12-in. PVMaT R&D system to establish the source behavior at rates above and below those required for the baseline process.

The test evaluation included identification and quantification of anomalous behavior that might be associated with higher effusion rates.

The experiment consisted of depositing a Cu film on test slides mounted on a web moving at 6 in/min above an effusion source containing Cu at temperatures of 1450°, 1475°, 1500°, 1525°, and 1550°C. In each case, the Cu source was stabilized at the set point temperature for 15 minutes before moving the web and exposing the test slides to the vapor flux. After the test at 1500°C the source was disassembled, reassembled and reinstalled in the system. The voltage and current applied to the effusion source was measured during each test. A small amount of Cu was added to the source after each test to compensate for the amount of Cu evaporated.

No anomalous behavior was observed during characterization of the coatings. Deposit thickness was characterized by stylus profilometry at nine evenly spaced locations (3 measurements each) across the test slides mounted on the web. Applied power was calculated from the product of measured voltage and current. Coating thickness as a function of source temperature is shown in Figure 8.7. The data is plotted as reciprocal temperature vs. log thickness in Figure 8.8. The correlation of the data to a linear fit is -0.98. The high degree of correlation indicates that there is a linear relationship between thermocouple and melt pool temperature in the range examined.

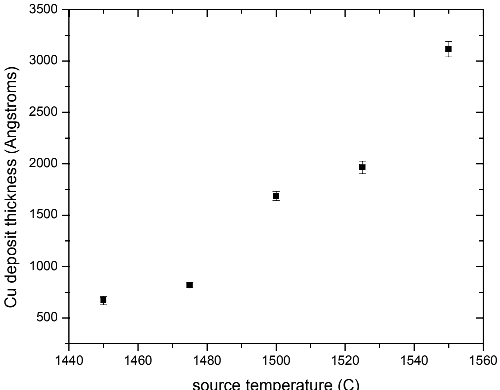

Figure 8.7. Cu deposit thickness as a function of effusion source temperature

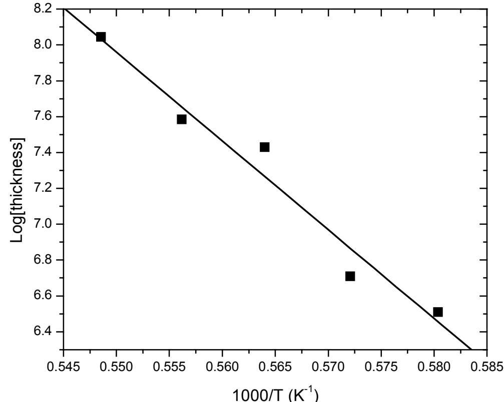

Figure 8.8. Log Cu thickness as a function of reciprocal effusion source temperature

The Cu layer thickness as a function of applied power, voltage, and current are shown in Figure 8.9, Figure 8.10, and Figure 8.11. An anomalous result was observed for the data taken at 1500°C. The data for applied voltage taken at 1500°C does not correlate with the other data, but the applied current from that same test correlates well. Plotting V/I (resistance) shows a smooth increase in resistance with increasing temperature (as expected based on the electrical properties of the heater element) (Figure 8.12), but the calculated value at 1500°C is substantially higher than expected. The removal and reinstallation of the source after the 1500°C test apparently induced a change in the series resistance of the heater element circuit. The implication is that

effusion rate control by temperature or current is superior to power due to irreproducibility in the set up procedure.

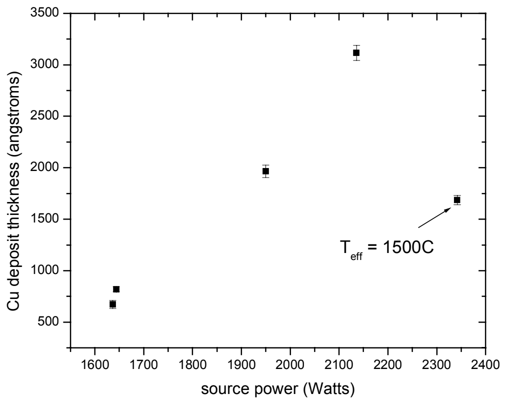

Figure 8.9. Cu layer thickness as a function of applied power

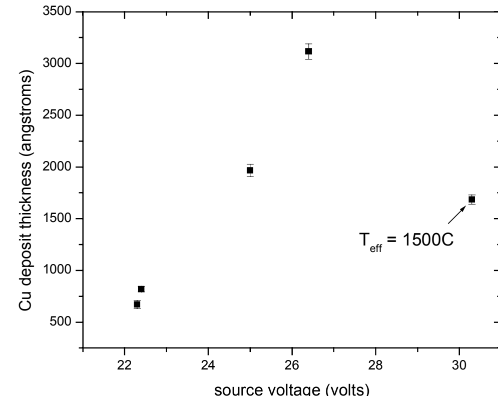

Figure 8.10. Cu layer thickness as a function of applied voltage

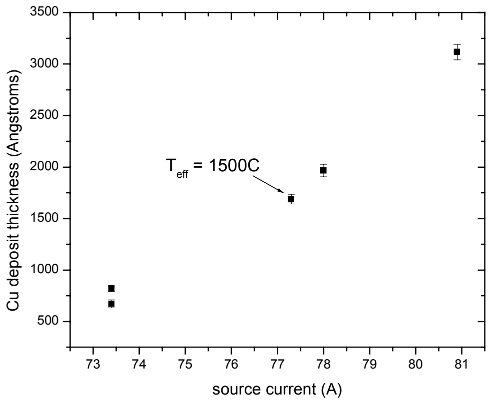

Figure 8.11. Cu layer thickness as a function of applied current

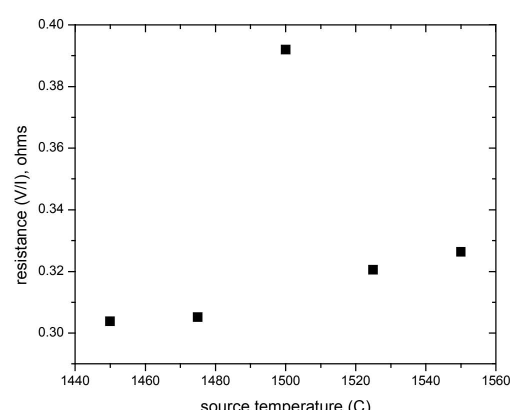

Figure 8.12. Calculated source resistance as a function of source temperature

8.4.2 High-Rate CIGS Films

Deposition experiments using the 3-stage process were conducted to determine the effect of web speed on CIGS performance. In one test (268C), the web speed was varied at 3, 6, and 12 inches/min for a total web length of 50 feet. After CIGS deposition, the entire 50-ft web was processed through the subsequent deposition operations and devices were fabricated from each section. The best devices (shown in Table 8.4) appear to indicate a falloff in efficiency with increasing web speed. The primary factor affected is the open-circuit voltage.

Another deposition experiment was conducted at web speeds of 6 and 12 in/min. (280A) (total length: 235 feet). The entire web was once again processed and devices were fabricated from each section. The device results are shown in Table 8.5. In this case, the devices from CIGS at 12 in/min were actually better than the devices at 6 inches/min., including the V_{oc} values.

Direct comparisons are difficult to make since changing the web speed requires an entirely different set of conditions with subsequent optimization (e.g., NaF, metal sources, Se). For now, maximum efficiencies and yield will have to be used to determine the upper limit of deposition rate. Once sufficient process control is implemented (in Phase 3), direct comparisons of web speed will be readdressed.

Table 8.4. Results from 268C

Web speed, in/min	$V_{oc,}$ mV	J_{sc}, mA/cm^2	Fill factor, %	Efficiency, %
12	376	33.8	56.3	7.16
6	414	35.1	56.0	8.13
3	448	34.3	58.6	9.02

Table 8.5. Results from Run 280A.

Web speed, in./min	V_{oc}, mV	J_{sc}, mA/cm^2	Fill factor, %	Efficiency, %
12	464	35.7	60.7	10.05
6	448	34.7	60.1	9.35

8.4.3 Materials Utilization

The amount of metals and Se consumed during each production run is determined by volumetric measurements. As run length is variable, the consumption is normalized to 100 feet of coated web for comparison. Over the course of 17 production runs (G428-G444), the total amount of Cu deposited on the substrates was calculated from the average Cu/(Ga+In) composition ratio and CIGS film thickness. Composition ratio was measured using EDS analysis and thickness was determined by SEM cross sectional examination of the CIGS film.

The amount of Cu deposited on the substrate was compared to the mass loss of the source to determine the utilization. Average Cu utilization over the 17 production runs, representing 4158-ft is shown in Table 8.6

Table 8.6. Utilization of Cu evaporated from the standard effusion source.

Total web length (ft.)	Avg. Cu/(Ga+In)	Avg. thk. µm	Cu mass on web, g	Cu mass from source, g	Utilization, %
4158	0.70	2.07	865	2052	42

The standard flux of Se to deposit high-quality CIGS by co evaporation is generally believed to be 3-5x the total metal flux rate. This is the result of tests conducted in laboratory systems in which the Se molecules have a greater tendency to condense on the cold chamber walls. It is also anticipated that the molecular forms of Se present – determined by catalytic reactions with the heated materials comprising the delivery system – affect Se utilization. The deposition zone geometry and the Se delivery system in the GSE production systems are significantly different from laboratory systems thus CIGS deposition tests were performed to quantify the minimum amount of Se necessary to make device quality films.

A calibration run was performed by depositing Se for 140 minutes at a crucible temperature of 415°C (G264). At a web speed of 6 in/min, this corresponded to a Se usage of 6.1 g/linear ft. During a single subsequent run (lot 275B), the Se crucible temperature was adjusted to 395°, 415°, and 435°C (random order). All other conditions were kept constant. The Se usage for each condition was estimated from the calibration run and from curve fitting published vapor pressure data for Se.

Samples were extracted from each section to examine the morphology by SEM (Figure 8.13). The films deposited at the lowest Se flux (corresponding to 395°C), had very poor morphology, but adhered exceptionally well to the substrate. The grains were poorly defined in the film with the lowest Se flux compared to the cross-sections of the films deposited with higher Se fluxes.

After processing the web as a continuous lot through subsequent processes, test devices were fabricated from each of the three sections with varying Se exposure. The best cell results, shown in Table 8.7, indicate that the current CIGS deposition process in our equipment requires as a minimum somewhere between 4.9 and 6.1 grams of Se per linear foot of web.

A stoichiometric CIGS film that is two microns thick requires 0.55 grams of Se per square foot. Assuming a Se delivery to the web is identical to that of Cu in our system (42%), the minimum required Se effusion rate to the web (atoms/time) is 3.7 – 4.7x the total metal rate. This is not significantly different from laboratory results and implies that the residence time of Se in the deposition zone is short and/or the molecular forms of Se present are not as suitable as those from the standard Se effusion sources utilized.

As a result of the relatively low utilization of Se and its impact on system maintenance and robustness, the deposition zone was reconfigured as a hot box to avoid premature condensation of the Se.

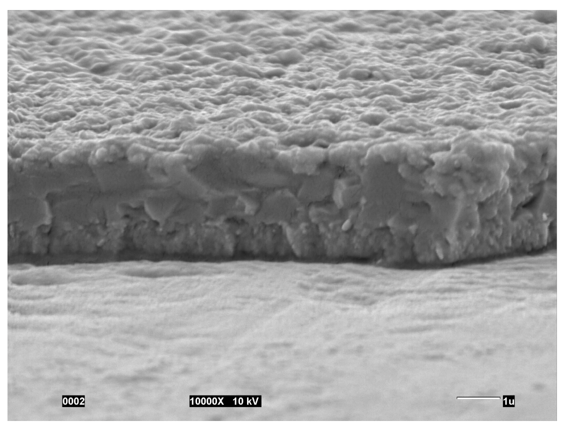

1a. 3.9 g/l-ft.

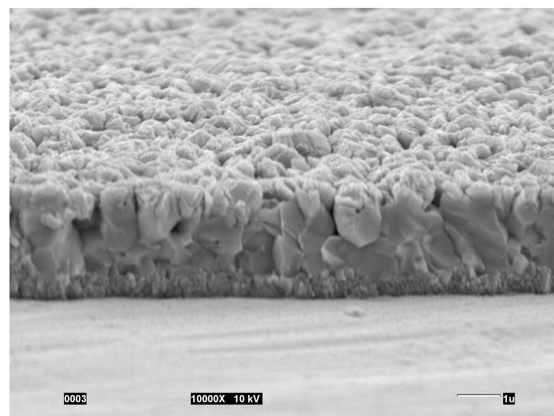

1b. 6.1 g/l-ft.

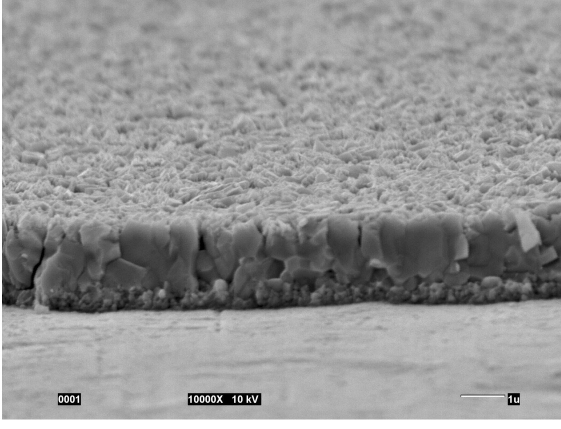

1c. 8.1 g/l-ft.

Figure 8.13. Cross sectional SEM micrographs showing the effect of Se delivery rate on CIGS morphology

Table 8.7. Effect of Se usage on device characteristics

Se Crucible Temp., °C	Est. Se usage, g/linear foot)	V_{oc}, mV	J_{sc}, mA/cm^2	FF, %	Efficiency, %
395	3.9	317	26.4	24.5	2.1
415	6.1	407	39.6	58.8	9.5
435	8.1	433	35.1	60.2	9.1

After the reconfiguration, Se utilization was determined by measuring the quantity of material consumed during each run. The Se source was refilled prior to each deposition to achieve the same starting volume. Maintaining the source crucible at a constant temperature for each run controlled the Se source rate. The amount of Se consumed in the production equipment for runs G428 to G444 is shown in Figure 8.14. As shown, significant variability was observed. A gage study was performed that indicated that only a fraction of the variability is due to measurement

error. The majority of the non-repeatability is apparently due to system and operational variability.

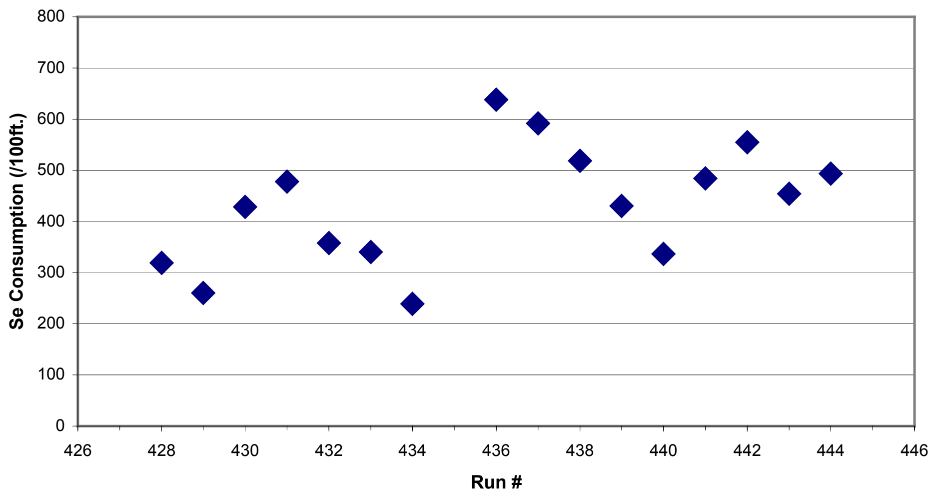

Figure 8.14. Se consumption over the course of multiple runs with nominally identical conditions.

Not long after the modification to a "hot box" was implemented, a significant variability in CIGS thickness was noted. Statistical analysis was performed and an inverse correlation between CIGS thickness and the rate of Se effused normalized to web length was determined (Figure 8.15). The increase in CIGS thickness can be explained by an increased mean free path of the metal atoms at lower Se pressure which enhances mass transport to the web. Change is thickness has important implications on CIGS material quality and Se usage. Analysis of the existing data and additional tests are required to establish a lower limit on Se required using the newly configured deposition zone. A problem confounding completion of these additional tests and controlled production in general is the difficulty in controlling the Se rate (see above). A thermal model is being prepared for the existing Se source to improve flux control.

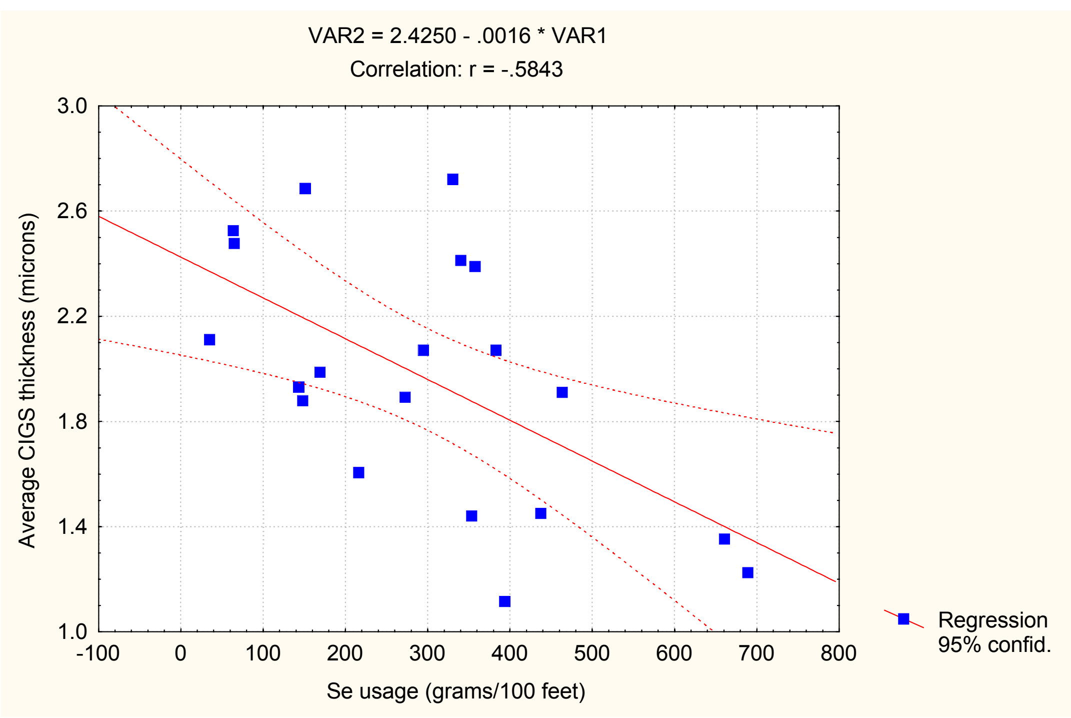

Figure 8.15. CIGS thickness as a function of effused Se mass.

8.5 Conclusions and Future Work

At GSE we have been successful in developing methods for high rate deposition of high purity CIGS using a low temperature, roll-to-roll process on flexible polyimide and stainless steel substrates. CIGS deposited in continuous roll-to-roll process is of reasonable quality, as indicated by device results, even at substrate rates that exceed the PVMaT end-of-contract goal. The aspects of this task associated with the highest risks (scaled-up evaporative source design and very high rate CIGS formation) have already been attacked, with good result. Deposition of CIGS by co-evaporation at very high rates over large areas appears to be viable.

The design and use of effusion sources will continue to undergo evolutionary modification to further improve CIGS uniformity, control, film composition and device efficiency. Although the adhesion of the CIGS has been acceptable under many conditions, more work is required to fully understand the factors involved, including interaction with the back contact. Systematic experiments must begin to determine the dominant causes affecting CIGS/back contact adhesion.

More work is required to extend the operational control and reliability of the CIGS deposition components, including the sources, to attain longer runs of roll-to-roll material. Work here will also likely involve means to thermally stabilize the deposition environment over longer periods of time.

9. Task 9 - Absorber Layer Diagnostic Development

9.1 Introduction

Fundamental mechanisms underlying processing and materials performance relationships in more complex and dynamic thin film structures, may not be revealed in post-processing measurements. For these cases, effective feedback process control is critical and underscores the need for real-time measurement and interpretation of system parameters. Although process models and simulators enable development of effective process reactor designs and model-based control strategies, real-time sensing and control of critical process and product variables is required to accommodate unanticipated process upsets, reactor variability/drift, and perhaps allow operation in physically unstable processing regimes where repeatability can be achieved only through dynamic feedback/feedforward control.

For *in-situ*, real-time thin film property measurements, it has been particularly useful to concentrate on the polarization state of light reflected from deposited films, and how this is modified through the interaction with the sample. A spectroscopic ellipsometer (SE) sensor that we are developing has the potential of measuring several thin film properties simultaneously, such as thickness, composition, and resistivity, and providing the real-time sensing required for effective CIGS process control. Unlike conventional ellipsometers, which measure the intensity of the reflected polychromatic light for each polarizer orientation, our SE utilizes carefully selected polarization states (intensities) to determine complex reflectance and/or ellipsometric amplitude (Ψ) and phase (Δ).

The amplitude and phase change parameters (Ψ, Δ) obtained in ellipsometry can also be expressed in terms of the changes upon reflection in the angular orientation and ellipticity of the polarization ellipse associated with the incident wave. Unlike a reflectance measurement, which only provides the ratio of reflected to incidence irradiances, an ellipsometer can extract both real and imaginary parts of the dielectric function, (ε_1,ε_2), as a function of the photon energy, ($h\nu$), from the (Ψ,Δ) measurement.

9.2 Goals

The equipment and methods for real-time*, in-situ* intelligent control using Parallel Detector Spectroscopic Ellipsometry (PDSE) are being developed. The key goals of this task are to:

- Demonstrate that the PDSE method is sensitive to, and predictive of the crucial electrical and physical properties of the CIGS absorber material.
- Design and install practical PDSE equipment on laboratory scale reactors, and finally on production equipment.

- Develop a robust, practical algorithm to reduce raw data to information that is uniquely predictive of the important electronic and physical qualities of the CIGS.

Even though our SE sensor has been shown to have a simple architecture, its true real-time processing capability is still dependent on the development of an efficient spectra-structure transformation algorithm(s) to handle the large dimensionality of the input parameter space/data set. In addition, with the advent of high-speed microcomputers and efficient end-point predictor, we intend to extract meaningful interpretations of ellipsometric data so as to be practically simultaneous with the measurement.

The specific goals for Phase 2 are to:

- Collect and analyze SE data from different CIGS films with properties that have been intentionally varied.

- Installation and testing of the PDSE in a CIGS deposition chamber.

9.3 Summary of Phase 1 Accomplishments

Based on an original design crafted to overcome some of the intrinsic limitations of conventional ellipsometry instruments the design and construction of the individual system components for the PDSE was completed in the first phase. The SE was designed to provide reliable measurements of the CIGS films from a flexible moving support.

9.4 Summary of Phase 2 Accomplishments

The assembly of an operational PDSE system was completed in the fall of 1999. Testing of the PDSE to acquire calibrated data and to be able to realign to maintain the calibration was also completed in Phase 2. The PDSE acquired data with as much or more accuracy and precision as a state-of-the-art analytical spectroscopic ellipsometer. A calibration procedure has been defined that is flexible enough to allow changes based on materials and other geometrical concerns that might arise once the PDSE is installed in the production CIGS chamber. Once the initial *ex-situ* testing was performed with the PDSE, it was installed and operated in a prototype CIGS vacuum deposition chamber. The PDSE provided real-time, *in-situ* SE measurements in vacuum condition to 10^{-6} torr with the external and internal optical and electronic components at 70ºC. Using the results of this initial *in-situ* testing, a design has been finalized and construction has begun on the PDSE hardware that will be installed in the 15 inch web production CIGS vacuum deposition chamber.

Spectroscopic ellipsometry measurements and analysis was performed on 13 CIGS samples provided by IEC. Initial modeling of the measured data has proved to be very challenging but indicates that SE can provide the type of film property information that will be needed for real-time process control. Besides all the film property information that can be obtained from a detailed evaluation of the SE measurements, the initial data analysis indicates that we may be able to use the “raw” real-time data to provide information about the film quality, the bandgap (and thus the composition) and the surface roughness. Based on these initial results, transformation algorithms

are being developed to convert the SE data to quantified information for process control. Ultimately, a next generation, 'smart' interpretive algorithm(s), may be developed and applied to the CIGS processes that can provide additional information about the film properties, but this will require a significant increase in the present research and development effort. In either case, both approaches will need to be validated for the CIGS deposition process.

9.5 Task Objectives

Diagnostic development is necessary to enable real-time control during the absorber deposition for the extended times necessary to process up to 1000 ft of substrate. Cost and yield improvements will result from better control of the CIGS properties in the roll-to-roll process. Key issues with intelligent control of the absorber layer deposition are:

- Sensitivity of diagnostic method to key electronic and physical CIGS properties.
- Sensor robustness, reliability and suitability to *in-situ* deposition conditions.
- Algorithm for data reduction to meaningful and predictive output, data collection speed for real-time operation.

Specifically, the task for this Phase 2 effort is to perform SE measurements of CIGS films with significantly different properties and to install and test the PDSE in an actual CIGS vacuum deposition chamber.

9.6 Technical Approach

As discussed above, ellipsometry is a unique technique in that the real and imaginary parts of the dielectric function can be extracted directly as a function of photon energy. For the homogeneous, layer-by-layer growth of a perfectly uniform transparent or absorbing film on an ideal, fully characterized substrate, real-time ellipsometry at a single photon energy has been shown to provide the dielectric function of a film along with its thickness. The dielectric function, $\varepsilon(\omega,K)$, which describes the response of a material to an electromagnetic field has significant consequences for the physical properties of a solid. It depends sensitively on the electronic band structure (and other physical properties) of a material and studies of the dielectric function by optical spectroscopy (multi-frequency response) are very useful in the determination of a material's overall band structure.

Several spectroscopic ellipsometry systems have been designed for *in-situ* process monitoring. Some can be purchased as an integrated device. However, there are no spectroscopic ellipsometers currently available (either commercially or in any reported development laboratory) that acquire all of the necessary information in a single, instantaneous sampling; nor are these systems cheap. Since no spectroscopic ellipsometer with appropriate capabilities is commercially available, we are developing a novel Spectroscopic Ellipsometer sensor for in-line, real-time control of CIGS manufacturing processes. The SE sensor we are developing has the potential of measuring several thin-film properties simultaneously, such as thickness,

composition, and resistivity, and providing the real-time sensing required for effective CIGS process control (spectroscopic data can now be acquired in parallel over a wide photon energy range in less than 20 ms).

To complete the goals of the Phase 2 effort, we have designed, constructed, tested, and installed a PDSE into a CIGS vacuum deposition system. We have also acquired CIGS samples with different film properties and performed detailed analyses using SE. The results of this work have been used to complete the objectives of the Phase 2 effort and provided a good foundation for proceeding to the Phase 3 work.

9.7 Results

9.7.1 PDSE Hardware Development

While most of the initial hardware design and construction was completed in Phase 1, implementation of the PDSE into a CIGS deposition chamber required additional design modifications and construction of other vacuum compatible components.

9.7.1.1 Hardware Installation in CIGS Vacuum Deposition Chamber

A PDSE using spectrometers that operates with visible light is presently operational and has been tested in a prototype CIGS deposition chamber. Figure 9.1 shows the PDSE in the vacuum chamber after several CIGS deposition trial runs. The PDSE provided real-time information about the sample being measured in vacuum at 10^{-6} torr with the source and substrate heaters on. Under these conditions the PDSE reached an operating temperature of 60 to 80 ºC. The temperature inside the vacuum chamber resulted from operation of both substrate and source heaters. The construction of the PDSE to go into the vacuum deposition chamber involved many modifications of the original design and construction of fiber optic feed throughs, electronic feed throughs, mounting brackets, and heat shielding. To minimize Se deposition on the PDSE optical surfaces, an active purge system was designed and installed on the PDSE hardware. Presently, we can control the purge rate sufficiently to limit overall chamber increases to below 1 x 10^{-7} torr. Based on these initial test results of the PDSE in the vacuum deposition chamber, a more robust PDSE design has been completed and construction has begun on a system for installation in a production CIGS deposition system.

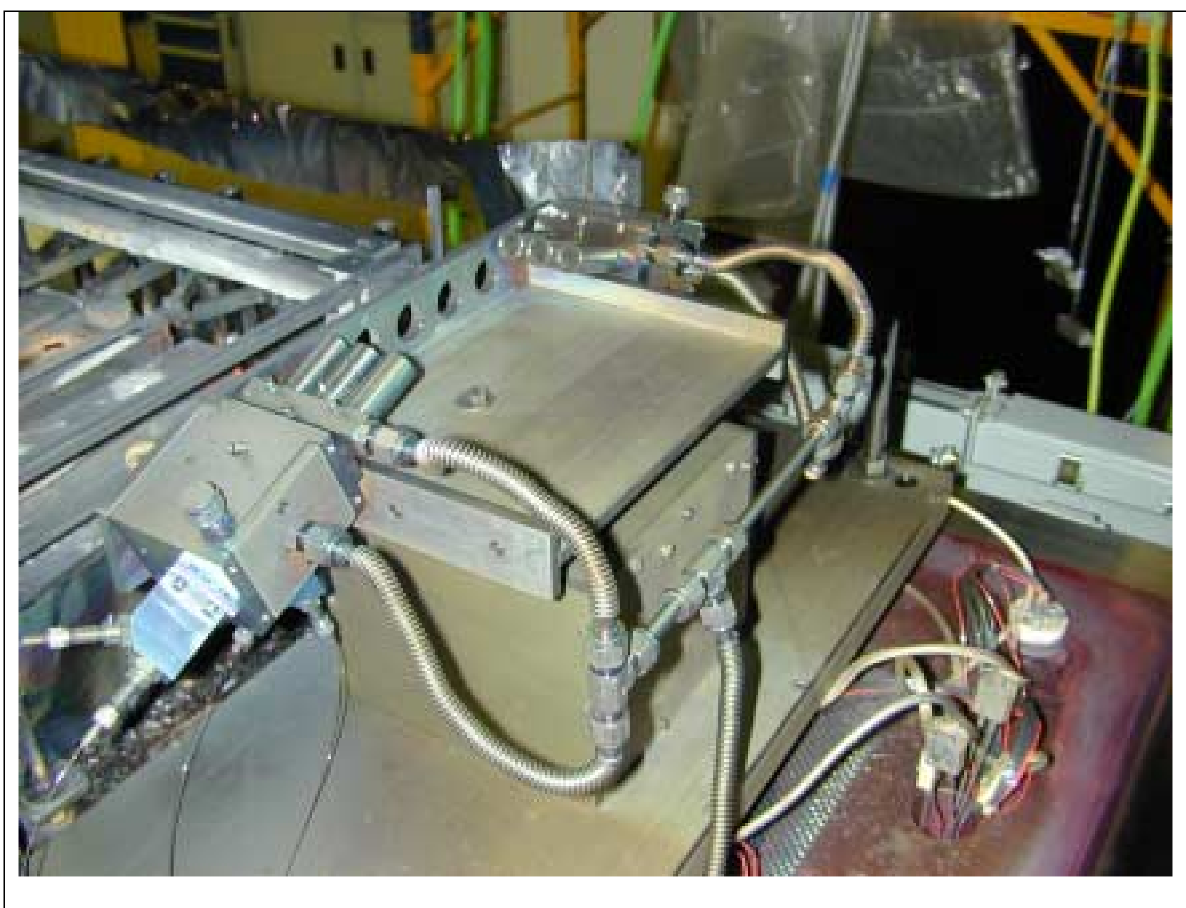

Figure 9.1. Picture of the PDSE in a prototype CIGS vacuum deposition chamber. The optical fibers and wires for the electronics pass out of the vacuum chamber in feedthroughs in the bottom right of the picture. Flexible tubes carry nitrogen to the optical components to keep Se from depositing on the cooler surfaces.

9.7.1.2 PDSE Calibration

A calibration procedure was designed and implemented for the PDSE that fully defines an instrumentation matrix of the four-plex spectrometers. Software code was written to perform the necessary tasks for calibration of the PDSE detection head. With this code a scheme was identified that eliminated geometrical effects and provides an excellent calibration of the detection head and an appropriate instrument matrix that converts the raw data to the polarization parameters of S_0, S_1, S_2, and S_3 (Figure 9.2). Additional software was written to numerically fit the calibration data and convert the stokes vectors to the standard ellipsometry parameters of Psi, Delta (Figure 9.3), or Epsilon 1 and 2, etc.

Figure 9.2 shows the normalized stokes vectors for the PDSE detection head from 400 to 800 nm. The data are exactly what is expected based on the polarization of the incident light (45°, 65°, 90°, and right and left circular, respectively). Comparison of the spectroscopic ellipsometry data shown in Figure 9.3 indicates that the PDSE provides equivalent information to the Woollam spectrometer from a Si sample.

Figure 9.2. Normalized tokes vectors from the PDSE with incident light at different polarizations.

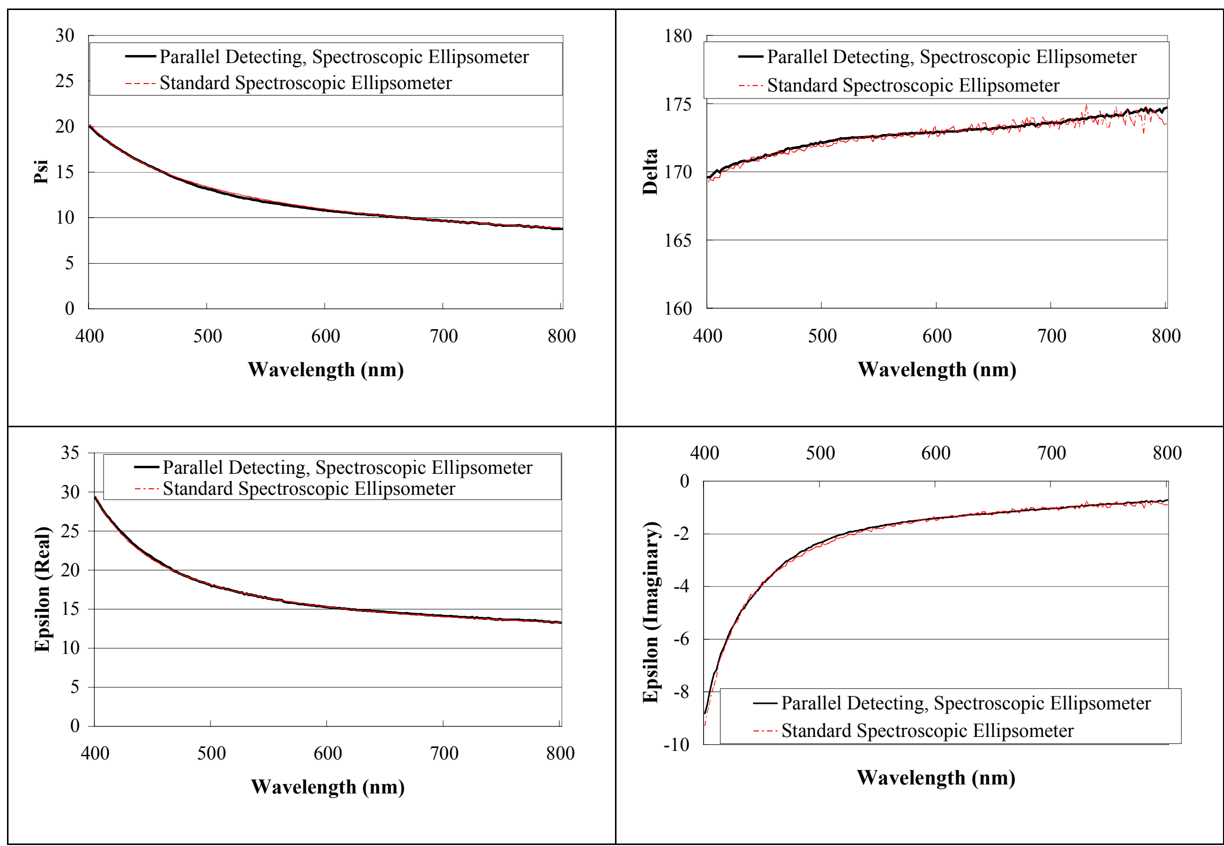

Figure 9.3. Comparison of Si optical properties measured with a standard commercially available spectroscopic ellipsometer and the PDSE. The PDSE data was acquired with a 15 ms integration time for the spectrometers compared to the 10 to 15 minutes required to obtain the spectra from the standard spectroscopic ellipsometer.

9.7.1.3 PDSE Alignment

Alignment of the PDSE is critical to its proper operation. The information extracted from the device is contained within the relative intensities of the four detection channels. Any geometrically related intensity variations are indistinguishable from sample-derived information. Our current alignment strategy uses crossed laser beams and quadrant photodiodes. Initial tests have been completed on this present alignment strategy. The initial design had both lasers and quadrant photodiodes in the PDSE source and detection heads. However the heat inside the deposition chamber adversely affected the electronic components. Therefore, the laser light was introduced through a optical fiber and an imaging fiber bundle is used to preserve position sensitivity of the laser spot after it is reflected off the sample and to transport that laser spot to the quadrant photodiode. With this new optical fiber based laser delivery and detection strategy, the laser, quadrant photodiode, and accompanying electronics can now remain outside the harsh environment of the deposition chamber.

Investigations into New Alignment Strategies

As part of our efforts to continuously improve the intrinsic PDSE design, we have been investigating alternative approaches for several of the components including alignment. The present crossed polarizer system suffers from not being directly correlated with the white light beam that is really the important component of the system. Furthermore, electronic noise is a constant problem that needs to be taken into account. A new strategy that is being investigated for implementation in future PDSE systems is to exploit the built-in geometrical sensitivity of the white light beam itself to establish an alignment signal. This should work, since the diffuser screens create a broad angular distribution of light that is anisotropic, favoring the forward direction. With misalignment, the portion of this distribution that is sampled by the fiber changes. The key is to find ways to identify the characteristics of this variation so as to establish a clearly identifiable aligned condition. This scheme has the significant advantage of simplicity and not requiring additional sources, or detectors.

In order to effectively utilize this effect the incident beam must first be depolarized. Depolarization serves two important roles. Primarily it eliminates all but the geometric effects of sample orientation and secondly it improves accuracy by ensuring that all detector light paths are used. One might assume that proper alignment could be achieved by locating a maximum luminosity position. There is however a large amount of both fluctuation and drift in such a measurement which makes it unsuitable for alignment purposes. The cause of such fluctuation and drift is difficult to isolate and surely harder to eliminate. In contrast to total luminosity, the relative intensities in each of the spectrometers are remarkably stable.

Our initial investigation yielded promising results (Figure 9.4). Starting from a predefined alignment position the head assembly was swept along both independent rotational axes while the relative intensities were recorded. Regardless of which axis was varied we found parabolic peaks in spectrometer channels 1 and 3 and corresponding minimums in channels 2 and 4. Further investigation involved rotating the heads off alignment along one axis and then sweeping the second axis through its alignment position. Some small interdependence was noticed during these limited tests but there was still little if any angular separation seen between the peaks in channels 1 and 3 or the minimums in channels 2 and 4. Consequently we sought to both expedite and simplify alignment by reducing the 4 relative intensities to a single alignment index (obtained by summing the relative intensities in channels 1 and 3 and subtracting the relative intensities of channels 2 and 4). Alignment was then to be obtained simply by maximizing this number by rotation on one axis and then repeating the procedure for the second axis.

A more thorough test of this method however revealed a strong (although essentially linear) interdependence between the rotational axes. This interdependence is such that we can specify with precision alignment only along one rotational dimension. This does not in any way preclude alignment by relative intensities however since by creating the single index we were essentially limiting our available information. The fact that utilizing only this single index has eliminated one rotational axis is encouraging since we have now only to find a second axial and a single translational dependence with our four available channels. A complete sampling of all four channels through all three degrees of freedom will be our next step. We are hopeful that this will yield a simple solution through individual or joint variance of relative intensities.

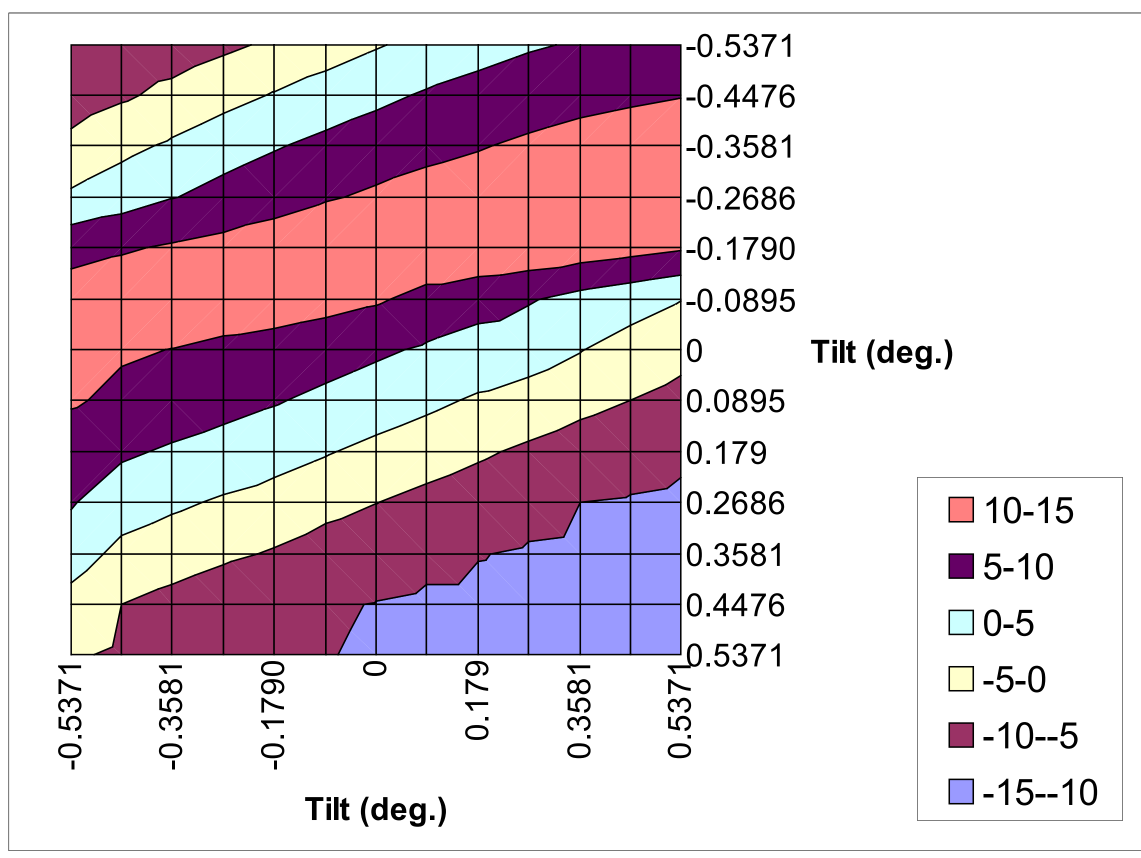

Figure 9.4. Relative intensity alignment index multiplied. The index is derived by subtracting the number of counts of the two smallest spectra from the number of counts from the two largest spectra, dividing that by the sum of the counts from all four spectra, and multiplying by 100.

9.7.1.4 PDSE IR Spectroscopy Development

Unlike the visible "CCD" based spectrometers that are commercially available in multiple spectrometer configurations that allow simultaneous data collect from all four spectrometers, the available IR spectrometers can only be operated one at a time with commercially available software drivers and configurations. The present state-of-the-art IR spectrometers will soon be available with PCI compatible computer cards. We have ordered these new PCI cards and once they arrive it should be possible to build the software necessary to operate more than one IR spectrometer at a time. We anticipate receiving these new cards in the next month. In the interim, since each IR spectrometer is approximately $15,000 each, it may be very advantageous to be able to collect IR data with a single IR spectrometer, even if we eventually use four IR spectrometers on for process control of the production CIGS chamber. This will require an optical fiber switch that can be controlled and delivers light from the four different PDSE optical fibers to a single IR spectrometer and to take the data serially to obtain all the data needed for ellipsometric measurements.

Initial attempts to purchase a small 100 μm based fiber optic switch did not work for the PDSE application. The small optical fiber limitation reduced light throughput too much and the switch never operated with enough reproducibility for the PDSE application. Attempts to use division of amplitude and division of wavefront based (approximately 15% throughput) optical fiber switches also failed due to low light throughput. After extensive searching, no commercially available switch with higher throughput efficiency could be found to meet our needs. Therefore, initial design and construction of a mechanical switch that rotates one of the four fibers and aligns it with the detector has been completed. This type of switch should provide better than 95% throughput with 1000 μm diameter optical fibers but needs to reproducibly align the fibers multiple times.

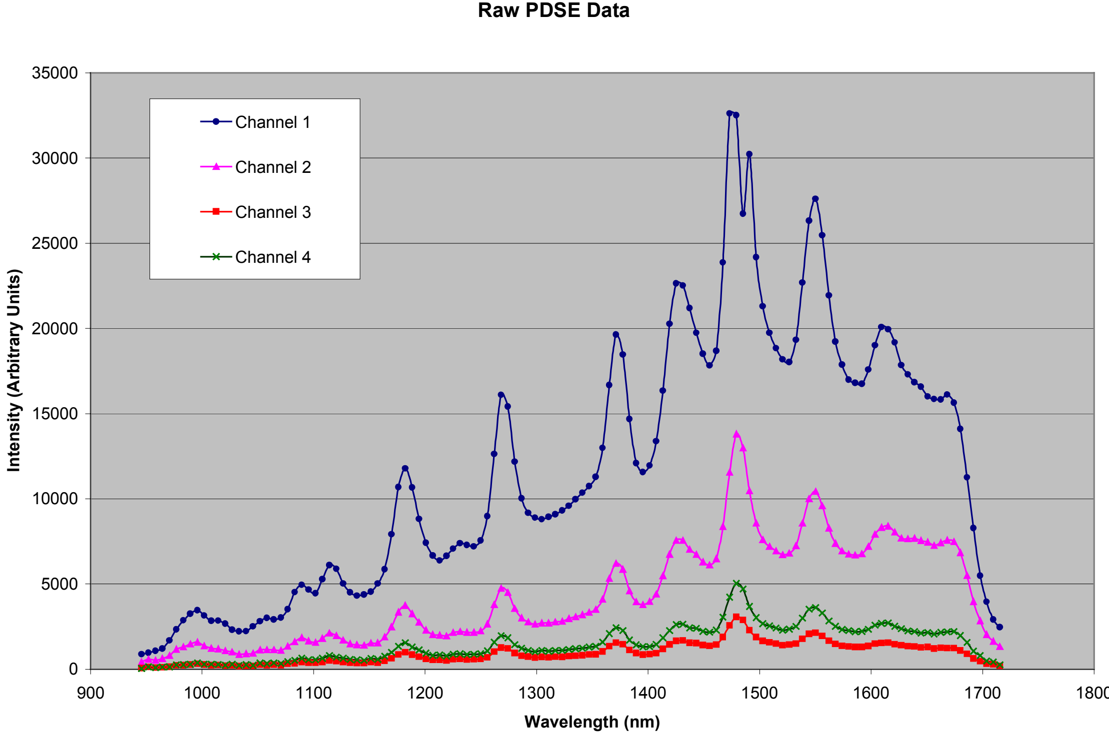

Figure 9.5. Raw intensities from Si measured with the PDSE in the IR region between 900 and 1700 nm.

All the parts for the optical switch have been delivered and assembled. An initial program was written to operate the switch separately, however a significant amount of additional programming will be needed to incorporate the optical switch into the present and future PDSE software. For the first time, four IR spectra from ~900 to 1700 nm were obtained from the PDSE (Figure 9.5) without disconnecting and reconnecting optical fibers. The initial indication is that the switch components provide reproducible alignment of the fiber optics with enough accuracy to allow data collection for the PDSE and to calculate the stokes vectors. The next step will be to collect actual IR data from samples and compare that data to known results.

9.7.2 Spectroscopic Ellipsometry Analysis of CIGS Thin Films

To develop the transformation algorithms needed for real-time conversion of the SE data to process control variables, detailed analysis of CIGS films with different properties must be performed. Thirteen CIGS samples deposited on Mo-coated (~1 μm) soda lime glass substrates were provided by IEC to be analyzed with spectroscopic ellipsometry. The specific compositions, substrate heater temperature used during deposition, and film thickness for each sample is shown in Table 9.1.

Table 9.1. Measured composition and thickness of CIGS Films. The composition was measured with EDS and the thicknesses determined by substrate mass gain.

Sample #	Cu (%)	IN (%)	Ga(%)	Se(%)	Cu/(IN+Ga)	Ga(In+Ga)	Tss (C)	Thickness (microns)	Comment
32876.22	23.0	19.2	7.7	50.2	0.86	0.29	550	3.1	Baseline
33157.2	22.5	17.2	8.2	52.1	0.89	0.32	550	2.8	Baseline
32983.22	24.4	17.7	8.5	49.5	0.93	0.32	550	2.8	Baseline
33021.21	26.6	17.6	6.3	49.5	1.11	0.26	550	3.1	Higher Cu
32823.21	30.9	16.9	5.1	47.2	1.41	0.23	550	2.5	Higher Cu
33018.21	19.9	19.8	7.7	52.6	0.72	0.28	550	2.9	Lower Cu
32897.21	16.8	21.6	9.7	51.9	0.54	0.31	550	2.7	Lower Cu
32988.33	22.6	14.6	12.4	50.4	0.84	0.46	550	3.2	Higher Ga
32991.33	21.5	10.6	16.5	51.4	0.79	0.61	550	3.1	Higher Ga
32893.33	22.8	17.6	7.7	51.9	0.90	0.31	550	1.5	½ thick.
32889.21	26.7	16.3	8.0	49.1	1.10	0.33	550	1.4	½ thick., high Cu
32909.22	24.0	19.2	9.0	47.9	0.85	0.32	400	2.9	Low T (small grain)
33125.21	25.9	16.2	7.3	50.6	1.10	0.31	400	3.0	Low T, high Cu

9.7.2.1 Spectroscopic Ellipsometry Measurements

Spectroscopic ellipsometry parameters Psi and Delta from the 13 different CIGS samples were measured at three different incident angles. Figure 9.6 to Figure 9.10 show the data from some of these measurements. Initially, we have performed a general "top level" type analysis of the SE data from the CIGS samples to demonstrate the type of information that can be obtained with SE measurements quickly without detailed modeling. Additional modeling will be performed to analyze, and quantify the results from the SE data.

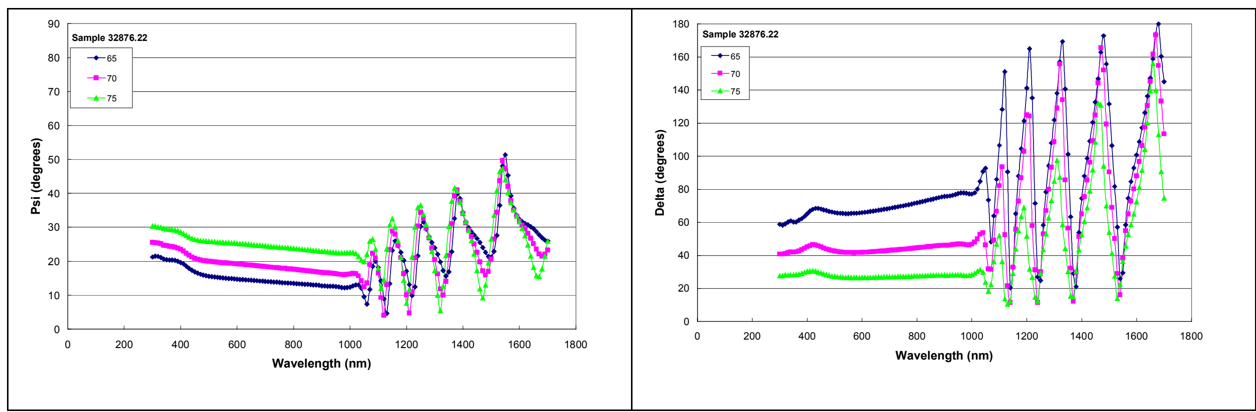

Figure 9.6. Measured spectroscopic ellipsometry parameters Psi and Delta from baseline CIGS sample 32876.22 for incident angles 65, 70, and 75 Degrees.

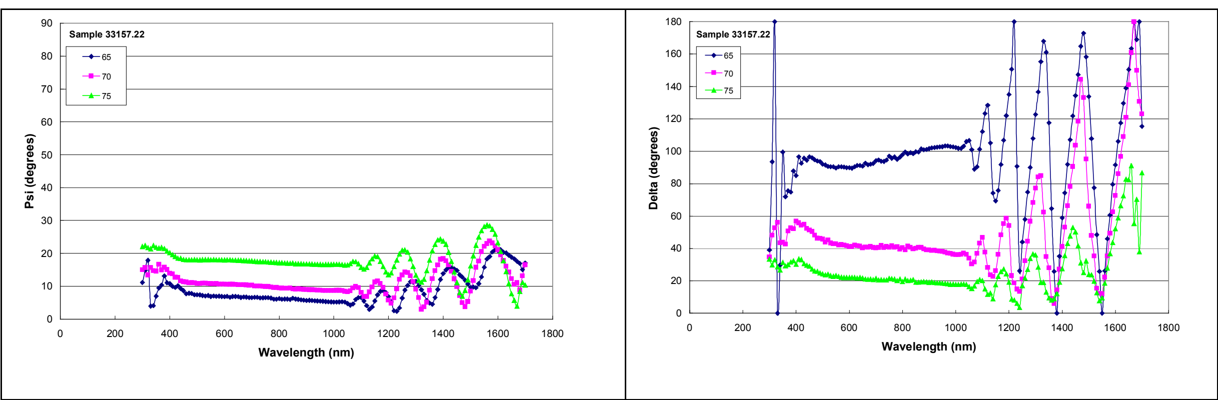

Figure 9.7. Measured spectroscopic ellipsometry parameters Psi and Delta from baseline CIGS sample 33157.22 for incident angles 65, 70, and 75 degrees.

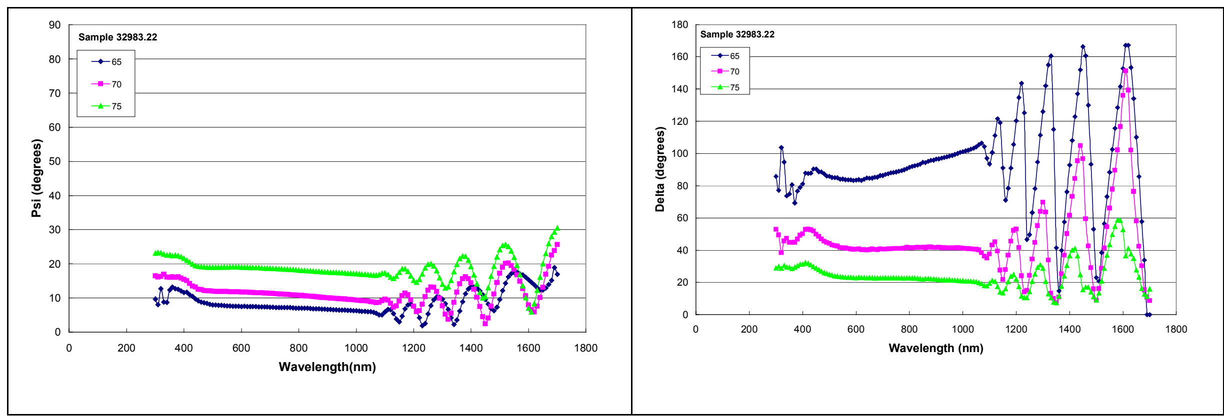

Figure 9.8. Measured spectroscopic ellipsometry parameters Psi and Delta from baseline CIGS sample 32983.22 for incident angles 65, 70, and 75 degrees.

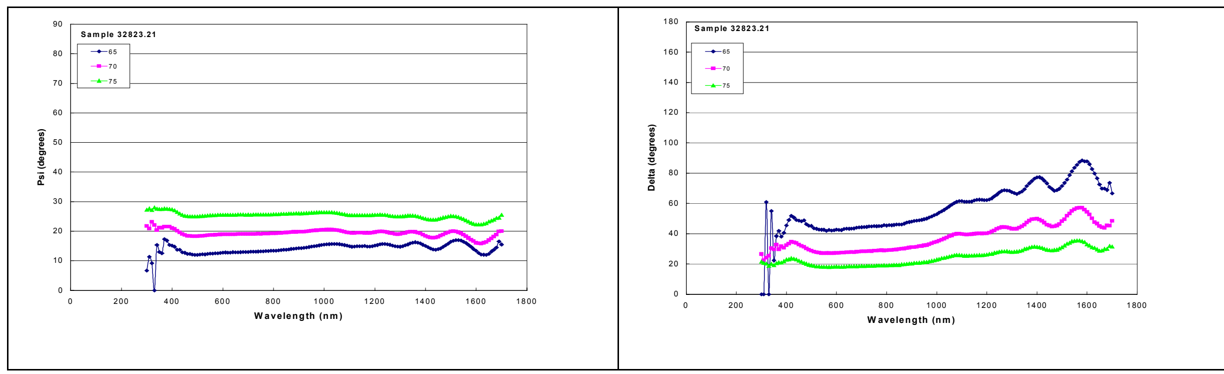

Figure 9.9. Measured spectroscopic ellipsometry parameters Psi and Delta from baseline CIGS sample 32823.21 for incident angles 65, 70, and 75 degrees (higher Cu).

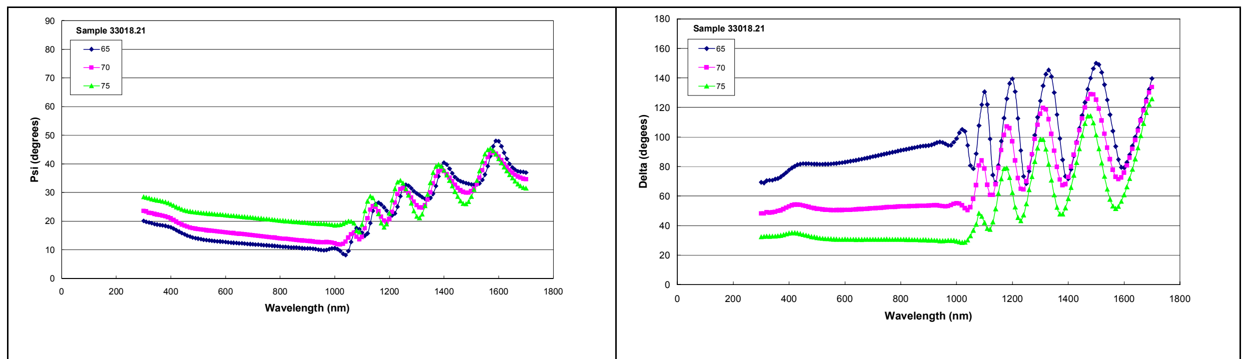

Figure 9.10. Measured spectroscopic ellipsometry parameters Psi and Delta from CIGS sample 33018.21 for incident angles 65, 70, and 75 degrees (Lower Cu).

9.7.2.2 Analysis of Spectroscopic Ellipsometry Data from CIGS Samples

Initial modeling of the measured data has proved to be very challenging due to the substantial differences in optical properties between the different samples including samples with the same compositions and produced with similar processing conditions. Our initial modeling efforts and results are reported below, however, additional structural and characterization information may lead to enhanced modeling that will provide additional insight into these samples.

In general, spectroscopic ellipsometry data analysis of materials like CIGS is enhanced with additional information about the samples, especially when very little SE data is available. Thus with the limited amount of information initially given for these samples, the present data analysis is tenuous and can be improved. Furthermore, CIGS is not a good optical material since its optical properties change significantly with small changes in composition (and possibly binary phase content) and processing conditions and since it has high surface roughness with substantial grain boundary and defect structures. Therefore, we could not use "literature" optical property values to begin the analysis of the samples and had to determine both the structural and optical properties simultaneously in the models.

Transparent Region

Our initial modeling effort focused on the transparent region of the SE data, from ~1100 nm to 1600 nm. The strategy we employed for SE data analysis of CIGS samples was to determine the physical properties of an individual CIGS film with the transparent region of the SE data, then use these physical properties in a self-consistent manner to analyze the bandgap region and the absorptive region of the SE data. Therefore, it is extremely important to develop accurate models for the transparent region before analyzing the other regions. The initial modeling results are only for the transparent regions of samples in which reasonable fits could be obtained.

Initial inspection of the SE data from the three baseline samples indicated that baseline sample 32876.22 (Figure 9.6), with its noticeably sharper and higher valued features in the transparent region, has significantly different optical properties compared to "baseline" samples 33157.22 (Figure 9.7) and 32983.22 (Figure 9.8), even though all three samples have similar compositions and were processed under similar conditions. The initial model for sample 32876.22 included a Mo substrate, a CIGS layer, and an interface (psuedo-surface roughness) layer between the surface of the CIGS and the air. The model used the CIGS thickness provided by IEC and optical

properties derived from other CIGS samples to start. However, both the optical properties (*n* and *k*), the CIGS layer thickness, and the surface roughness thickness were allowed to vary as the modeling performed the regression fitting routine for the data. Once complete, the model that best fit the data had the values shown in Table 9.2 and the *n* and *k* values shown in Figure 9.11. The regression models fit all the data taken at three different incident angles simultaneously to improve the fits. The models provide physically reasonable values for the optical properties ($n \sim 2.05$ and $k \sim 0.03$), CIGS film thickness (~2.9 µm), and surface roughness (~81 nm) with a reasonable fitting RMSE coefficient of 62 for sample 32876.22.

Two main points should be noted from this initial set of modeling data. The first is that any SE analysis for pseudo-surface roughness over ~10 nm does not correlate well to actual surface roughness values measured by atomic force microscopy or equivalent techniques. However, the SE measured surface roughness can be compared with other SE measurements of similar materials to provide an empirical relation between samples. Second, the *n* values for these CIGS samples is significantly lower than the ~2.8 expected from literature references. We will discuss optical properties of all the analyzed samples later and will discuss this low *n* value at that time.

Table 9.2. Measured composition and thickness of CIGS Films. The SE information was determined from analysis of the data.

Sample #[1]	Cu (%)	IN (%)	Ga (%)	Se (%)	Thickness SE (nm)	SE Surface Rough. (nm)	SE RMSE	Tss (C)	Thickness[2] (microns)	Comment
32876.22	23.0	19.2	7.7	50.2	2898	81	62	550	3.1	Baseline
33157.22	22.5	17.2	8.2	52.1	2826	43	39	550	2.8	Baseline
32983.22	24.4	17.7	8.5	49.5	2759	34	30	550	2.8	Baseline
33021.21	26.6	17.6	6.3	49.5	3025	63	45	550	3.1	Higher Cu
32823.21	30.9	16.9	5.1	47.2				550	2.5	Higher Cu
33018.21	19.9	19.8	7.7	52.6				550	2.9	Lower Cu
32897.21	16.8	21.6	9.7	51.9	3112	111	58	550	2.7	Lower Cu
32988.33	22.6	14.6	12.4	50.4	3177	142	29	550	3.2	Higher Ga
32991.33	21.5	10.6	16.5	51.4	2831	151	18	550	3.1	Higher Ga
32893.33	22.8	17.6	7.7	51.9	1377	54	90	550	1.5	½ thick.
32889.21	26.7	16.3	8.0	49.1	1118	78	41	550	1.4	½ thick., high Cu
32909.22	24.0	19.2	9.0	47.9	3052	209	53	400	2.9	Low T (small grain)
33125.21	25.9	16.2	7.3	50.6	3284	154	26	400	3.0	Low T, high Cu

1. Samples, EDS compositional information, and processing condition provided by IEC.
2. Thickness measured by mass gain after deposition of CIGS.

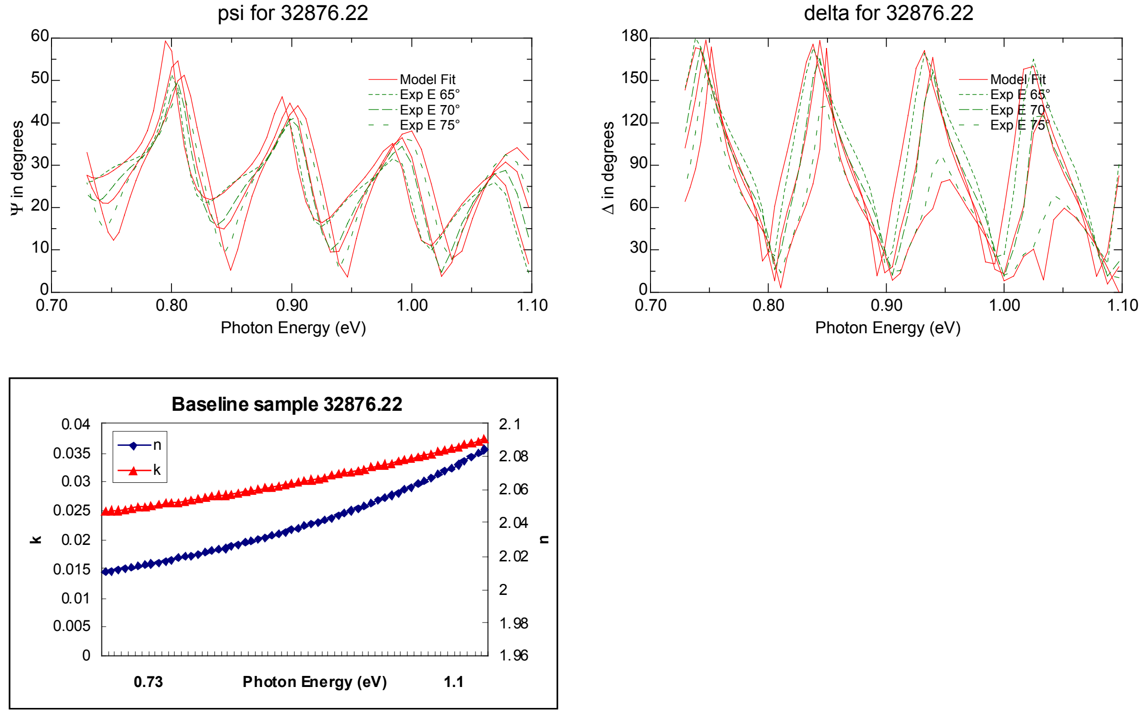

Figure 9.11. Baseline sample 32876.22 modeled with thickness and cauchy coefficients for *n* & *k*

The optical properties for sample 32876.22 could not be used to model the other "baseline" samples (Figure 9.12). A single set of optical properties were determined and used to model the baseline samples 33157.22 and 32983.22 but different *n* and *k* values from sample 32876.22 were required to provide a reasonable fit (Figure 9.12). Again the physical and optical properties used to model the SE data of these two baseline samples is shown in Table 9.2 and Figure 9.12. While there are slight differences in composition and film thickness, there is a significant difference between the *n* and *k* values for sample 32876.22 and samples 33157.22 or 32983.22. This difference in optical properties between the baseline samples indicates that sample 32876.22 will probably have significantly different optical properties for solar collection compared to "baseline" samples 33157.22 or 32983.22. Furthermore, the higher *k* values for sample 33157.22 and 32983.22 compared to sample 32876.22 in the transparent region indicates that structures in the CIGS layer are causing additional absorption or scattering of light. The differences in the baseline samples could not be accounted for by including "voids" in the CIGS layer to account for grain boundaries and specific inhomogeneous phases.

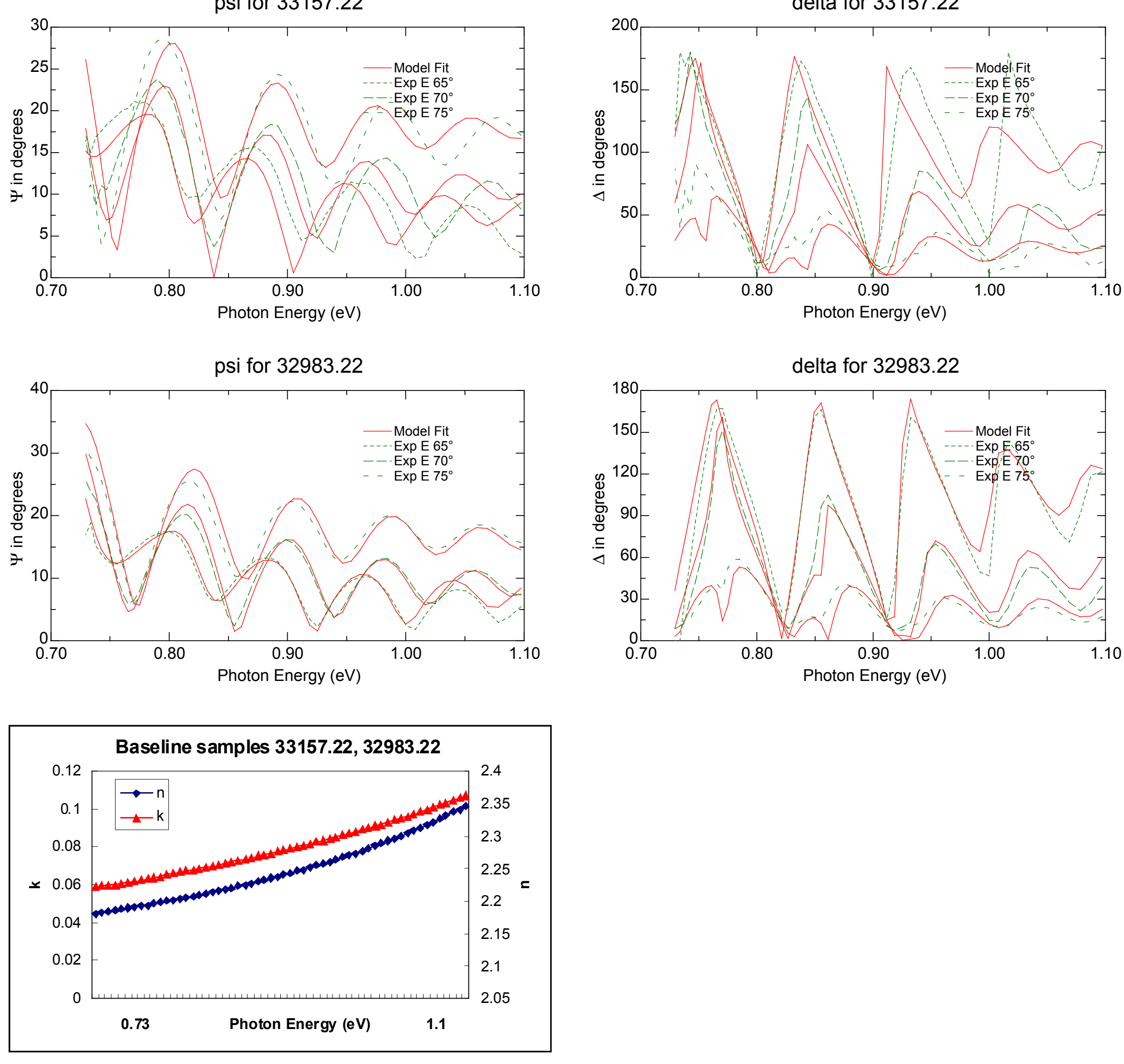

Figure 9.12. Baseline samples 33157.22 and 32983.22 modeled with thickness and cauchy coefficients for *n* and *k* coupled together for each model

Typically, for a given set of "baseline" samples we want to establish and fix the optical properties (*n* and *k*) and then develop models that establish the physical properties. We were able to do this with baseline samples 33157.22 and 32983.22 but not sample 32983.22 which should have better solar collection properties. However, initial inspection of the SE data also indicated that sample 32893.33 (Figure 9.13) should also have good solar collection properties and we were able to model the SE data using the optical properties derived from sample 32876.22. Sample 32893.33 has approximately half the CIGS film thickness compared to the baselines with a correspondingly smaller surface roughness (Table 9.2). Thus we were able to use our preferred SE analysis strategy with sample 32893.33 even though the CIGS thickness was substantially reduced.

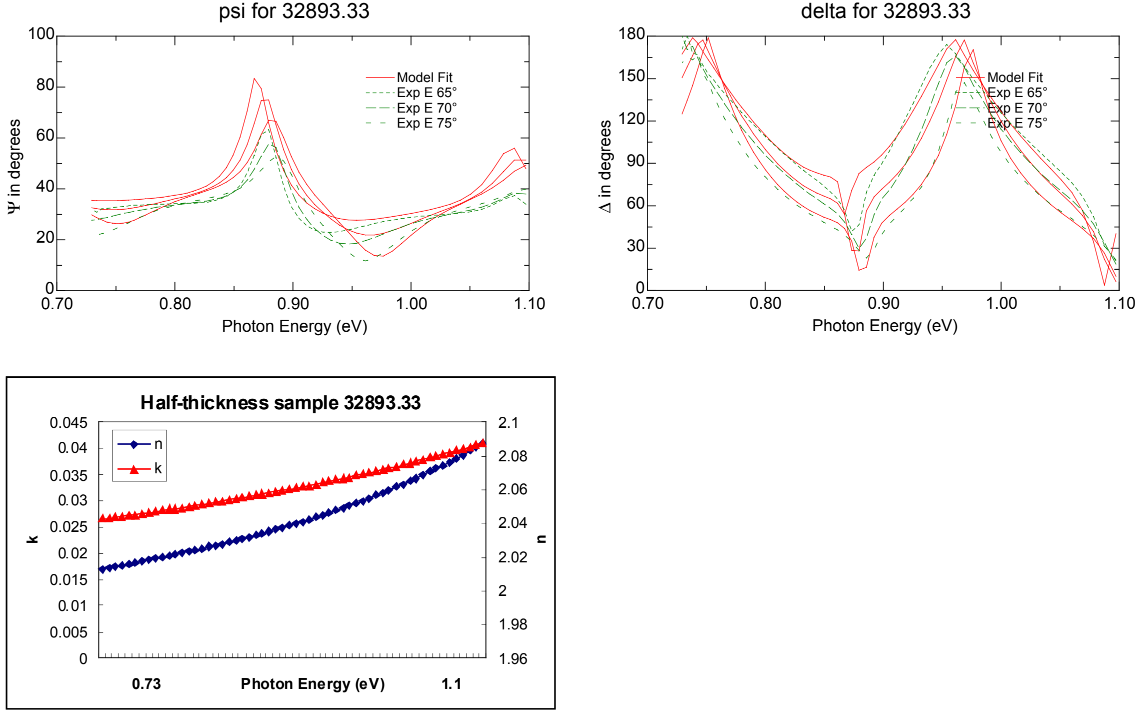

Figure 9.13. Half thickness sample 32893.33 modeled with thickness and optical parameters from sample 32876.22.

Since increasing and decreasing the Cu content of the CIGS films significantly changes both the physical and optical properties, analysis of the SE data has not been forthcoming for two of the samples, 32823.21 and 33018.21, and very tenuous for the other two, samples 33021.21 and 32897.21. However, since, to first order, Ga simply replaces In in the CIGS films and since CIS and CGS have similar optical properties in the transparent region, we felt that some useful information could be obtained from the high Ga samples and the low T sample with similar composition to the baselines. Initial inspection of the Ga SE data indicated that the spectra were more similar to baseline samples 33157.22 and 32983.22. However, initial attempts to model higher Ga sample 32988.33 with the optical properties from samples 33157.22 and 32983.22 were unsuccessful (see Figure 9.14). As shown in Figure 9.14, by letting n vary, a reasonable fit was achieved with a relatively low RMSE, a CIGS film thickness virtually identical to the expected thickness, but a relatively rough surface. The need to change n from the baselines to account for the difference in optical properties is not surprising, but emphasizes the difficulty of analyzing the SE data due to its intrinsic sensitivity to optical and physical properties of the CIGS films. The higher Ga sample 32991.33 could only be modeled by letting the film thickness and optical properties vary during the regression fit (Figure 9.15).

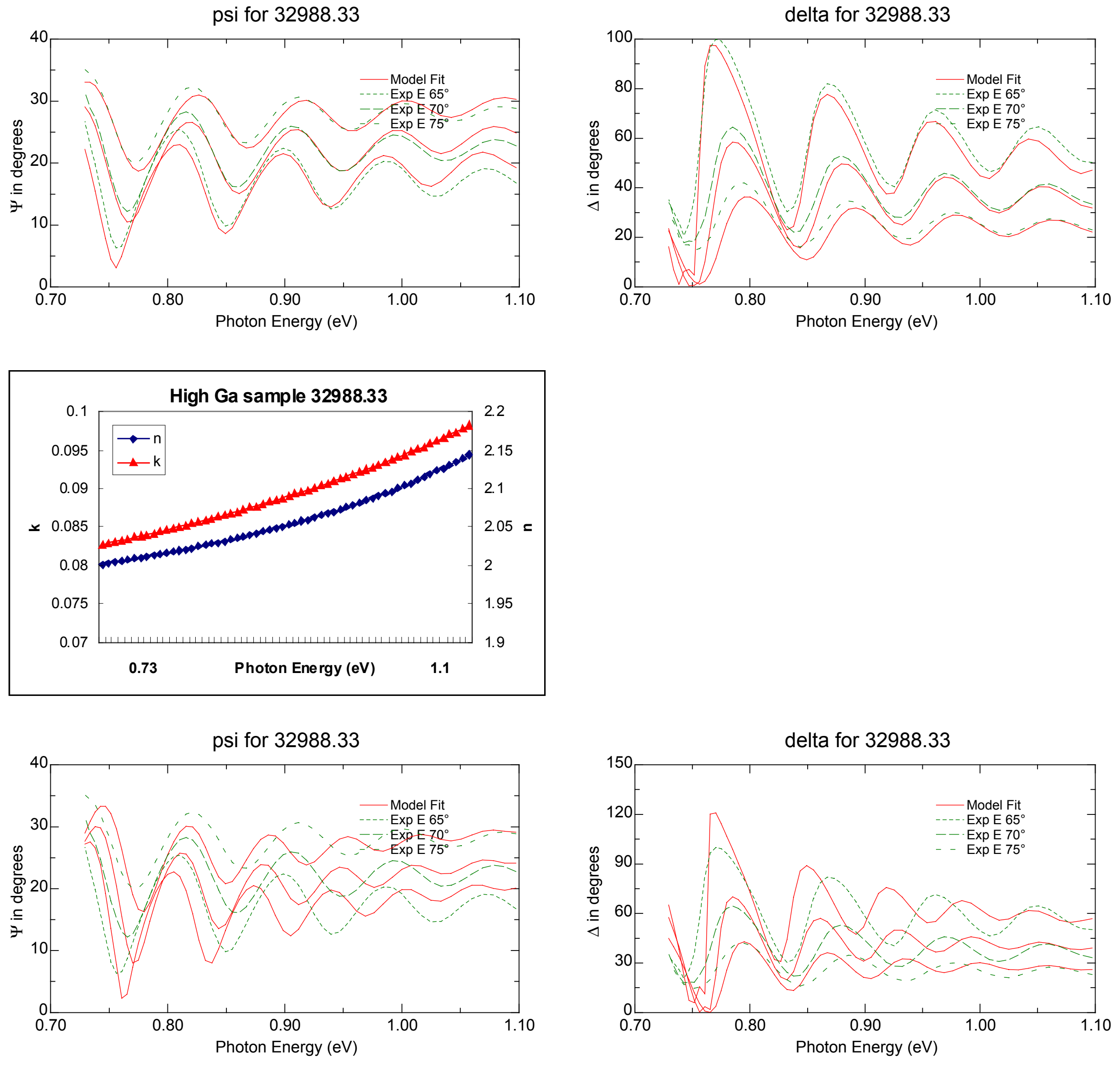

Figure 9.14. High Ga sample 32988.33 modeled with thickness and cauchy parameters for *n* and *k* (more dependant on *n*) and modeled with (lower two plots) thickness and optical properties coupled to baseline samples 33157.22 and 32983.22 (See Figure 2).

The higher Cu content in sample 33021.21 significantly increased k (Figure 9.16) and thus the absorption in the transparent region. Using the optical properties from sample 33021.21, we were able to obtain a reasonable fit for sample 32889.21 (Figure 9.17) which had a similar Cu content but approximately half the CIGS film thickness. As with the two baseline samples 33157.22 and 32983.22, and samples 32876.22 and 32893.33, the ability to use optical properties of one sample to determine the physical properties of another indicates that we will be able to develop a data base of CIGS optical properties that can be used to identify appropriate compositions and performance criteria that can be used for process control. The main issue will be developing a large enough data base with known optical and physical properties to provide appropriate characterization of the CIGS deposited films over a diverse processing space.

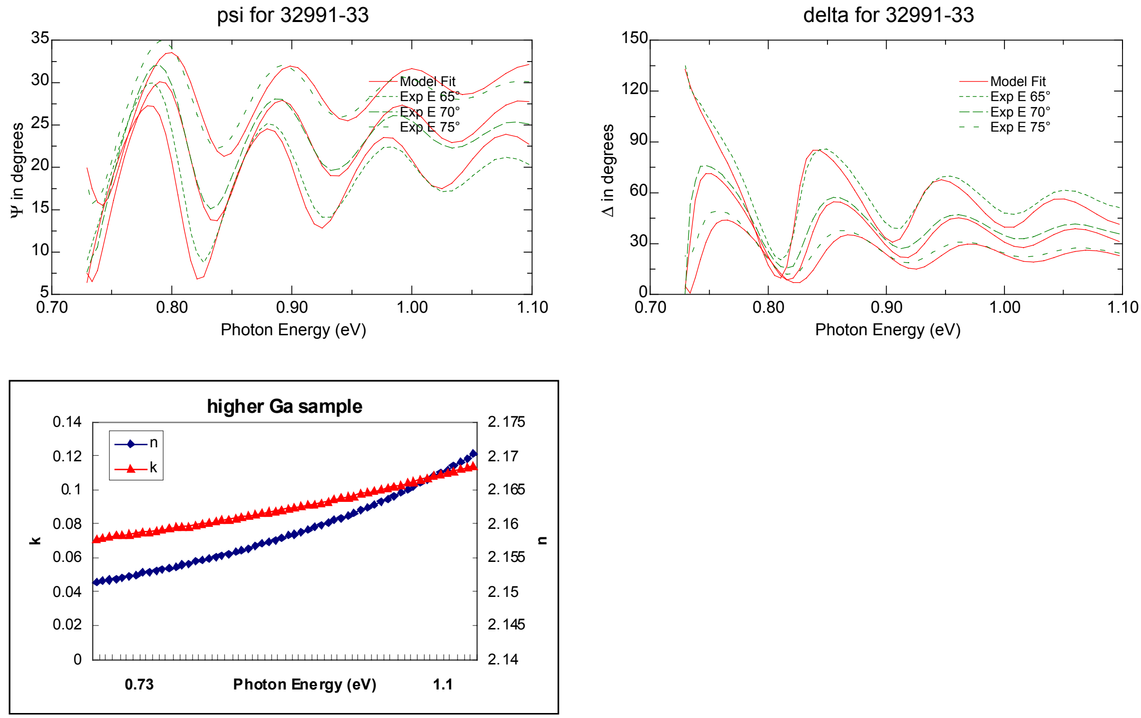

Figure 9.15. High Ga sample 32991.33 modeled with thickness and cauchy coefficients for *n* and *k.*

Modeling the low Cu sample 32897.21 required substantial changes in the optical properties with a significant increase in *n* and *k* at the lower wavelengths (Figure 9.18). The other significantly different samples (32909.22 and 33125.21) involved CIGS deposition at lower substrate temperatures. Attempts were made to include "voids," presumably accounting for grain boundaries, in the CIGS layer for all of the other samples analyzed. The modeling indicated that these "voids" or grain boundaries did not significantly alter the optical properties for the other samples. However, by including these grain boundary effects in the models for the lower temperate samples, a significant "void" percentage was needed to accurately fit the data. For sample 32909.22 a reasonable fit was achieved by using the optical parameters from baseline sample 33157.22 and including 18.3% voids in the CIGS layer (Figure 9.19). A better fit was obtained by allowing the *n* and *k* values to vary significantly, resulting in less voids (10.5%) in the CIGS layer but a thicker film at 3457 nm. Without an accurate independent measure of grain size, it is impossible to determine which model is appropriate.

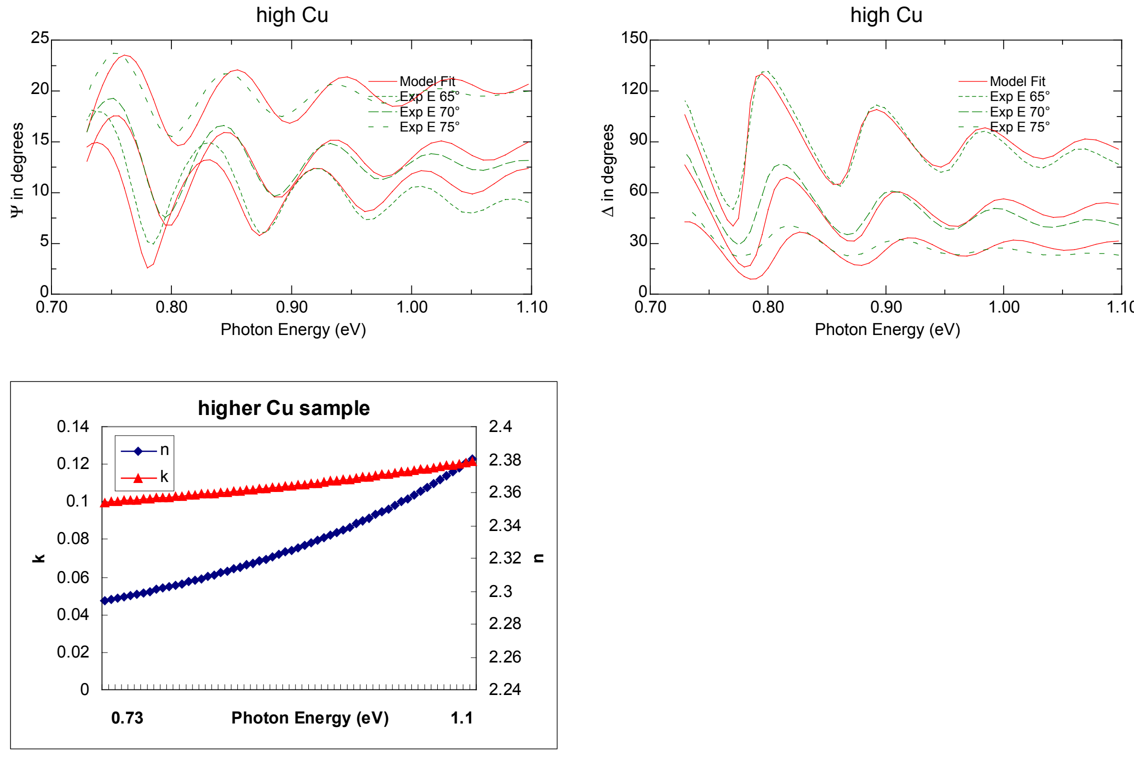

Figure 9.16. High Cu content sample 33021.21 modeled with thickness and cauchy coefficients for *n* and *k*.

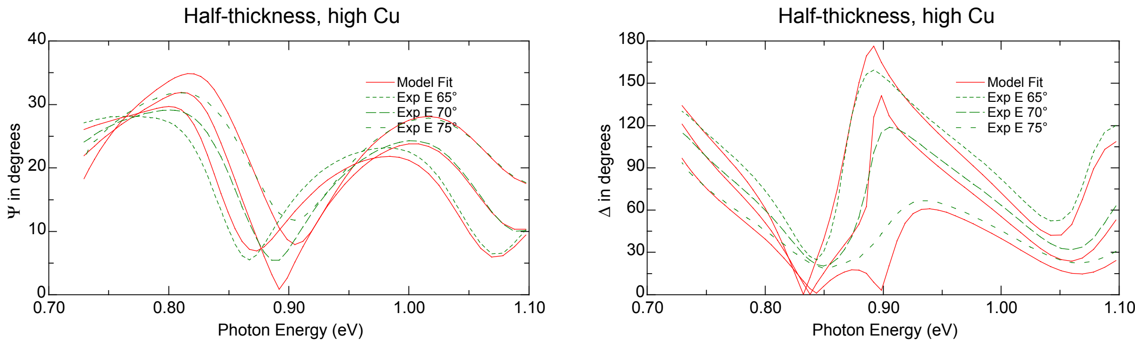

Figure 9.17. High Cu content, half thickness sample 32889.21 modeled with thickness and optical parameters from sample 33021.21.

A similar approach was used for the low temperature sample 33125.21 (Figure 9.20) where the models used the optical properties from sample 33021.21 and/or allowed *n* and *k* to vary. The model coupled to the optical parameters from sample 33021.21 required 17.7% voids, while the cauchy parameter model required 25% voids. It is evident from these lower temperature samples, that decreased grain size is an important factor that must be included in the models to accurately account for the SE data. However, along with characterization information about grain size and

voids in the CIGS layer, additional information will be needed to account for the substantial differences in the optical properties between baseline and other similar samples. Furthermore, additional information will be needed to account for the substantial decrease in *n* (~2 to 2.4) for all the samples (Figure 9.21) compared to the 2.8 expected from the literature. This may be related to the fact that the CIGS films used for photovoltaics are not stoichiometric and therefore have significantly different compositions compared to crystalline samples used in the literature references. Also, specific phase formation, incorrect Mo optical properties, inhomogeneities, and other defects may account for some of the discrepancy in *n*.

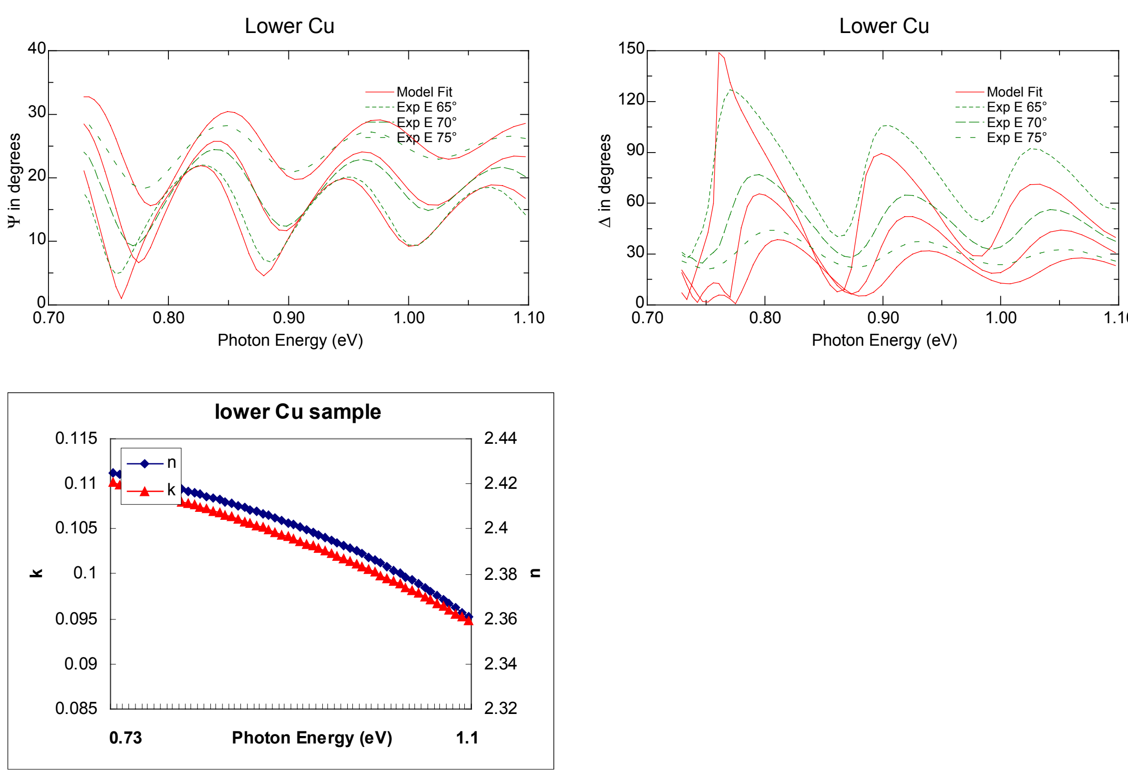

Figure 9.18. Low Cu content sample 32897.21 modeled with thickness and cauchy coefficients for *n* and *k*.

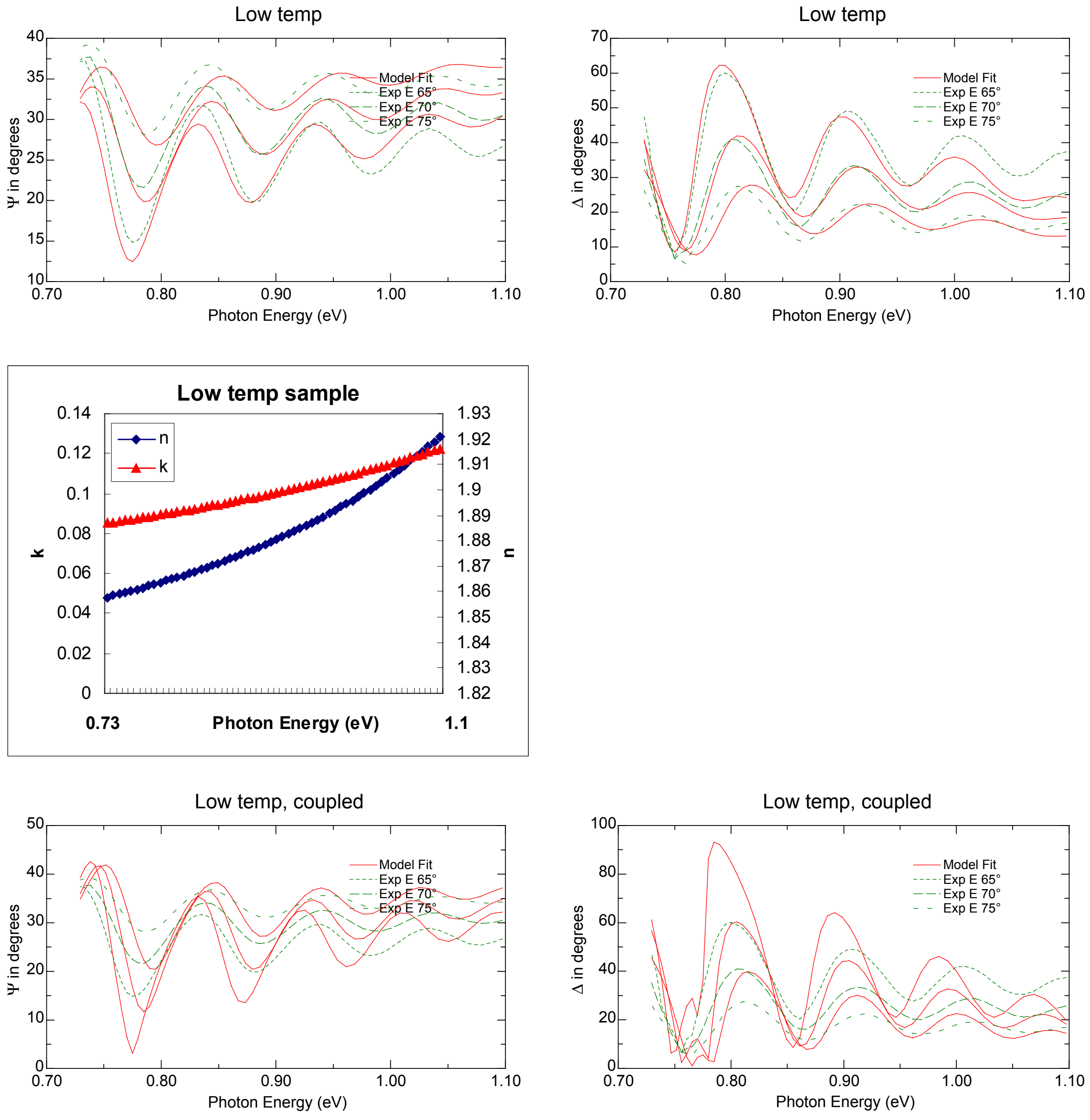

Figure 9.19. Low temperature sample 32909.22 modeled with thickness and cauchy coefficients for *n* and *k*, or with thickness and coupled optical properties from sample 32876.22 (lower two plots).

Low temp, high Cu

Model Fit
Exp E 65°
Exp E 70°
Exp E 75°

Ψ in degrees
Photon Energy (eV)

Low temp, high Cu

Model Fit
Exp E 65°
Exp E 70°
Exp E 75°

Δ in degrees
Photon Energy (eV)

Low temp, high Cu sample

n
k

k
n
Photon Energy (eV)

Low temp, high Cu, coupled

Model Fit
Exp E 65°
Exp E 70°
Exp E 75°

Ψ in degrees
Photon Energy (eV)

Low temp, high Cu, coupled

Model Fit
Exp E 65°
Exp E 70°
Exp E 75°

Δ in degrees
Photon Energy (eV)

Figure 9.20. Low temperature sample 33125.21 modeled with thickness and cauchy coefficients for *n* and *k*, or with thickness and coupled optical properties from sample 33021.21 (lower two plots).

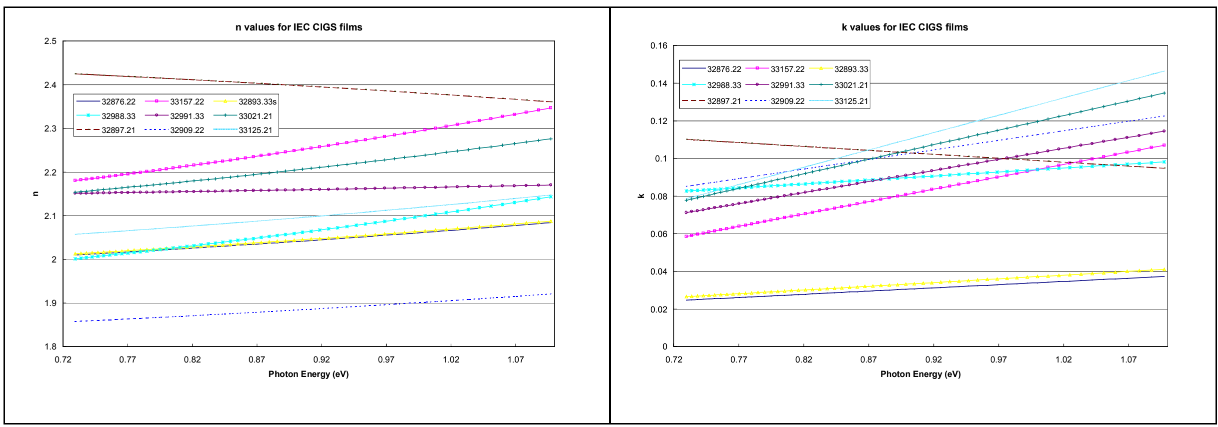

Figure 9.21. Comparison of *n* and *k* values for different CIGS samples.

Spectroscopic Ellipsometry Analysis of the Absorption and Band Gap Region

Spectroscopic ellipsometry modeling for the absorption and bandgap regions of the 13 CIGS samples provided by IEC has been initiated. Initial analysis of the SE data for baseline sample 32876.22 (Figure 9.22) indicates that this method provides a self consistent way to determine the optical properties of the CIGS films in the absorption region between ~ 250 and 900 nm. The model and fits for this specific data set are very good. We will apply this approach to the other samples to derive their specific optical properties in the absorption region. It should be noted that the inherent surface roughness of the CIGS samples produces depolarization of the light that is not accurately accounted for by the rotating analyzer spectroscopic ellipsometer used to collect these data. As a result, the imaginary part of epsilon data has angle of incident dependence in the absorption region. While this posses a potential problem for extremely accurate modeling of these samples, it may not be a problem for the more empirical data needed for process control. Furthermore, it does provide a possible measure of surface roughness and the PDSE may be able to measure these effects directly providing a superior analysis of the CIGS samples.

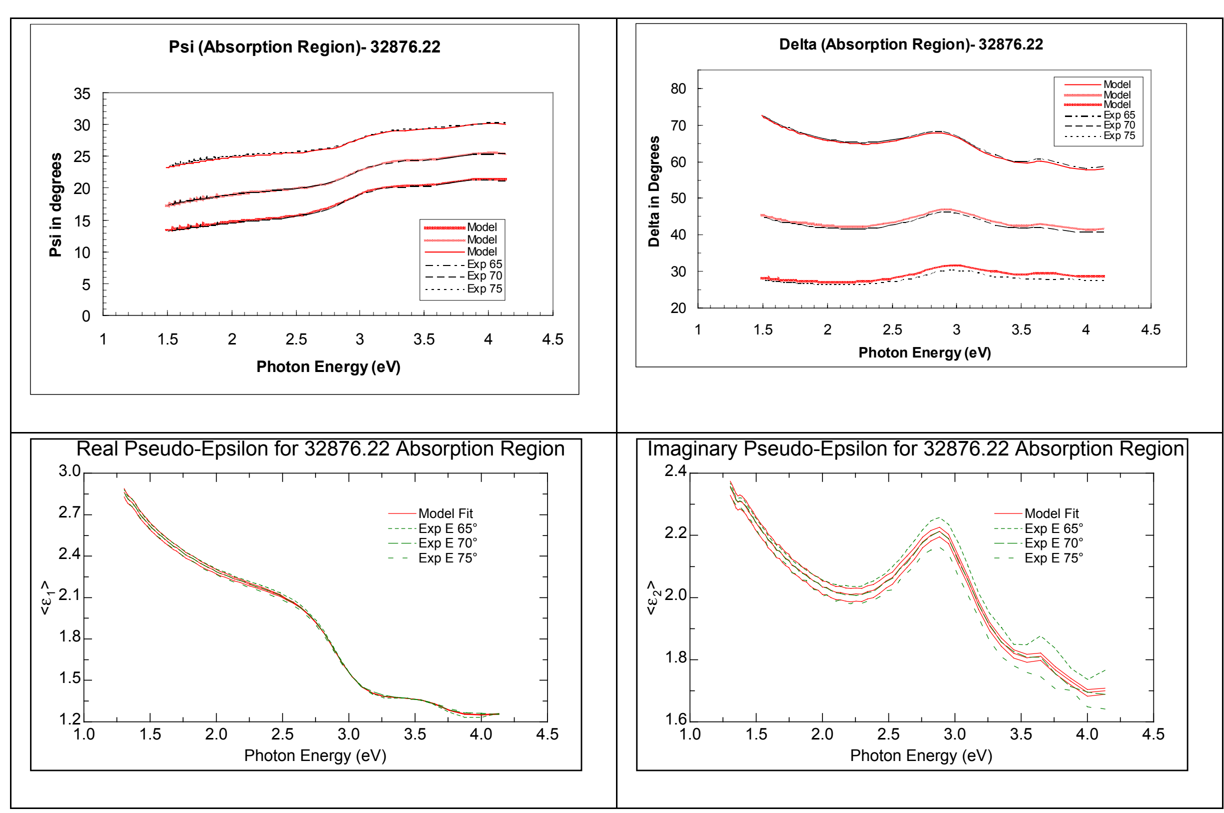

Figure 9.22. Plots of the modeled SE data from sample 32876.22 for the absorption region. The models used the exact material structure established with the transparent region data to fit the absorption region data.

Modeling of the band gap region has also been initiated for all the samples. This modeling involved using the individual structure models developed with the transparent region data to

back out the optical properties in the band gap region. Figure 9.23 contains plots of the ellipsometric parameters Psi, Delta and the pseudo-dielectric with their corresponding fits based on the models developed for the transparent region. Again this approach was fairly straight forward, however exact determination of the band gap has proven to be very challenging. In general, band gap determination should be based on fitting the data to a first principles model that explicitly contains the band gap as one of the parameters. Initial attempts using this strategy have been met with only limited success. While we will continue to develop this strategy to exactly determine the band gap, for process control we also want to investigate other strategies that can provide the band gap very quickly.

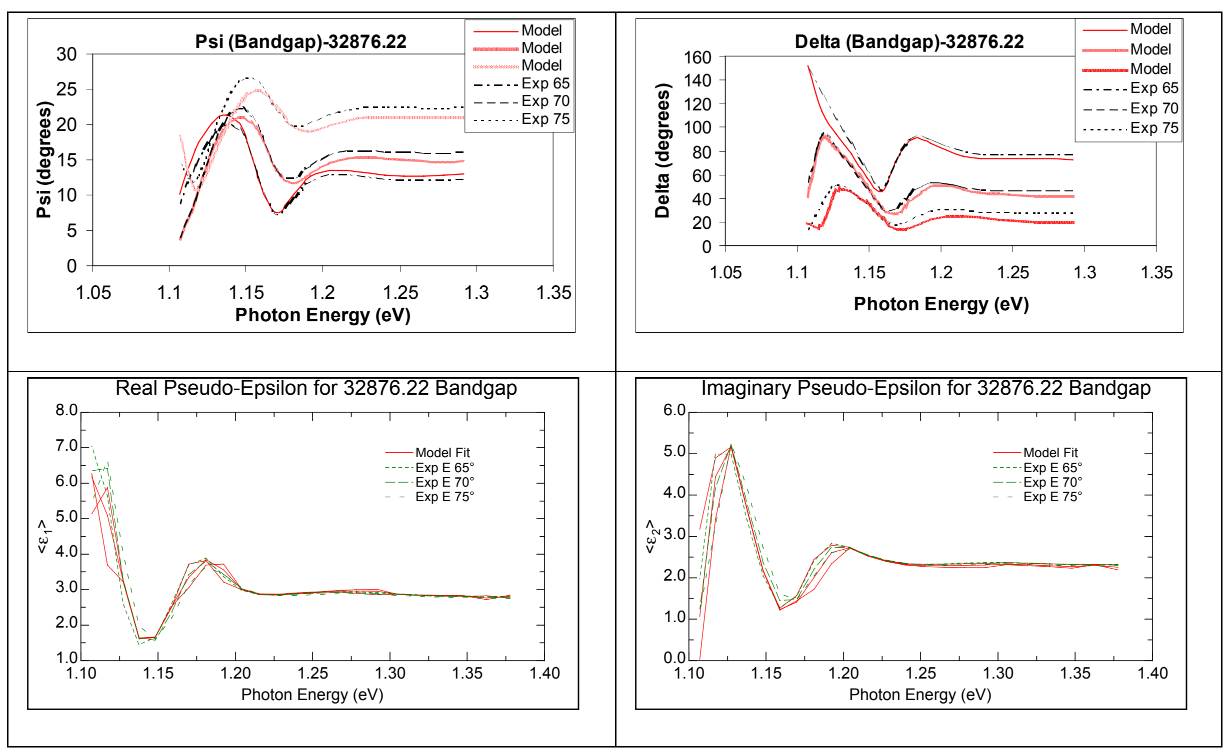

Figure 9.23. Plots of the modeled SE data from sample 32876.22 for the band gap region. The models used the exact material structure established with the transparent region data to fit the band gap region data.

Since CIGS is strongly absorptive for light energies above the band gap, an initial examination of the data was performed based on quantitatively identifying the energy where the oscillation due to interference effects in the transparent region ends. Specifically, by monitoring the imaginary part of the pseudo-dielectric or the dielectric function which are linearly related to the absorption coefficient, it was possible to identify criteria based on inflection points where the absorption of the CIGS samples change significantly at the band gap. Thus by taking the second derivative of the imaginary part of the pseudo-dielectric and dielectric functions (Figure 9.24) the inflection points are unambiguously identified when the second derivative crosses zero.

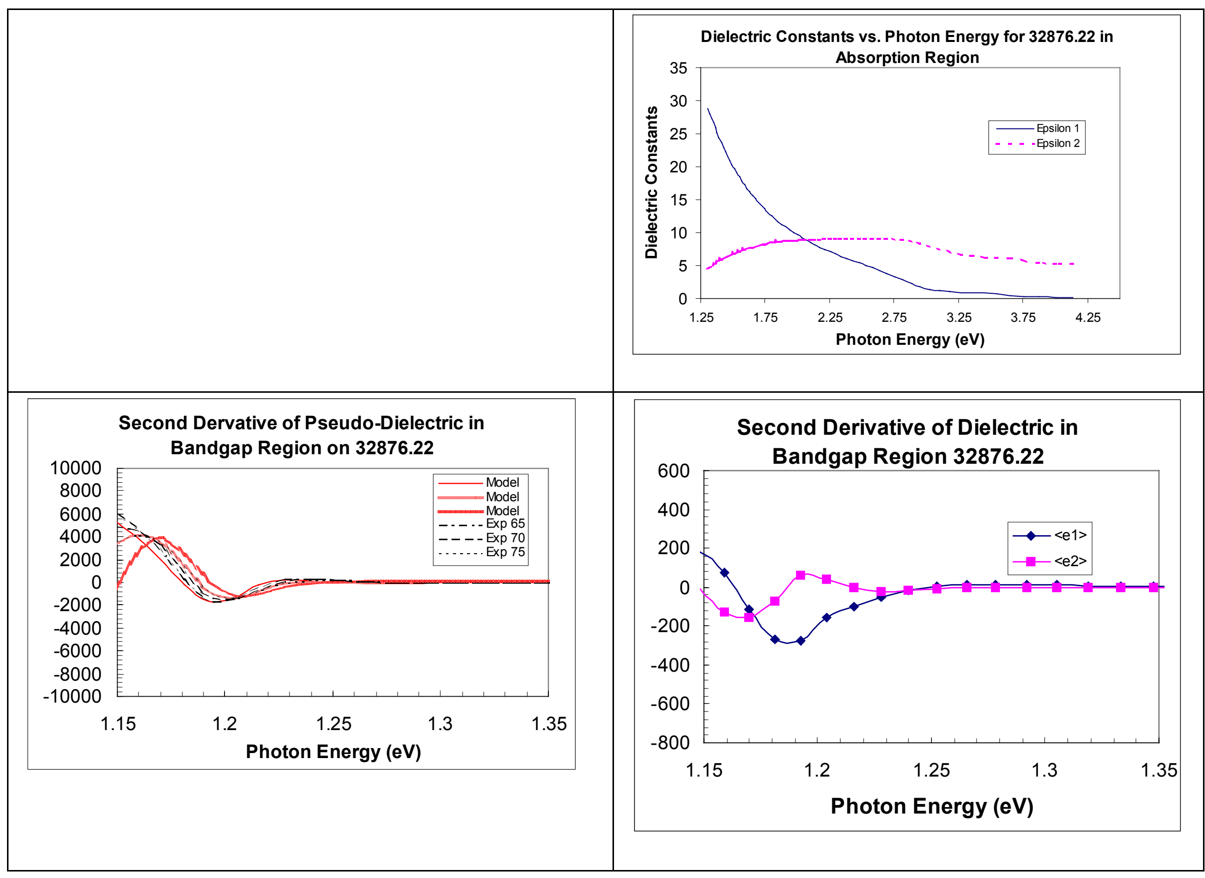

Figure 9.24. Second derivative plots of the imaginary part of the pseudo-dielectric and dielectric functions in the band gap region. The inflection points correspond to the points in the second derivatives that are zero.

9.7.2.3 Potential Real-Time Data Interpretation Concepts

As mentioned above, we have a strategy to determine the surface roughness of CIGS films using visible light. In addition, we will also develop interpretive algorithms that can quickly determine the bandgap and quality factor of CIGS films. CSM has demonstrated that the quality factor is directly related to film performance and efficiency while the band gap should be intricately tied to composition. Our initial strategy will be to incorporate one or two of these measured ellipsometric parameters into a process control structure. Additional measured CIGS film properties will be investigated and may be incorporated in the process control structure as needed.

As an example, we used the second derivative criteria to provide an estimate of the band gap for all the samples. Figure 9.25 contains a plot that includes the band gap estimates based on the pseudo-dielectric, dielectric, and literature model data as a function of gallium fraction. It appears from this initial data set that both the pseudo-dielectric and dielectric functions provide similar information based on the second derivative technique. This means that the imaginary part of the pseudo-dielectric which can be determined without any regression modeling can be used to provide real-time information that can be related to the band gap. While the band gap

estimates are not exactly what is expected based on literature values for the gallium fraction in the CIGS samples, except for a couple of samples, the trend is very similar. Additional measurements and work need to be performed to either calibrate the second derivative derived bandgap estimates to the literature values or to define a more appropriate criteria for estimating the bandgap. Either way, better modeling and determination of the band gap based on first principle models will be performed to provide more accurate band gap estimates.

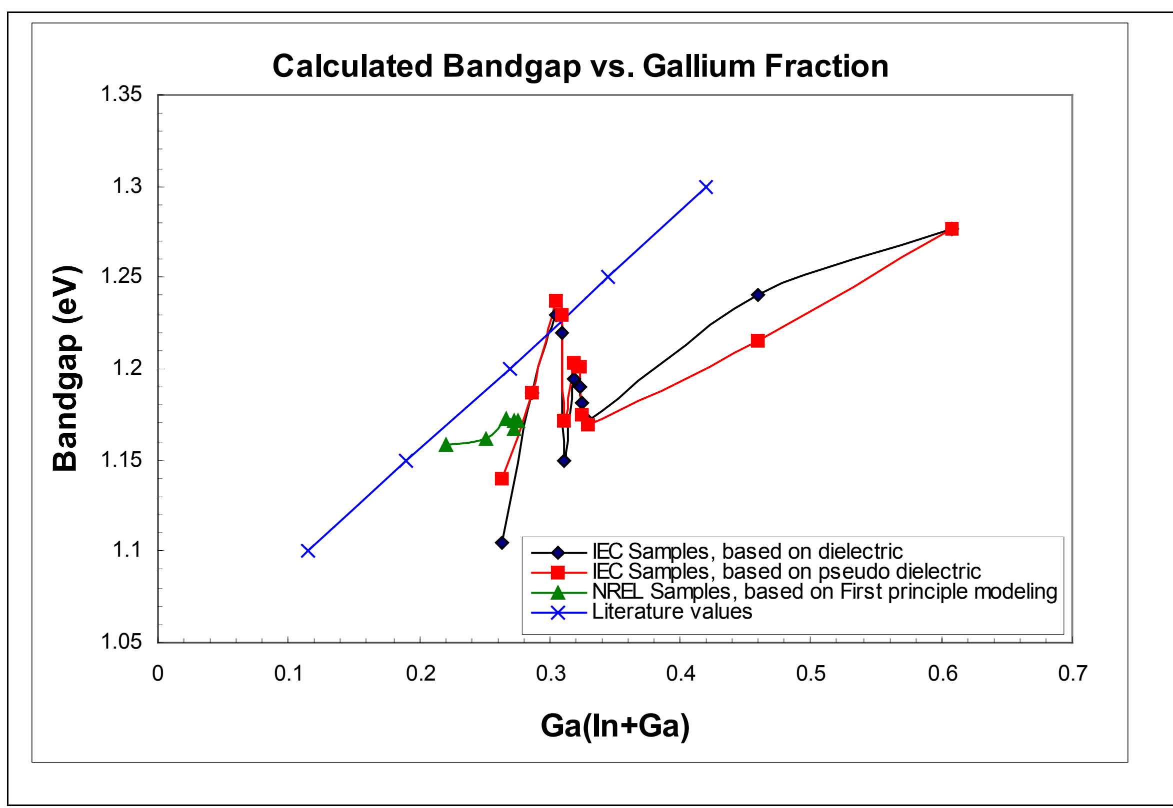

Figure 9.25. Comparison of bandgaps as a function of Ga(In+Ga) ratio for CIGS samples.

9.8 Conclusion and Future Work

While the PDSE effort is very complex and requires a tremendous amount of effort to complete, the PDSE can provide the type of process control information that may be needed to make high conversion efficiency CIGS films at the production scale. The final calibration results with Si samples indicates that the PDSE can provide absolute ellipsometry/polarimetry measurements with the accuracy of top quality standard rotating polarizer spectroscopic ellipsometers in a fraction of the time with perhaps higher precision and signal to noise. Optimizing the PDSE for thin metal films should provide comparable results to the Si data reported in Figure 9.3, however, at this time to accelerate our PDSE process control efforts we have begun optimizing the PDSE for CIGS samples. Additional work to streamline and enhance the software for the PDSE will continue along with the development of the IR collection capabilities.

With the completion of the design, once the PDSE hardware is physically constructed and mounted in the production CIGS deposition chamber at GSE we will begin recording data and testing the measurement capabilities of the instrument under actual production conditions Once appropriate data is being measured in the CIGS production system, the data will be analyzed and the interpretive algorithms modified if necessary. The interpretive algorithms will then provide information that can be integrated into a process control structure.

Our initial modeling effort focused on the transparent region of the SE data, from ~1100 nm to 1600 nm. Substantial differences in optical properties between the different samples including samples with the same compositions and produced with similar processing conditions was observed. Therefore, "literature" optical property values could not be used and models had to be constructed to account for both the structural and optical properties of the samples. The strategy for SE data analysis of CIGS samples is to determine the physical properties of an individual CIGS film with the transparent region of the SE data, then use these physical properties in a self-consistent manner to analyze the band gap region and the absorptive region of the SE data. We will continue our modeling of the other samples in the absorption and band gap region and perform first principle modeling of the band gap region to determine the band gap of the different samples.

10. Alternative Contacts

10.1 Back Contact

10.1.1 Introduction

Molybdenum (Mo) has been used almost exclusively as a back contact material for CIGS-based photovoltaics. Key beneficial features of Mo include: high electrical conductivity, ohmic contact to CIGS, and high temperature stability in the presence of selenium during CIGS absorber deposition. Nevertheless, GSE has identified a few issues regarding Mo. Mo is an expensive brittle material that exhibits large intrinsic stresses when deposited by sputtering. The compressive stress in the Mo complicates substrate handling and transport, as it has a tendency to curl or roll up even when constrained under tension between rollers. Intrinsic film stresses can be controlled by choice of sputter deposition working gas pressure, however, Mo deposited at higher pressures exhibited other problems.

Additionally, sputtered Mo does not adhere well to the stainless steel chamber walls resulting in excessive Mo debris generation. As a result, Mo production chambers require frequent cleaning to remove debris.

Problems with Mo as the back contact material also extend to glass substrates. When deposited at low sputter working gas pressures (achieving dense, near bulk electrical resistivity), adhesion to glass is poor, whereas at high sputter pressures adhesion is good but at the expense of increased resistivity. High pressure/low pressure bi-layer Mo is often used but transition to in-line automated manufacturing will require two chambers to deposit the back contact layer, thereby increasing cost.

Goals for GSE entail large-scale production of thin film CIGS for all market segments: utility, consumer, and space. In meeting these markets, the cost of every manufacturing operation in the production of CIGS modules must be considered. Deposition of Mo as the back contact is currently a significant issue with regard to meeting our ultimate cost goal. Mo as the back contact impacts cost by: the cost of raw materials, delivery time (cost of working capital), down time for chamber cleaning, and reduced yield from Mo particulate on the substrate caused by poor adhesion of the Mo to the stainless steel vacuum chamber walls.

10.1.2 Back Contact Task Objectives

GSE is investigating alternative back contact materials that can be engineered to avoid the difficulties associated with Mo. Lower melting point materials should be less prone to stress retention. Candidate materials must also be low cost and must be tested for compatibility with CIGS device stack formation and module processing (in particular the material must form a ohmic contact with CIGS and be stable as not to diffuse into the CIGS or react with Se during deposition). Although Mo is not ideal, and based on its work function should not form an ohmic contact with CIGS, it is currently the best available and standard metal for industry and laboratories.

Under the PVMaT program, GSE is investigating alternative back contact materials. Results from this task should be applicable to other substrate including glass, polymer, and metal foil.

Quantitative benefits expected from the back contact task under the PVMaT program include:

- reduce cost of back contact deposition operation by 50%,
- reduce raw material cost by 50%,
- reduce scheduled and unscheduled downtime by 50% by reducing particulate contamination, and
- increase step yield to 99% by eliminating frequent arcs or shunts from Mo debris.

Cost modeling indicated that the above items correspond to a reduction in cost and an increase in capacity by achieving a reduction in direct materials cost, operating cost, and downtime while improving yield.

10.1.3 Back Contact Technical Approach

Technical approach for the alternative back contact task involved investigating different metals and alloys as well as bi-layers. Bi-layer configurations consisted of Mo in direct contact with CIGS and an underlying layer that provides the bulk of the back contact sheet resistance and controls the stress state.

Initial identification of potential contact candidate was based on a review of past literature and by discussions with organizations involved with CIGS development. With candidates identified, both single element and bi-layer materials were analyzed for potential reaction with selenium. Single element back contacts were deposited at IEC and sheet resistance and crystallography were characterized. CIGS was deposited on the most promising single component back contacts and finished into devices to measure the ohmic behavior of the interface.

In parallel, bi-layers were deposited in GSE roll-to-roll production-based equipment. Two promising bi-layers that consist of a conductive underlying layer and Mo as the overlying layer were deposited. Back contact uniformity was characterized by measuring across-web and down-web sheet resistance. CIGS was deposited on candidate bi-layers in GSE roll-to-roll production-based equipment and devices were characterized to assess behavior of the back contact.

10.1.4 Back Contact Results

10.1.4.1 Background and Candidate Material Identification

The back contact base layer in a CIGS module serves to collect photogenerated current. Desirable film characteristics and deposition properties for the back contact include:

- good bonding to the substrate,

- sheet resistance of less than 1 Ω/sq., analysis indicated less than a 1% power loss due to series resistance for a CIGS module with a cell spacing of 0.5 to 0.75 cm at AM 1.5,
- ohmic contact to CIGS,
- amenable with high rate deposition,
- low cost, readily available raw material,
- stable at CIGS processing temperatures of 450 to 600°C in selenizing environment, and
- neutral or slightly compressive stress.

Metal contacts with CIS were investigated by NREL in the early 1980s [Ref 5-1]. Candidate back contacts included platinum (Pt), gold (Au), silver (Ag), nickel (Ni), copper (Cu), aluminum (Al), and molybdenum (Mo). According to these early NREL studies (as summarized in Table 10.1), Au and Ni were the best and most reproducible contacts to CIS with clean interfaces and no evidence of reaction. Good ohmic contact was also achieved with Ag, but Ag had a tendency to diffuse in CIS and dope it n-type. Al was generally a good ohmic contact but was unstable due to natural oxide formation and could not withstand CIS processing temperatures. Mo was reported to exhibit a slight diode behavior but had a low contact resistance to CIS and was stable with no detectable reaction.

Despite the positive results with Au and Ni, both were eliminated as serious candidates for the back contact to CIS. Au is expensive and limits the ultimate PV cost whereas Ni was difficult to sputter at a high rate. As a result, Mo became the leading candidate for the back contact and is the material most widely used by researchers and industry. Key attributes of Mo include: low sheet resistance, low contact resistance, stability at CIS deposition temperatures, amenable to high rate deposition processes such as sputtering, reasonable cost compared to Pt, Au and Ag, and phase stability in contact with CIS, Cu, In, and Se.

Table 10.1 Ohmic behavior of CIS/metal contacts from NREL Work [Ref 5-1].

Metal	Configuration	Deposition Technique	Behavior	Reproducibility
Au	Substrate*	Thermal Heating	Ohmic	Very Good
	On CIS†	Thermal Heating	Ohmic	Very Good
Mo	Substrate*	d.c. Magnetron	Non-Ohmic	Good
	On CIS†	r.f. Magnetron	Generally Ohmic	Very Poor
		d.c. Magnetron	Generally Ohmic	Poor
Ni	On CIS†	d.c. Magnetron	Ohmic	Very Good
Al	On CIS†	Electron Beam	Generally Ohmic	Poor
		d.c. Magnetron	Ohmic	Good
Ag	On CIS†	Thermal Heating	Generally Ohmic	Poor
		d.c. Magnetron	Generally Ohmic	Poor
Cu	On CIS†	Electron Beam	Non-Ohmic	Poor (Degraded with time)

* CIS deposited onto metal, † Metal deposited onto CIS

Under the PVMaT program, GSE proposed and in-depth study on alternative CIGS solar cell back contact materials for both flexible and glass substrates. Initial candidate back contact materials included, but was not limited, to niobium (Nb), titanium (Ti), a nickel (Ni), and chromium (Cr). Additionally, layered structures consisting of copper, for example, to achieve low sheet resistance and a barrier layer to prevent reaction of copper with selenium were also investigated. GSE's unique monolithic integration approach allows consideration of bi-layers with copper as part of the back contact because the copper is never directly exposed to Se even after the back contact through-scribe operation.

Bulk properties of the several candidate back contact materials are listed in Table 10.2. In addition to the materials listed in Table 10.2, bi-layers and binary compounds such as nickel aluminides, titanium aluminides, nickel titanium, as well as conductive carbides and nitrides were investigated

Table 10.2. Key material properties and cost estimates for alternative back contact materials proposed for an in-depth investigation under the GSE PVMaT program.

Material	Electrical Resistivity, μΩ·cm	Melting Point, °C	Density gm/cm^3	Weight ft^2 of module grams	Cost of Target, $/kg	Cost per ft^2 of module, $†
Mo	5.2	2610	10.2	0.95	240	1.14
Nb	12.5	2468	8.57	0.80	149	0.60
Ni	6.8	1455	8.90	0.83	150	0.62
Ti	42	1660	4.5	0.42	52	0.11
Cr	12.9	1857	7.2	0.67	150	0.50
	~2.0	1083	8.92	0.83	50	0.21

† Accounts for Sputter Yield of 20%.

10.1.4.2 Alternate Back Contact for Polyimide

During Phase I, good results were achieved with a bi-layer back contact consisting of a compliant moderate CTE austenitic base metal with an overlayer of Mo. Based on small area devices this bi-layer was baselined and integrated into production. To further optimize the layer several small area devices were fabricated and tested. Unfortunately, fabricating small area device on polyimide was difficult and results were convoluted by inadequate isolation between adjacent devices. Laser scribing had been used for this purpose, but the process was under development and had the potential to further confound the interpretation of JV measurements. Isolating devices on polyimide by mechanical scribing was not practical as the polyimide deforms under pressure preventing effective isolation or inducing shunts. However, devices on stainless steel can be easily isolated mechanically.

To evaluate the bilayer contact, a special test web (S282) was prepared on stainless steel. The web was prepared by coating one half with a Cr/Mo and the other half with Cr/Mo/Ni:V/Mo. The Mo cap layer was deposited to prevent Se from reacting with the Ni:V layer. The entire web was coated with CIGS in a single step after which samples were removed for compositional analysis and SEM characterization. Subsequently, the web was processed whole through the final GSE coating steps and coupons were extracted from along the web and processed into devices.

The transition between the two different back contacts was easily discerned from the atomic concentration of Ni measured by EDS (Figure 10.1). The atomic ratio Cu/Ga+In, critical to device performance, remained relatively constant across the transition. The conversion efficiency of the test devices was found to drop dramatically crossing from the Cr/Mo to the Cr/Mo/Ni:V/Mo coated region. The degradation was observed to primarily affect V_{oc} and fill factor. The implication is that the Ni:V coating was responsible for the degraded device performance. As a result of these studies, the bilayer has been temporally replaced with multi-layer Mo awaiting the results of further experiments and investigation of additional alternative back contacts.

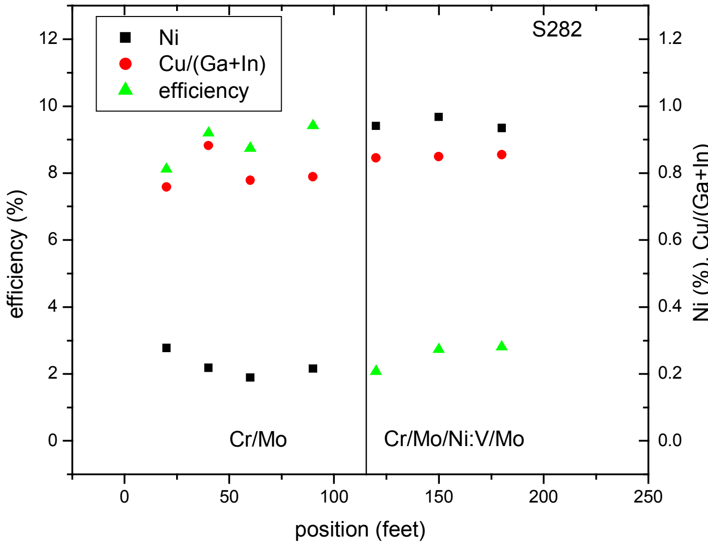

Figure 10.1. Evaluation of the Ni:V back contact on a stainless steel web.

10.1.4.3 Alternate Back Contact for Stainless Steel

The Mo sputtering conditions on stainless steel substrates were investigated for their effect on device efficiency. The pressure at which Mo is sputtered is known to have a strong effect on conductivity, morphology, and stress. The qualities of the Mo substrate should be expected to have a less than subtle effect on the crystallographic (and electronic) properties of the CIGS coating.

To determine the sensitivity of device efficiency to the Mo sputtering pressure, a stainless steel 105-foot test web was prepared by depositing Mo at 2, 4, 6, 9, 12, and 15 mTorr in 15-ft increments. All other parameters were maintained at a constant setting. The web was coated with CIGS and window layers in single passes under standard conditions. Coupons were removed from each section and small-area devices were fabricated and then characterized by illuminated JV measurements.

The results for the V_{oc}-fill factor product as a function of Mo sputtering pressure are shown in Figure 10.2. Each condition represents the average and standard deviation of 36 devices. The efficiencies, which reached a maximum of over 9%, are not shown compared because of variation in cell area which induces additional noise in the short-circuit current density. The optimum sputtering pressure for Mo in the GSE process is between 6 and 9 mTorr.

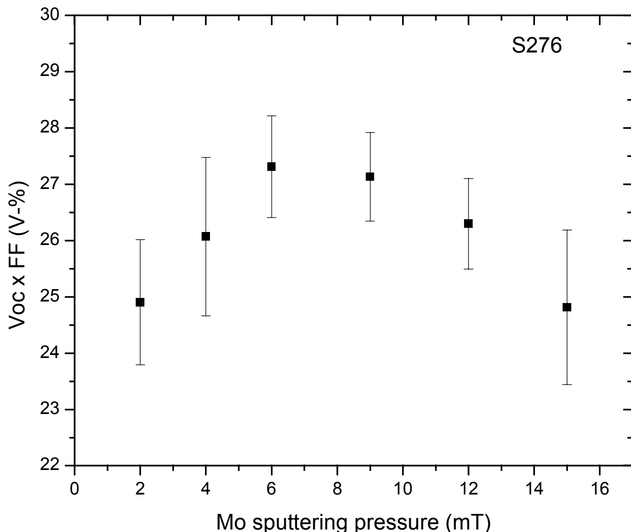

Figure 10.2. V_{oc}-fill factor product as a function of Mo sputtering pressure for lot S276.

10.2 Front Contact Introduction

Key requirements of the front contact are a low optical absorption over the entire wavelength spectrum in which CIGS is active (~400 to 1100 nm) and low sheet resistance. Achieving a balance of these properties while maintaining high rate deposition presents a significant technical challenge.

Issues associated with transparent conductive oxide (TCO) top contact deposition include:

- achieving high rates (>200 Å /sec) to support high throughputs,
- variation in sheet resistance resulting from minor differences in the underlying CIGS properties,
- dramatic change in the TCO properties as a function of sputtering target erosion, (sheet resistance has been measured to change by up to 10× during full target consumption if sputtering parameters are not actively adjusted),

- damaging the previous Mo/CIGS/CdS layers by arcing or ion bombardment that occurs during high rate TCO deposition, and

- cost of precursor conductive oxide materials.

10.2.1 Front Contact Task Objectives

Goals for the front contact portion of this task include:

- increasing throughput speeds of high quality TCO by 100% to a final web rate of 12-in/min.

- improving optical transmission and sheet resistance uniformity during long runs,

- increasing yield by significantly reducing arc and ion bombardment damage, and

- improve TCO uniformity.

10.2.2 Front Contact Technical Approach

Key items that will be investigated are alternative deposition approaches including DC magnetron, RF magnetron, low or mid frequency sputtering and mixed mode sputtering as well as modified cathode assemblies. In addition, GSE will design and implement optical emission techniques to monitor the deposition process and provide active real time control of critical sputtering parameters to maintain properties within tight control boundaries. Optimization of optical and electrical properties of the TCO are generally carried out through statistically designed experiments. Preference will be given to the techniques having the high deposition rates, low substrate damage/heating and simplicity.

10.2.3 Front Contact Results

10.2.3.1 Optical Emission Spectroscopy (OES) Control

In-situ OES equipment has been set up to monitor optical emission lines representative of one or more of the metallic exited transitions in the sputtering plasma. We have also found it useful to monitor emission lines characteristic of background components, such as hydrogen and nitrogen. Thus, the OES can be used to monitor contamination levels as well as to continuously monitor plasma emission that is related to the deposition rate. On our equipment the metallic OES signal of the target was incorporated in a feedback control loop to the sputtering power supply to continuously change the sputtering current to compensate for target erosion.

Statistical analysis of sputtering rate versus target life revealed variation remaining in the sputtering rate that was not compensated for by the OES signal. Recent tests indicate that the rate at which the OES signal changes with target erosion may depend on the mounting position and orientation of the OES sensor. We will try to find a mounting location for the OES that exactly compensates for target life, or alternatively, we will use a programmed rate of change

under software control to keep sputtering rate constant. The latter option would not depend on the OES signal.

10.2.3.2 Elimination of Arc Damage

Arc damage occurred in the sputtered TCO process on partially finished modules on polyimide substrate. Most frequently the arc damage was at the edge of the web, or on the interior where scribe lines intersected. The arc damage appeared to be caused by surface charge build-up on the web by the sputtering discharge, and subsequent discharge at some point of contact between the web edge and a grounded transport part, such as a roller. Since modifications were made to the system to prevent the flow of sputtering current through the web and transport parts, the symptoms of the arc damage have disappeared.

10.2.3.3 Process Optimization and Throughput

Several statistically designed experiments were run to map the responses of sheet resistivity, optical transparency and film stress to independent variables of sputtering power, oxygen flow and total pressure. Dependence of the response variables were fit as linear functions over the range of interest, allowing us to choose parameters that would yield the best optical transparency for a required sheet resistivity.

Subsequently, more targets were added to increase the web speed and thus the process throughput. Re-optimization of the parameters was required, again through a designed experiment. Presently the web speed has been increased to 6-in./min and our standard process yields TCO having 12 Ω/ with an integrated absorptive loss to a CIGS cell of less than 6 mA/cm^2 on glass as standard. The optical transmission of a sample of TCO on a glass witness that had a sheet resistivity of 12.3 Ω/ and an integrated absorptive loss of 4.9 mA/cm^2 is shown in Figure 10.3.

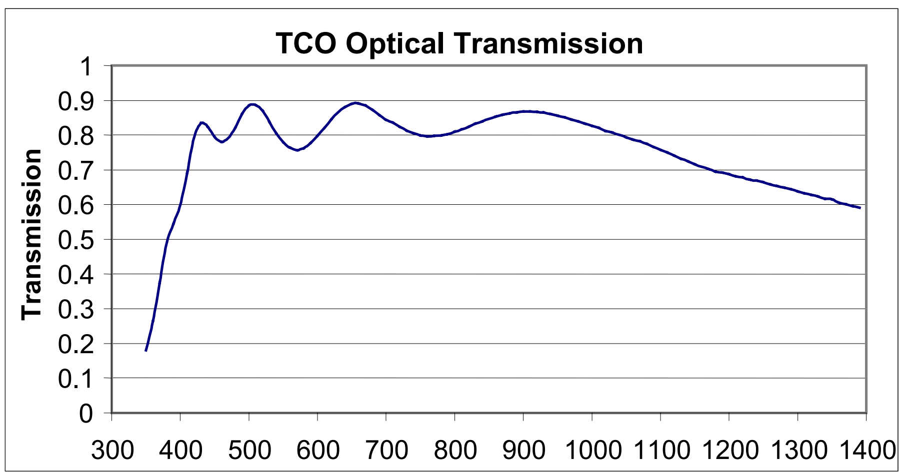

Figure 10.3. The optical transmission of TCO on glass having 12.3 Ω/□ sheet resistivity and about 4.9 mA/cm2 integrated absorptive loss on a CIGS device.

Run to run variation, shown in Figure 10.4, is usually well controlled with occasional exceptions. Causes for the exceptions are usually arc events caused by debris near the cathodes.

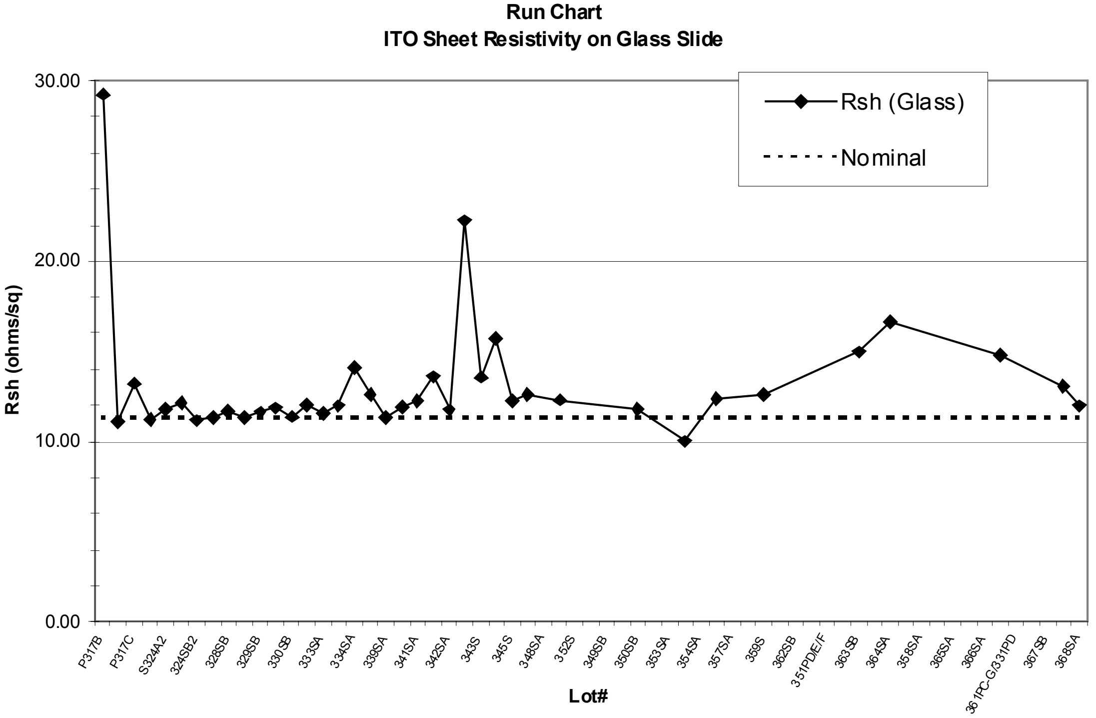

Figure 10.4. Typical run chart data for the TCO process showing lot-lot variation in sheet resistivity, taken on glass witness coupons co-deposited with the CIGS web.

10.3 Summary

Although The Ni-V/Mo alternative back contact demonstrated good performance during Phase 1, continued experiments in large area production equipment revealed potential diffusion of the Ni constituent into the CIGS. Resultant devices exhibited much poorer performance as compared to devices prepared with standard Mo. Work will continue with alternate bi-layer configurations.

Top contact repeatability and properties were substantially improved. Hundreds of runs have been conducted, many with full target consumption (which normally changes rate) with the resultant film exhibiting transmission and sheet resistance values that fall with established specification limits.

REPORT DOCUMENTATION PAGE

Form Approved
OMB NO. 0704-0188

Public reporting burden for this collection of information is estimated to average 1 hour per response, including the time for reviewing instructions, searching existing data sources, gathering and maintaining the data needed, and completing and reviewing the collection of information. Send comments regarding this burden estimate or any other aspect of this collection of information, including suggestions for reducing this burden, to Washington Headquarters Services, Directorate for Information Operations and Reports, 1215 Jefferson Davis Highway, Suite 1204, Arlington, VA 22202-4302, and to the Office of Management and Budget, Paperwork Reduction Project (0704-0188), Washington, DC 20503.

1. AGENCY USE ONLY (Leave blank)	2. REPORT DATE	3. REPORT TYPE AND DATES COVERED
	March 2001	Phase II Annual Subcontract Technical Report, July 1999–August 2000

4. TITLE AND SUBTITLE
Photovoltaic Manufacturing Cost and Throughput Improvements for Thin-Film CIGS-Based Modules; Phase II Annual Subcontract Technical Report, July 1999–August 2000

5. FUNDING NUMBERS
C: ZAX-8-17647-11
TA: PVP16101

6. AUTHOR(S)
R.G. Wendt and S. Wiedeman

7. PERFORMING ORGANIZATION NAME(S) AND ADDRESS(ES)
Global Solar Energy, L.L.C.
5575 S. Houghton, Rd.
Tucson, AZ 85747

8. PERFORMING ORGANIZATION REPORT NUMBER

9. SPONSORING/MONITORING AGENCY NAME(S) AND ADDRESS(ES)
National Renewable Energy Laboratory
1617 Cole Blvd.
Golden, CO 80401-3393

10. SPONSORING/MONITORING AGENCY REPORT NUMBER
NREL-SR-520-29283

11. SUPPLEMENTARY NOTES
NREL Technical Monitor: R. L. Mitchell

12a. DISTRIBUTION/AVAILABILITY STATEMENT
National Technical Information Service
U.S. Department of Commerce
5285 Port Royal Road
Springfield, VA 22161

12b. DISTRIBUTION CODE

13. ABSTRACT *(Maximum 200 words)* Thin-film photovoltaics (PV) has expanded dramatically in the last five years, but commercial use remains limited by performance, cost, and reliability. Of all the thin-film systems, copper indium gallium diselenide (CIGS) has demonstrated the greatest potential for achieving high performance at a low cost. The highest-quality CIGS has been formed by multi-source co-evaporation, a technique pioneered in this country by researchers at NREL. Multi-source co-evaporation is also potentially the fastest and most cost-effective method of CIGS absorber deposition. Global Solar Energy (GSE) has adapted multi-source co-evaporation of CIGS to large-area, roll-to-roll processing on flexible substrates, enabling several manufacturing and product capability advantages. Roll-to-roll processing enables a low-cost, automated continuous manufacturing process. Flexible substrates enable product application in unique, as well as traditional, areas. The primary objectives of the GSE Photovoltaic Manufacturing Technology (PVMaT) subcontract are to reduce cost and expand the production rate of thin-film CIGS-based PV modules on flexible substrates. Improvements will be implemented in monolithic integration, CIGS deposition, contact deposition, and *in-situ* CIGS control and monitoring. Specific goals of the three-year contract are:

- Monolithic Integration—Increase integration speed by developing high-speed, all-laser scribing processes that are more than 100% faster than the baseline process and offer clean, selective scribing; increase capacity and substantially reduce module area losses by insulating materials with high accuracy into laser scribes.
- Absorber Deposition—Increase absorber-layer deposition rate by 75% in the large-area, continuous GSE process, increasing throughput and reducing labor and capital costs. Integrate a parallel detector spectroscopic ellipsometer (PDSE) with mathematical algorithms for *in-situ* control of the CIGS absorber, enabling runs of over 300 meters of moving substrate, while ensuring uniform properties; enhance health and safety by reducing selenium waste generation through modifications to the reactor and Se delivery method.
- Back Contact Deposition—Reduce back-contact cost and increase operation yield by using improved back-contact materials.

14. SUBJECT TERMS
photovoltaics; copper indium gallium diselende; CIGS; multi-source co-evaporation; roll-to-roll processing; flexible substrates; monolith integraton; absorber deposition; back contact deposition; laser selective scribes; in-situ control; parallel detector spectroscopic ellipsometer

15. NUMBER OF PAGES

16. PRICE CODE

17. SECURITY CLASSIFICATION OF REPORT	18. SECURITY CLASSIFICATION OF THIS PAGE	19. SECURITY CLASSIFICATION OF ABSTRACT	20. LIMITATION OF ABSTRACT
Unclassified	Unclassified	Unclassified	UL